University of Milano-Bicocca

DEPARTMENT OF MATERIALS SCIENCE
Doctorate in Materials Science and Nanotechnology — XXXII Cycle

Continuum modeling of heteroepitaxy at the mesoscale: tackling elastic and plastic relaxation

Candidate:
Fabrizio Rovaris

Thesis advisor:
Prof. Francesco Montalenti

Coordinator:
Prof. Marco Bernasconi

Academic year 2019/2020

CONTENTS

LIST OF FIGURES

INTRODUCTION

The development of cutting-edge micro and opto-electronic devices requires increasingly high standards on the material quality. Indeed, up to nowadays, the advancement of the microelectronic industry has relied on the aggressive downscaling of the size typically featured by devices in the silicon-based technology. However, since the miniaturization of the "standard" MOS transistor design cannot go beyond a certain size, the microelectronic industry has pursued different solutions, ranging from different transistor architectures [1, 2, 3] to the heterointegration of different semiconductors on Si substrate to be used as base material for MOSFET channels [4]. The appealing aspect of this heterointegration is the possibility to exploit the superior material qualities of a wide range of semiconductor materials while maintaining the manufacturability in the Si foundries [5], the standard of the microelectronics industry.

One of the major issues that has to be addressed while attempting an heterointegration is controlling the effect of the difference in lattice parameter between the epi-layer and the substrate. Indeed, the first deposited monolayers, grow pseudomorphically, resulting in an in-plane deformation of the film lattice parameter to match the substrate one, leaving the epilayer in a strained condition. The elastic energy accumulated due to this reticular misfit can be released in two possible ways, elastically through the deformation of the planar morphology into three dimensional structures (named islands) or plastically with the loss of its in-plane lattice coherence with that of the substrate, via nucleation of misfit dislocations (MDs) [6]. MDs are terminated by threading arms, which do not contribute to the relaxation but extend up to the free surface. These defects, known as threading dislocations (TDs) are the most detrimental for the applications, since they reach the active area of the final devices. Lowering the density of these defects represents one of the main obstacle in view of further exploitation of heteroepitaxial systems, since, with the technological node approaching the 6 nm limit for 2020 roadmaps (see e.g. Ref. [7]), even the presence of a single defects can severely reduce the desired performance of the devices, inhibiting any expected advantage from the superior material quality. Such requirement calls for a tight synergy between experimental and theoretical investigations, since the parameter space for a heteroepitaxial process is too large to be sampled by a trial and errors approach.

This Thesis is devoted to the modeling of the heteroepitaxial growth, with the main focus on Ge (or SiGe alloys) on Si substrates. Ge has shown to have superior optoelectronic properties and higher carrier mobility with respect to Si and indeed it has been exploited in many applications in the Si-based technology as high-performance transistors [8], solar cells [9, 10] or photodetectors [11]. Furthermore, the SiGe/Si system has been widely investigated in literature, being frequently proposed as a prototypical system to study

the hetereoepitaxial process, and thus most of the developed methodology can be applied to other lattice-mismatched systems.

In this work the various aspect of heteroepitaxy described above, ranging from the elastic relaxation with the formation of three-dimensional islands, to the plastic relaxation of thin films and heterostructures are investigated by means of theoretical models based on continuum approaches. Working at the continuum level conveniently allows to match typical experimental sizes of interest (up to several tens of μm) and time scales (up to several minutes). Obviously, however, such models only describe average behavior on sufficiently large scales (tens of Å). As we shall show, such limitations do not prevent the description of several key phenomena in semi-quantitative agreement with experiments.

Modeling heteroepitaxy requires the proper description of several different phenomena. Purely elastic relaxation requires to describe the free surface diffusion of material responding to local gradients in the strain field and has been implemented by means of a computational code able to solve the differential equation for surface diffusion by means of the Finite Element Method (FEM). This was done by implementing a two and three dimensional code based on the FEniCs [12, 13] framework for solving partial differential equations. The generality of the developed code has also permitted the description of the solid-state dewetting of strained films, a topic that was not initially considered, by the implementation of the wetting potential proposed in Ref. [14] to described the behavior of thin layer exhibiting a finite contact angle with their substrate.

Modeling the plastic relaxation in heteroepitaxial systems, instead, requires the use of a code able to describe the behavior of single defects, still keeping the description of the spatial scale of interest described above. This was done by means of a discrete Dislocation Dynamics (DD) code, microMegas, exploiting a 6-month visit to the group of Prof. Devincre and Dr. Gatti at the Laboratoire d'etudes des Microstrucures (LEM) at the CNRS-Onera laboratory in Chatillon, where the code was the developed. During this period of collaboration an extension of the DD code able to tackle the presence of free-surfaces, called the Discrete Continous Model (DCM) [15], was implemented in the same FEniCs environment presented before.

Once the required methodology was implemented, a very extensive comparison with experimental results was carried out. The goal was not limited to providing interpretation of available data, but also to suggest to various experimental partners better growth condition to achieve the desired results. Particularly useful in model development and application were the close collaboration with research group at SILTRONIC (one of the world-leading company for the growth of hetereopitaxial substrates), and with more academic research group. These will be cited when presenting their experimental results during this manuscript.

This Thesis is organized as follows. Chapters 1 and 2 are devoted to provide the main physical background for the systems under consideration, dealing respectively with heteroepitaxial growth and dislocations. They provide a brief introduction to the topics and insights on the modeling tools used in the remaining of the Thesis. Chapter 3 deals with the implementa-

tion of the above described physical models into the numerical codes developed in this Thesis.

Chapters 4, 5 and 6 report the results obtained during this Thesis work. Specifically, in Chapter 4 entitled "From plastic to elastic relaxation" are presented the results obtained for the modeling of the competition between elastic and plastic relaxation. The results presented range from systems exhibiting a purely elastic behaviors, as in the modeling of the the solid-state dewetting of thin strained films, to phenomena that clearly shows the competing effects of these two possible relaxation paths, with a clear transition from a predominantely-elastic regime (formation of heteroepitaxial islands and cyclic growth) to a plastic regime (growth of nearly flat, plastically-relaxed thin films).

In Chapter 5 entitled "Misfit dislocation distribution in heteroepitaxy" specifically moves in details towards the plastic relaxation of heteroepitaxial thin films, providing a detailed analysis of the network of misfit dislocations formed during the growth of a low-misfit SiGe/Si film and showing its relation with the formation of Cross-hatch patterns, a well-known phenomena consisting in the formation of regular surface undulations.

Finally, Chapter 6 "Threading dislocation in heteroepitaxy" deals with the unavoidable formation of threading defects involved in the plastic-relaxation process. First, thanks to an extension of the DD code described above a simulation reproducing the progressive plastic relaxation during the deposition of a thin film is reported. Then, an unexpected phenomena leading to a quasi-unidirectional relaxation in macroscopic regions of a SiGe/Si wafer will be analyzed in detail and explained by means of DD simulations. Finally, the end of the Chapter will presents some combined experimental and theoretical characterization of the dislocation distributions in Vertical Heterostructures (VHEs) recently proposed as a viable path to reduce the number of threading defects [16].

Finally, analytical expression for the displacement, strain and rotational fields produced by array of dislocations, including the derivations of the strain fields for the case of dislocations near a free surface and for non-singular strain expressions, are reported in Appendix A.

1 MODELING GE/SI HETEROEPITAXY

In this first chapter, we shall provide an introduction to the physical system under consideration in this Thesis together with the basis for the modeling tools that will be implemented in the remainder of the manuscript.

Section 1.1 presents a brief overview of heteroepitaxial and a discussion of aspects specific to Ge/Si heteroepitaxy. Then, in section 1.2 we shall provide an introduction to the Linear Elasticity Theory as the framework for all the models developed in this Thesis. Direct applications of the linear elasticity theory to the topic of thin strained films are briefly treated here.

Section 1.3 introduces the equation for surface diffusion and its application tp the modeling of elastic relaxation in heteroepitaxial growth. In section 1.4 the model is further developed with the introduction of a wetting potential specifically designed to model Ge/Si heteroepitaxy.

Finally, section 1.5 provides a first insight on the mechanism of plastic relaxation in heteroepitaxy via misfit dislocations. The treatment of the elastic theory of dislocations will be further expanded in the whole chapter 2.

1.1 HETEROEPITAXIAL GROWTH

Heteroepitaxial growth refers to the process of growing a crystalline film over a substrate with a different lattice parameter. In this process the epilayer tends to cover coherently the substrate, resulting in a strained-state due to the reticular mismatch. From the energetic point of view the main contribution playing a role during an heteroepitaxial growth are the surface energies per unit area of the film and the substrate, γ_f and γ_s respectively, the substrate-epilayer interface energy per unit area, γ_i and the lattice elastic energy density ρ_{el} due to the lattice mismatch ε between them. This latter quantity can be defined as:

$$\varepsilon = \frac{a_s - a_f}{a_f} \tag{1}$$

where a_s and a_f are respectively the lattice constants of substrate and film in their unmodified sate. The possible growth modalities that can take place in an heteroepitaxial proccess are usually schematized in different regimes. The first possibility corresponds to a layer-by-layer growth where the film is coherent with the substrate and remains flat without altering its morphology. This is known as Frank-van der Merve (FM) growth. Another growth regime, known as Volmer-Weber (VW) consists in 3D island formation on the substrate. The last modality, known as Stranski-Krastanov (SK) is intermediate between those two, with the formation of islands after the completion of a thin wetting layer. These growth modalities are schematically illustrated in Fig. 1.

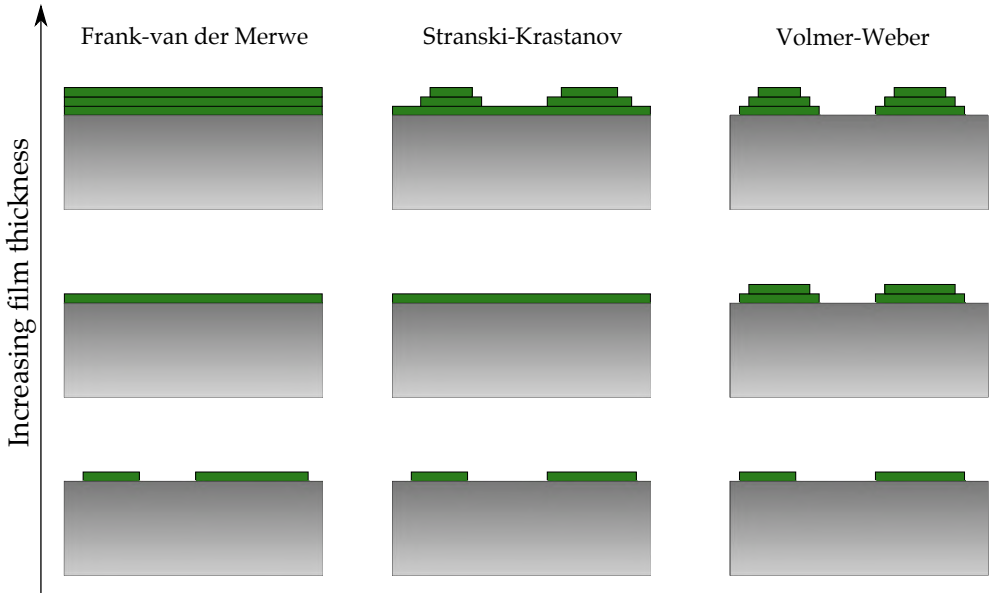

Figure 1: Heteroepitaxial growth regimes. The Frank-van der Merwe growth corresponds to a low misfit between film and substrate, and can sustain a flat growth without altering the morphology of the film. The Stranski-Krastanov is an intermediate case where the growing of islands can begin after the deposition of a few monolayers of wetting layer. The Volmer-Weber regime corresponds to and high misfit condition in which the 3D islands growth begins immediately with the deposition.

This general schematization can be rationalized by considering the energetic contributions acting during an heteroepitaxial growth. Considering the surface energy densities it is easy to understand that, if $\gamma_s > \gamma_f + \gamma_{sf}$ the complete wetting of the substrate is favored and a layer-by-layer growth occurs. On the opposite side, if $\gamma_s < \gamma_f + \gamma_{sf}$, covering the substrate with the film has a net energy cost and so the film tends to immediately retract forming 3D islands and exposing the substrate. Adding the effect of the elastic energy to this description can also explain the SK growth. Indeed, the elastic term tends to deform the flat geometry of the film by forming islands. The energy gain corresponding to island formation depends on the island volume, thus when the total energy balance $\Delta E_{tot} = \Delta E_{elastic} + \Delta E_{surface}$ becomes negative, islanding is favored as in the Stranski-Krastanow (SK) growth. The presence of the wetting layer in the SK growth has a physical meaning since it allows for an high energy gain during the deposition of the first mono-layers, which covers the dangling bonds of the exposed substrate surface. After this stage the energy balance returns favorable to islands formation.

1.1.1 Ge/Si heteroepitaxy

In this Thesis we consider the deposition of SiGe layers on silicon substrates. This is a typical example of heteroepitaxial system well studied in literature [17, 6] both for the importance of SiGe devices themselves [8, 9, 10, 11], both as representative case study for the SK growth. Indeed, other common heteroepitaxial systems such as InGaAs layers grown on GaAs [18], GaAsP on GaAs substrate [19] or InP on silicon [20] exhibit SK growth. While the spe-

cific details of the growth process should be considered for each case, some general aspects can be still be drawn from the modeling tools developed for Ge/Si systems.

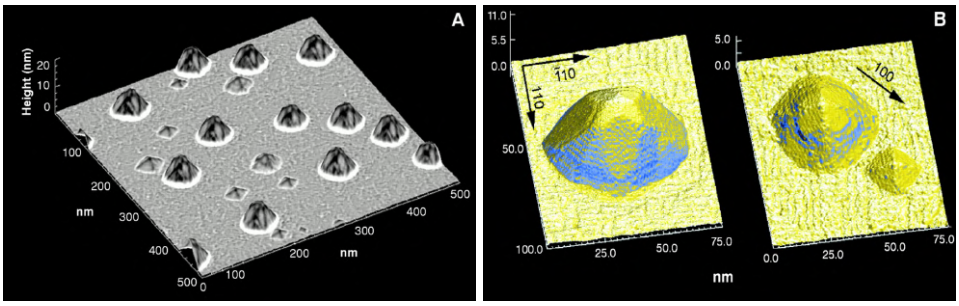

Figure 2: STM image of germanium islands grown on Si(001). On the right is possible to observe two different island shapes, larger dome and smaller pyramids. Image adapted from Ref. [21].

Ge and Si have the same diamond-like crystal structure and thus can be grown heteroepitaxially producing a high-quality single crystalline film. However, they have different lattice parameters, as reported in the following table for pure Si and Ge:

Si	Ge
5.43 Å	5.65 Å

Given these values the resulting misfit strain can be calculated starting from Eq. 1:

$$\varepsilon_0 = \frac{a_{Si} - a_{Ge}}{a_{Ge}} = -3.99\%$$

The effect of this lattice mismatch is a compression of the Ge film grown on Si, because during the deposition the germanium adatoms are forced to the lattice sites on top of the exposed silicon surface. So the deposited germanium, distorted to match the value of silicon lattice constant is forced to expand in the free surface direction, producing a tetragonal distortion. This strained condition can be sustained only for the first few monolayers, thanks to the high energy gain when germanium covers the dangling bonds on the silicon surface. After this stage the film tends to relax elastically forming in 3D islands. The critical thickness condition for the onsets of island formation depends on the germanium concentration in the film, but is typically just a few mono-layers [22]. Furthermore in a SiGe/Si(001) film the islands morphology generally depends on the volume and, as reported in Fig. 2, different shapes can be observed, with smaller islands forming pyramids while larger domes exposing a higher number of crystallographic facets [21, 22]

Germanium and Silicon can be mixed producing SiGe alloys at various Ge concetration x. The resulting alloy is considered to be a perfect mixture of silicon and germanium with a resulting lattice parameter that can be expressed with good approximation by means of the Vegard's law:

$$a_{Si_{1-x}Ge_x} = (1-x)a_{Si} + x \cdot a_{Ge} \tag{2}$$

Varying the concentration of germanium thus modifies the total reticular misfit between the SiGe layer and the substrate, leading to completely different behaviors for the relaxation of the deposited film.

1.1.2 Growth techniques

The heteroepitaxial growth process consists in the deposition of a chemical species on a substrate in controlled condition of temperature and deposition flux. Physical vapor deposition (PVD) and Chemical Vapor Deposition (CVD) are the most common methods for transferring material atom by atom from a source to a substrate. Vapor deposition describes any process in which a solid immersed in a vapor can grow due to reactions from vapor phase to the solid phase. The deposition normally occurs in a vacuum chamber to finely tune the partial pressures of the vapors of the chemical species being deposited. In the PVD the vapor is created by physical means, while in the CVD the deposited material is the product of a chemical reaction.

Chemical vapor deposition provides a method for growing semiconductors or a wide class of thin film materials in which a chemical reaction between a gaseous precursor and a volatile compound of the material from which the film have to be grown occurs. This produces an atmosphere with a gaseous compound of the material to be deposited (as SiH_4 or GeH_4 for the case of Si and Ge). This vapor phase can condensate to the solid surface exposed, fine-tuned by the temperature of the substrate or by means of a plasma phase. The control of the parameters of the growing film can be made by tuning the vapor supersaturation and the substrate temperature. Low vapor supersaturation and high substrate temperature can favor the growth of a coherent single crystalline film on the substrate, while high supersaturation and low temperature tend to grow amorphous films.

On the other side, among the possible PVD methods the most used for the growth of semiconductors is the Molecular Beam Epitaxy (MBE) that can provide crystalline film materials of very high quality, but generally with a slow growth rate compared to other CVD reactors. This technique achieves a near equilibrium growth, opposed to the CVD method presented above, widely in industrial applications due to their high deposition flux. In a MBE reactor a substrate wafer is placed in an ultra-high vacuum chamber, ($p \simeq 10^{-8}$ Pa). The substrate typically heated at a temperature of $T \simeq 500$ - 1000 K. The growth occurs by directing collimated atomic beams of the film materials, obtained from a Knudsen evaporation cell that is heated well above the substrate temperature, to induce evaporation and condensation. The peculiarity of this growth technique is the precise control on the deposition: it is possible to reach very low rates, up to fractions of monolayer (ML) 10^{-1} - 10^{-2} ML s^{-1}. It also permits the deposition of different species on the same substrate, by using multiple evaporation cells. The relative composition can be finely tuned controlling the deposition flux and time for each cell. Another feature associated to this deposition method is the possibility to monitor *in situ* the complete history of the film during growth [23, 24, 25].

As mentioned above, the condition for a vapor deposition is that the substrate temperature T_s must be low enough for the vapor phase to be over-

satured, so that atoms in the gas can attach to the substrate and become *adatoms*. The conditions for growing crystalline films are that the deposition flux must be low enough and the substrate temperature high enough to permit the adatoms to explore different atomic sites at the surface. This cause a net flux of material at the surface toward the local energy minimum. This can be regarded as a local process because the adatoms have only a limited diffusion length, dependent on the temperature. Furthermore, the deposition of a new layer of atoms freezes the preceding adatoms at the atomic sites reached, because they become bulk atoms with a higher number of chemical bonds.

1.2 LINEAR ELASTICITY THEORY

In this Thesis the topic of heteroepitaxial growth is treated by continuum models with the linear elasticity theory as a framework. This description allows to tackle the evolution of large system (up to tens of microns) at long time scales (up to several minutes), not accessible with atomistic models. In this section an overview of linear elasticity theory drawn from references [26, 27, 28] is presented.

Let $\mathbf{x} = x_i \mathbf{e}_i$, $(i = 1, 2, 3)$ be the vector that describe the position of a point inside an undeformed medium. We can denote the forces per unit area acting on this body as σ_{ij}, where σ_{ij} is the i-th component of the force acting on a plane whose outward normal is parallel to the positive x_j direction. At rest each infinitesimal volume of the solid must be in mechanical equilibrium, and we assume that no net torque can act on the body so the stress matrix must be symmetric:

$$\sigma_{ij} = \sigma_{ji} \tag{3}$$

If the medium undergoes a deformations the positions in the new state are given by $\mathbf{x'} = x'_i \mathbf{e}_i$. We can define the displacement vector as:

$$\mathbf{u}(\mathbf{x}) = \mathbf{x'} - \mathbf{x}$$

$\mathbf{u}$, is a vector field, and in the elastic theory the displacements and their derivatives are assumed to be small, so $|\mathbf{u}| \leqslant 1$ and $|\nabla \mathbf{u}| \leqslant 1$. Given these definitions we can define a *strain tensor* and a *rotation tensor* by a Taylor expansion of $\mathbf{u}(\mathbf{x})$:

$$\begin{aligned} u_i(\mathbf{x}) &= u_i^0 + \frac{\partial u_i}{\partial x_j} \, dx_j \\ &= u_i^0 + \frac{1}{2}\left(\frac{\partial u_i}{\partial x_j} + \frac{\partial u_j}{\partial x_i}\right) dx_j + \frac{1}{2}\left(\frac{\partial u_i}{\partial x_j} - \frac{\partial u_j}{\partial x_i}\right) dx_j \\ &= u_i^0 + \varepsilon_{ij} \, dx_j + \Omega_{ij} \, dx_j \end{aligned}$$

where we have indicated with ε the symmetrical part of this expansion, known as *strain tensor*:

$$\varepsilon_{ij} = \frac{1}{2}\left(\frac{\partial u_i}{\partial x_j} + \frac{\partial u_j}{\partial x_i}\right) \tag{4}$$

and with Ω the anti-symmetrical part, the *rotational tensor*:

$$\Omega_{ij} = \frac{1}{2}\left(\frac{\partial u_i}{\partial x_j} - \frac{\partial u_j}{\partial x_i}\right) \tag{5}$$

When a stress field is applied on the physical system, it responds to it by means of a deformation associated to a strain field, described by means of a linear relation through the elastic constants of the material. In general this relation can be written as:

$$\sigma_{ij} = C_{ijkl}\varepsilon_{kl} \tag{6}$$

that is known as the *Hooke's law*. The tensor $\mathbf{C}$ collects all the elastic constants of the system. From equation (3) and from the immediate condition $\varepsilon_{ij} = \varepsilon_{ji}$, it follows directly that:

$$C_{ijkl} = C_{jikl} = C_{ijlk} = C_{jilk}$$

Furthermore, because of crystal symmetry, the number of independent constants is reduced further and in crystals with cubical symmetry the tensor $\mathbf{C}$ has only three independent constants, C_{11}, C_{12}, C_{44}. Equation (6) can be written under this assumption in the Voigt representation, in which only the independent components of tensor ε and σ appear:

$$\begin{bmatrix}\sigma_{xx}\\ \sigma_{yy}\\ \sigma_{zz}\\ \sigma_{xy}\\ \sigma_{xz}\\ \sigma_{yz}\end{bmatrix} = \begin{bmatrix}C_{11} & C_{12} & C_{12} & 0 & 0 & 0\\ C_{12} & C_{11} & C_{12} & 0 & 0 & 0\\ C_{12} & C_{12} & C_{11} & 0 & 0 & 0\\ 0 & 0 & 0 & C_{44} & 0 & 0\\ 0 & 0 & 0 & 0 & C_{44} & 0\\ 0 & 0 & 0 & 0 & 0 & C_{44}\end{bmatrix} \cdot \begin{bmatrix}\varepsilon_{xx}\\ \varepsilon_{yy}\\ \varepsilon_{zz}\\ \varepsilon_{xy}\\ \varepsilon_{xz}\\ \varepsilon_{yz}\end{bmatrix}$$

If the system is also isotropic in three dimensions, we can also introduce the last condition that $C_{11} = C_{12} + 2C_{44}$. It is thus necessary to provide only two independent constants to describe the elastic behavior of this class of solids, $\lambda_L = C_{12}$ and $\mu_L = C_{44}$. The two constants λ_L and μ_L are called the *Lamé constants*.

1.2.1 Elastic energy

In the isotropic case the energy is given by the work done by the forces that act deforming the body. So, if the strain increment caused by a stress σ_{ij} is $d\varepsilon_{ij}$ the infinitesimal work done in the system is:

$$d\rho_\varepsilon = \sigma_{ij}\, d\varepsilon_{ij}$$

whose integration gives the energy density for a strained film, ρ_ε, that under our assumptions can be written in term of explicit elastic constants:

$$\begin{aligned}\rho_\varepsilon =& \frac{1}{2}(\lambda_L + 2\mu_L)(\varepsilon_{11} + \varepsilon_{22} + \varepsilon_{33})^2 \\ &+ 2\mu_L(\varepsilon_{12}^2 + \varepsilon_{23}^2 + \varepsilon_{13}^2 - \varepsilon_{11}\varepsilon_{22} - \varepsilon_{11}\varepsilon_{33} - \varepsilon_{22}\varepsilon_{33})\end{aligned} \tag{7}$$

Or an equivalent expression with stress components is:

$$\begin{aligned}\rho_\varepsilon =& \frac{1}{2E}\left(\sigma_{xx}+\sigma_{yy}+\sigma_{zz}\right)^2 \\ &+\frac{1+\nu}{E}\left(\sigma_{yz}^2+\sigma_{xz}^2+\sigma_{xy}^2-\sigma_{xx}\sigma_{yy}-\sigma_{xx}\sigma_{zz}-\sigma_{yy}\sigma_{zz}\right)\end{aligned} \tag{8}$$

where E and ν are the Young's modulus and the Poisson's constant of the material.

1.2.2 Eigenstrain

Misfit strain in heteroepitaxial films and/or plastic strain induced by dislocations should be added to this description. This strain fields cannot be describes as the linear response of the system to an applied loading by the Hooke's law of Eq. (6). To treat them within elasticity theory the concept of *eigenstrain* introduced by Mura [28] is required. The total strain in this approach is considered as the sum of an elastic ε and inelastic strain ε^*, called *eigenstrain*. The eigenstrain ε^* will then be defined as the strain required by the system assumes to restore its zero-force condition:

$$\boldsymbol{\sigma} = \mathbf{C}(\boldsymbol{\varepsilon}-\boldsymbol{\varepsilon}^*) = 0 \quad \Longrightarrow \quad \boldsymbol{\varepsilon} = \boldsymbol{\varepsilon}^*$$

Following this formalism, the strain ε correspond to the response of the system defined by this new strained reference state. The definition of the quantity as elastic energy of the system must include now also the eigenstrain as an additional term, so it becomes:

$$\rho_\varepsilon = (\varepsilon_{ij}-\varepsilon^*_{ij})C_{ij}(\varepsilon_{ij}-\varepsilon^*_{ij}) \tag{9}$$

1.2.3 Biaxially strained film

The system under consideration in this work is, as already discussed, a thin film of SiGe grown on a substrate of silicon. The deposited film is forced to cover the lattice sites at the top of the exposed silicon surface, resulting in an in-plane deformation of the SiGe lattice constant. In linear elasticity this condition can be modeled as a thin film subject to a biaxial compressive strain. The condition imposed on the free surface (with normal along the y direction $\hat{\mathbf{n}}$=$\hat{\mathbf{y}}$) is then:

$$\boldsymbol{\sigma}\cdot\mathbf{n} = \begin{pmatrix}\sigma_{xy}\\ \sigma_{yy}\\ \sigma_{zy}\end{pmatrix} = 0 \tag{10}$$

This condition at the free surface must hold in the whole homogeneous system for the continuity of stress field, so this correspond to the value of the stress tensor in the entire film. Furthermore, in a biaxial strained system the strain tensor reads:

$$\varepsilon_{xx} = \varepsilon_{zz} = \varepsilon \qquad \varepsilon_{ij} = 0 \qquad \text{for} \qquad i \neq j$$

The value of the response strain along the free surface direction can be obtained starting from the condition (10) and from the definition of σ in equation (6):

$$\begin{aligned}\sigma_{xx} &= C_{11}\varepsilon_{xx} + C_{12}\varepsilon_{yy} + C_{12}\varepsilon_{zz}\\ 0 &= C_{12}\varepsilon_{xx} + C_{11}\varepsilon_{yy} + C_{12}\varepsilon_{zz}\\ \sigma_{zz} &= C_{12}\varepsilon_{xx} + C_{12}\varepsilon_{yy} + C_{11}\varepsilon_{zz}\end{aligned}$$

solving this system of equation we obtain

$$\varepsilon_{yy} = -\frac{C_{12}}{C_{11}}(\varepsilon_{xx} + \varepsilon_{zz})$$

Finally, calculating from (7) the energy density of this biaxial strained system results in:

$$\rho_\varepsilon = Y\varepsilon^2 \tag{11}$$

where Y is the biaxial Young's modulus, defined with respect to the other constants as:

$$Y = \left(C_{11} + C_{12} - 2\frac{C_{12}^2}{C_{11}}\right) = \frac{E}{(1-\nu)}$$

1.3 DIFFUSION LIMITED GROWTH

As discussed in section 1.1.2 in usual growth conditions an heteroepitaxial system exhibit diffusion of material mostly at its free surface. Indeed, bulk diffusion is negligible at the typical growth temperatures due to high activation barriers [29].

In this section we shall introduce the equation of surface diffusion and discuss how this can be used to model the elastic relaxation of heteroepitaxial films. Indeed, as presented first in Refs. [30, 31, 32] a strained film is unstable with respect to a perturbation that alters its surface morphology.

1.3.1 Thermodynamical concepts

In order to derive a continuum equation that on average describes the driving force for the diffusion of adatoms on a surface we need to consider the thermodynamical process that drives the system toward its equilibrium state. In our condition this evolution is considered as a near-to-equilibrium process, as expected in growth at high-temperatures and/or slow deposition fluxes. The appropriated thermodynamical potential used to describe a system at constant temperature and pressure is the Gibbs potential, defined by a Legendre transformation of the Helmoltz free energy F:

$$G = F - \frac{\partial F}{\partial V}\,dV = E - TS + pV \tag{12}$$

where p is the pressure, V the volume, S the entropy and E the energy. With this definition we can write the differential form of G, and use of the first law of thermodynamics, $dE = T\,dS - p\,dV + \sum_i \mu_i\,dn_i$:

$$dG = V\,dp - S\,dT + \sum_i \mu_i\,dn_i$$

Starting from this last expression we can obtain the definition of the chemical potential μ_i from the comparison of the differential form of G, and for the i-th chemical species n_i:

$$\mu_i = \left(\frac{\partial G}{\partial n_i}\right)_{T,P,n_j}$$

In the case of an heteroepitaxial growth such as an MBE or CVD at very low pressure, the pressure-volume contribution can be neglected so the Gibbs free energy and the Helmholtz free energy coincide. Furthermore, in our system we consider the diffusion of only one chemical species so also the sum over the index i can be dropped. With these definitions we have thus obtained that, at constant temperature T, the only thermodynamical potential required to describe the evolution of our system toward its equilibrium is the chemical potential μ.

As discussed in chapter 1 in our model diffusion can occur only for adatoms at the surface, so the definition of the chemical potential is required only for these atoms and consists of two contributions, one from the elastic energy of the strained body, and the other one from the surface energy

$$\mu = \mu_\varepsilon + \mu_\gamma$$

The first term in this sum is the contribution to the chemical potential due to the elastic energy of the system. This can be easily derived from the elastic theory presented in section 1.2 and in particular from equation (7). So the elastic chemical potential is the variation in elastic energy ρ_ε with the addition (or removal) of an atom of volume V_a in the considered position. Since $G_\varepsilon = \int_V \rho_\varepsilon \, d\mathbf{x}$ we obtain:

$$\mu_\varepsilon = \frac{\delta G_\varepsilon}{\delta n} = V_a \rho_\varepsilon \tag{13}$$

The other term in the sum is the surface chemical potential contribution and must be defined with respect to the surface energy.

1.3.2 Surface energy

The surface contribution to chemical potential corresponds to the energy cost that must be accounted for the creation of a free surface. This term tends to stabilize the surface perturbation as the growing of a fluctuation has a net energy cost for the system. This is due to the work that must be done to break the chemical bonds and create new surface atoms, and can be represented by a parameter γ that accounts for the surface free energy density. The total surface free energy in term of this value γ is:

$$G_\gamma = \int_S \gamma \, d\mathbf{S} \tag{14}$$

The evaluation of γ is a complex task since it can be function of various parameters. The surface energy is indeed modified when the considering the region close to the film-substrate interface. Furthermore, a crystal has different values of surface energies depending on facet orientations. In general

an estimation of the value of the surface energy density can be derived from ab-initio calculation as reported in Refs. [33, 34, 35]. For the scope of this work, γ is considered isotropic and with a thickness dependence added to account for wetting effects as we shall discuss in section 1.4.1.

From Eq. 14 we obtain the surface contribution to the chemical potential introduced above:

$$\mu_\gamma = \frac{\delta G_\gamma}{\delta n} = V_a \kappa \gamma \tag{15}$$

where κ is the curvature of the profile and accounts for the energy cost associated to variations in its length: $\kappa = \frac{\delta}{\delta n} \int_C dl$ and for a function written as $h = h(x)$, reads:

$$\kappa = -h''(1 + h'^2)^{-3/2}$$

1.3.3 Diffusion Equations

For finite diffusion coefficients, i.e. in the situation considered in this work as discussed in section 1.1.2, diffusion is a local process driven by gradients in chemical potential. By imposing material conservation, the following continuity equation holds:

$$\frac{\partial n}{\partial t} + \nabla \cdot \mathbf{J} = \Phi \tag{16}$$

where $\mathbf{J}$ is the material current and Φ is the external flux of atoms. The material current J can be defined in term of the chemical potential according to the Onsager's law [36, 37], that yields:

$$\mathbf{J} = -M \nabla_S \mu$$

with the coefficient M describing the mobility of the system and ∇_S is the surface gradient operator. So, expliciting this term in the continuity equation (16), we obtain:

$$\frac{\partial n}{\partial t} = -\nabla \cdot J + \Phi = \nabla \cdot (M \nabla \mu) + \Phi \tag{17}$$

1.3.4 Asaro-Tiller-Grinfeld instability

With this framework we can now follow the theory presented by Asaro, Tiller and Grinfeld [30, 38, 31] that accounts for a possible way of island formation in an heteroepitaxial system. This is caused by the competition between surface and elastic energies. The surface contribution accounts for an energy cost for the formation of new surfaces, so it tends to oppose to the corrugation of the flat geometry. The elastic term on the other side favors the formation of islands since they are elastically more relaxed with respect to the flat film.

The ATG theory consists in a linear stability analysis of the surface of a semi-infinite film under stress in a flat-island approximation, so the amplitude of the perturbation is assumed to be small. Let us consider a cosine perturbation on the surface of a film:

$$h(x) = a \cos(qx)$$

where a and q are the amplitude and wave number for the perturbation, and, in the flat-island approximation, they are taken to be $q \cdot a \ll 1$. Following Refs. [30, 32], the stress distributions at a distance d from the surface are:

$$\begin{cases} \sigma_{xx} = \sigma_0 - \sigma_0 \left(q^2 d - 2q\right) e^{-qd} a \cos(qx) \\ \sigma_{yy} = -\sigma_0 q^2 e^{-qd} a \cos(qx) \\ \sigma_{xy} = -\sigma_0 q(1 - qd) e^{-qd} a \sin(qx) \end{cases}$$

In addition, the film can be modeled as infinite in the third dimension by introducing an additional constant eigenstress in the z direction, so $\sigma_{zz} = \sigma_0$. The constant σ_0 is defined as $\sigma_0 = \frac{E}{(1-\nu^2)}\varepsilon_0$ the stress for the flat morphology. According to eq. (13):

$$\mu_\varepsilon = V_a \rho_\varepsilon(-qa\cos(qx)) \quad \text{with} \quad \rho_\varepsilon = 2\sigma_0\varepsilon_0$$

In our approximation $\kappa \approx -h''$ so that, for isotropic surface energy density γ, we have from eq. (15)

$$\mu_\gamma = -V_a \gamma h''(x) = V_a \gamma q^2 a \cos(qx)$$

Summing these two contributions, the chemical potential is obtained:

$$\mu = V_a(\rho_\varepsilon q - \gamma q^2) a \cos(qx)$$

The profile law evolution by surface diffusion then reads:

$$\frac{\partial h}{\partial t} = M\nabla^2\mu = MV_a\left(\rho_\varepsilon q^3 - \gamma q^4\right) a\cos(qx) \tag{18}$$

Searching a solution for Eq. (18) with the form: $h(x,t) = a(t)\cos(qx)$ we can define the evolution of the surface profile in term of only the amplitude factor a:

$$a(t) = ae^{-MV_a\gamma q^3(q-q_c)t} \quad \text{where} \quad q_c = \frac{2\pi}{\lambda_c} \sim \rho_\varepsilon/\gamma. \tag{19}$$

The sign of the amplification factor, i.e. the exponent of equation 3 in this expression depends on $q - q_c$. If $q > q_c$ the amplitude decays so that the flat surface is stable. If $q < q_c$, the film is unstable as the amplitude of the perturbation grows exponentially. This behavior as function of q is shown in Fig. 3, where each curve corresponds to a different value for the Ge composition x in a $Si_{1-x}Ge_x/Si$ system. Notice that a fastest perturbation exists at $q_{max} = 3/4q_c$. The typical length scale for the evolution of the perturbation is $\ell = q_c^{-1}$. The stability results also show a characteristic time scale $\tau = \ell^4/(MV_a\gamma)$, strongly dependent on the misfit ($\sim \varepsilon_m^{-8}$). Since M is expected to obey an Arrhenius law, $M \approx e^{-A/k_bT}$ with A an effective energy barrier and k_b the Boltzmann constant, τ is extremely sensitive to temperature and decreases exponentially when T is raised.

The previous arguments are developed for a single q mode. When considering a generic perturbation, decomposed in a Fourier series, in the limit of linear elasticity, each q component behaves independently from the others according to Eq. (19). The resulting profile will be dominated by the fastest q

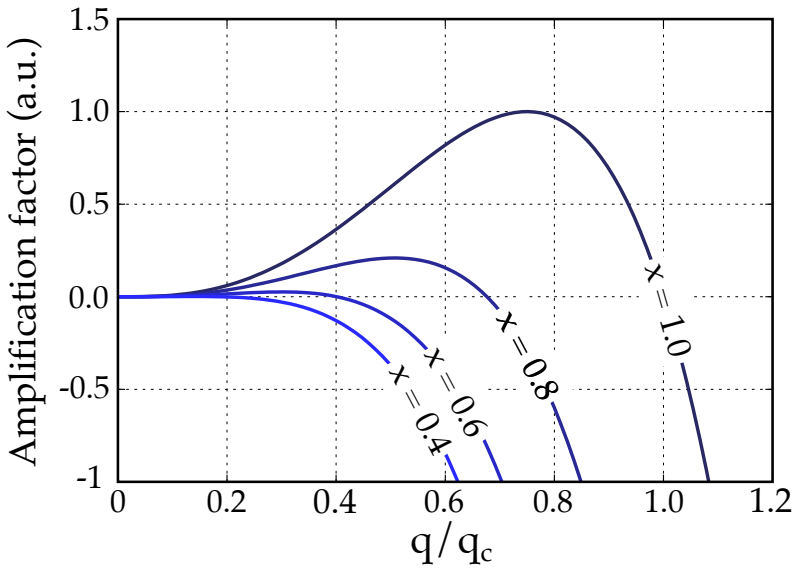

Figure 3: Amplification factor defined as the exponent of equation (19) as function of q for different germanium composition x in a $Si_{1-x}Ge_x$ film.

and for a white noise (ideally comprising all q values) the rise of the fastest perturbation with $q = q_{max}$ is expected. With this respect, the ATG model states that a stressed film is always unstable with respect to long-enough perturbation wavelengths $\lambda > \lambda_c = 2\pi/q_c$. However, when considering low misfits ε_m and/or high surface energy costs γ, too long λ_c, corresponding to extremely slow evolution τ, are expected but may be physically unreasonable leaving the film in a metastable state.

1.4 WETTING EFFECTS IN HETEROEPITAXIAL FILMS

The ATG model provides an analysis of the growing of a perturbation of small amplitude and can be used to describe the first stages of growth. An enhanced description must account for the solution of the equation (17) without the flat-island approximation introduced above. In this case the full expression for the curvature must be used: $\kappa = -h''(1 + h'^2)^{-3/2}$. Furthermore, an numerically exact description of the elastic field at the surface can be done by means of the Finite Element Method (FEM) in the solution of the mechanical equilibrium [39, 40, 41, 42]. This will be presented in Chapter 3

In this extended approach the simulation of the growth of a perturbation agrees with the solution obtained from the linear stability analysis of the ATG model in the first stages of evolution, in which the flat island approximation $qa \ll 1$ holds with the amplification of the initial sinusoidal profile. After the first stages the tendency is grow tips in the film forming cusp-like structures, breaking up the film in sharp trenches. These tips dig in the film and tend to form singularities in the surface profile, thus requiring a regularization to provide a realistic description of heteroepitaxial growth. This problem is studied in literature [43, 44, 45, 46] and a possible way reported is the modification of the surface energy in proximity of the substrate to account for the presence of a wetting layer in the Stranski-Krastanov growth.

In fact, in a Ge/Si system it is known that Si has an higher surface energy density than Ge. This property causes the formation of the Ge wetting layer, which covers all the Si surface, lowering the surface energy of the system.

1.4.1 Wetting potential for SiGe/Si(001)

The formation of a wetting layer in the SK growth can be modeled in our approach by a modification of the expression for the surface energy density γ considered so far [46, 47]. Results obtained from ab-initio calculations [48] show indeed a variation of the value of γ for the first few mono-layers close to the interface between a film and its substrate. The calculations reported in Fig. 4 are performed for the same Ge/Si system under consideration in this Thesis and can be used to quantify this surface energy modification. In our treatment the additional dependence of γ on the distance h from

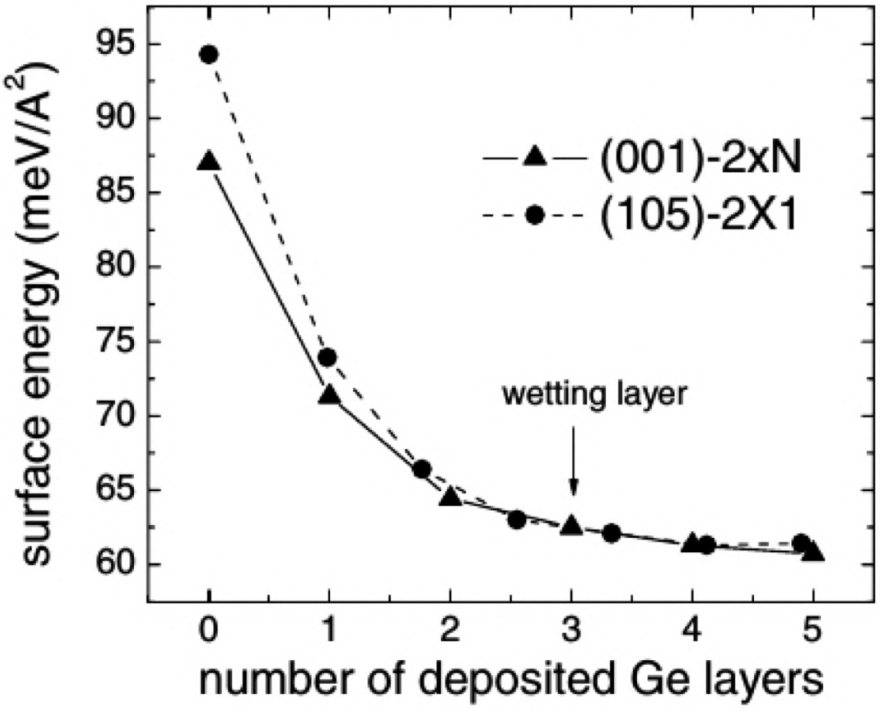

Figure 4: Surface energy densities of Ge/Si(001) and Ge/Si(105) as a function of the number of deposited Ge layers, obtained from ab-initio calculations. Image adapted from Ref. [48].

the interface is included in an additional term called *wetting potential*. The expression for the surface energy density of a Ge layer on Si then becomes $\gamma(h) = \gamma_{Ge} + W(h)$, where W is the wetting potential, expressed as:

$$W(h) = (\gamma_{Si} - \gamma_{Ge}) \cdot \exp\left(-\frac{h}{\delta}\right) \tag{20}$$

where $\gamma_{Ge} = 60$ meV/Å^2, $\gamma_{Si} = 87$ meV/Å^2 and δ, fitted from the data of Fig. 4, results to be $\delta = 0.27$ nm. When SiGe layers are considered, the surface energy density of the alloy will be considered as the linear combination of Si and Ge surface energies with the same approximation of perfect mixture discussed for the Vegard's law of Eq. (2).

The non-uniform definition of γ leads to an additional term in the surface chemical potential defined by (15). Considering also the free energy as function of h, $G = G(h)$, Eq. (15) gives an additional wetting term: $\mu_s = V_a(\gamma\kappa + W')$. The term W' is the derivative of the wetting potential and for the surface energy expressed by Eq.(20) yields:

$$W'_{sige}(h) = \frac{\gamma_{Ge} - \gamma_{Si}}{\delta} \exp\left(-\frac{h}{\delta}\right)$$

1.4.2 Dewetting potential

The surface diffusion equation presented above offers the possibility to treat also phenomena different from heteroepitaxy, but still determined by material transport at the surface of a solid. For example, some thin film systems can be deposited in a metastable condition and tend to dewet to form islands or solid droplets if heated to a sufficient temperature. This can happen at temperatures below the solid-liquid transition, thus producing a solid-state dewetting of the film via mass transport at its free surface. Some examples of materials showing this behavior are Ni thin films deposited on MgO substrate [49], Au films on graphite [50] or Au on silicon [51].

The results of the dewetting of a solid film is the formation of solid droplets and in analogy with the common treatment of liquids on substrate, a contact angle ϑ can be defined as the intersection between the film-substrate interface and the film-vacuum interface as in figure 5. The contact

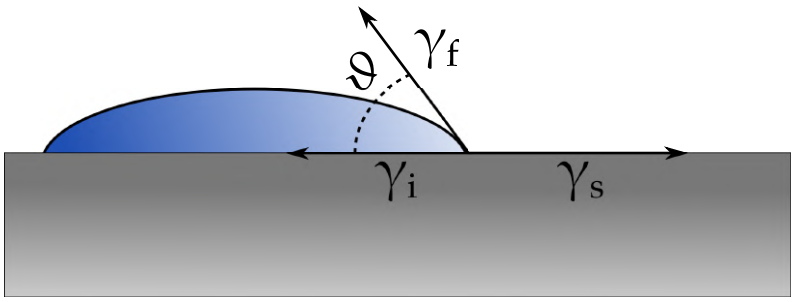

Figure 5: Contact angle ϑ defined by means of the equilibrium condition between the surface tensions of the droplet, γ_f, of the substrate, γ_s, and of the film-substrate interface, γ_i.

angle is entirely defined by the equilibrium condition for the surface tensions acting on the droplet: the film surface tension γ_f, the substrate surface tension γ_s and their interfacial surface tension γ_i, resulting in the equilibrium condition:

$$\gamma_s = \gamma_i + \gamma_f \cos\vartheta \tag{21}$$

In our treatment, the description of a contact angle between the film and the substrate will be modeld by means of a wetting potential able to reproduce the equilibrium condition of Eq. 21 when the retracting film edge touches the substrate. This wetting potential follows the description introduced by the work of Tripathi and O. Pierre-Luis [14] and reads:

$$W(h) = \gamma_0(1 - \cos\vartheta)(1 + \frac{5}{h^*}h)(\frac{h}{h} * -1)^5 \tag{22}$$

with γ_0 the surface energy density of the film and h^* a parameter defining a characteristic thickness for the wetting potential.

1.5 MISFIT DISLOCATIONS IN HETEROEPITAXIAL SYSTEMS

Elastic relaxation is not the only viable mechanism to obtain strain relaxation. Indeed, after a certain critical thickness, the film can lose its coherence with of the substrate. This mechanism consists in the plastic relaxation via insertion of defects in the lattice topology of the film, called *misfit dislocations* and sketched in figure 6.

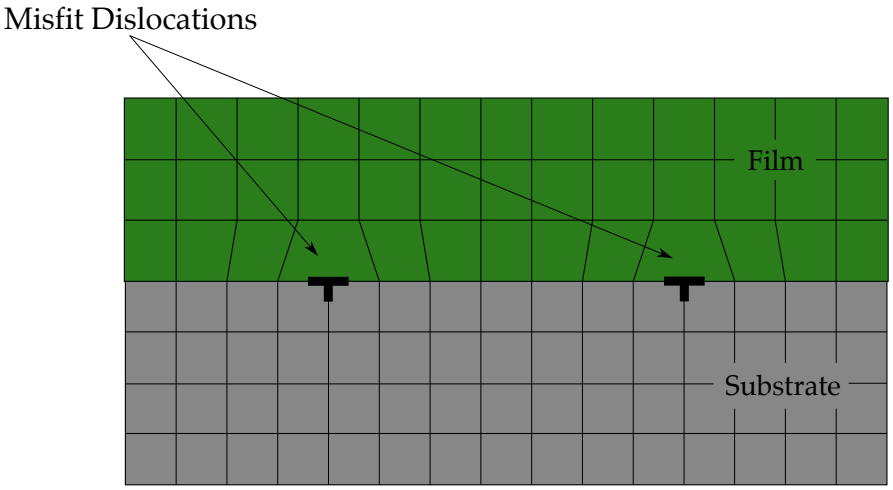

Figure 6: Sketch of the modified lattice topology in an heteroepitaxial film after the introduction of misfit dislocations.

Dislocations are line defects and in the direction of the dislocation line (normal to the paper in the figure) a whole plane of atoms is missing. The introduction of dislocations in a crystal produces a non-uniform strain field. However, on average, multiple dislocation partially relax the misfit strain, thanks to the extra space accommodated with the loss of the in-plane coherence between the film and the substrate.

Furthermore, even under conditions where elastic relaxation begins, the nucleated coherent islands tend to enlarge their height-to-base aspect ratio (AR) during the growth until a critical volume is reached. At this point the introduction of misfit dislocations is energetically favored and misfit defects are injected to further relax the misfit strain [23, 24, 25, 52, 53]. An introduction to the classical elastic theory of these defects will be the subject of the following chapter.

2 INTRODUCTION TO DISLOCATIONS

Dislocations are crystalline defects unavoidably introduced in the relaxation of a hetereopitaxial system. As we will see in chapters 4, 5 and 6 the nucleation and motion of dislocations will be the *fil rouge* linking all the systems considered in this Thesis. Thus, this chapter is entirely devoted to an introduction to the topic of dislocations in heteroepitaxy.

A number of different modeling approaches have been developed to study the nature of these defects depending on the space and time-scale under consideration, ranging from *ab initio* technique for the electronic structure to crystal plasticity approaches to predict the plastic flow of crystalline solids. As stated in the Introduction, in this Thesis the chosen approach is the discrete Dislocation Dynamics (DD) approach that is based on the linear elasticity theory. This model permits the description of dislocations behavior at the mesoscale, still mantaining the description of single defects. In this chapter we shall introduce the classical continuum theory of dislocations based on linear elasticity, while the description of the implementation of the DD model will be presented in Chapter 3.

2.1 BURGERS VECTOR

A dislocation is a line defect in the crystal lattice topology in which a line of atoms is mis-connected with respect to the perfect periodic structure of the crystal. The dislocation produces a displacement on the atoms near the missing plane, defined by a displacement vector known as *Burgers vector*, $\mathbf{b}$. The vector $\mathbf{b}$ can be defined geometrically by a construction known as *Burgers circuit*, depicted in figure 7, by drawing in a real crystal a closed clockwise circuit, which encloses the dislocations. Then we draw an equivalent circuit in a perfect crystal, with atoms in the ideal reference lattice. The vector required to close this second circuit is defined as the Burgers vector $\mathbf{b}$.

The orientations of these circuits are taken to be right-handed with respect to an oriented unit-vector normal to the page that defines the dislocation line ξ. A formal generalization of the definition of the vector $\mathbf{b}$ in a continuum approach can be done by taking the line integral of the derivative of the displacement field $\mathbf{u}$ over a circuit C oriented right-handed with respect to ξ:

$$\mathbf{b} = \oint_C \frac{\partial \mathbf{u}}{\partial l} \, dl \tag{23}$$

With these definitions it is now possible to distinguish two kind of dislocations. A defect with the Burgers vector perpendicular to the dislocation line is called an *edge dislocation*, while one with the Burgers vector parallel to the dislocation line is called *screw dislocation*. In a solid crystal a dislocation line

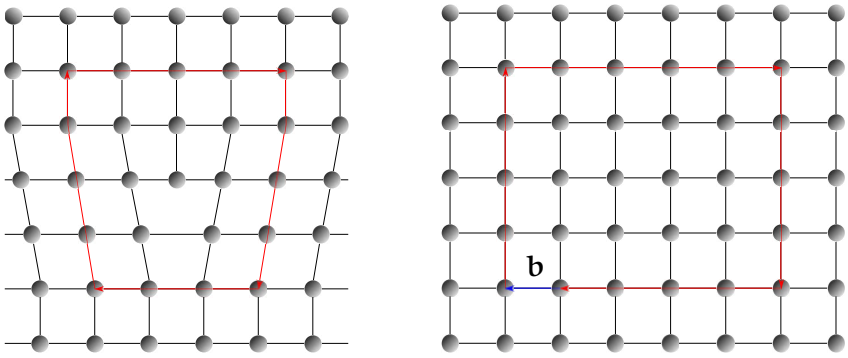

Figure 7: Two equivalent Burgers circuits. (a) Crystal with a dislocation present and (b) a perfect crystal. The vector **b** that closes the open circuit in (b) is defined as the Burgers vector of the dislocation.

and its corresponding Burgers vector belongs to specific crystalline orientation. Nevertheless, the Burgers vector can be decomposed in a component normal to the dislocation line, called the *edge component* of the dislocation and one component parallel to the dislocation line called the *screw component* of the dislocation.

2.2 VOLTERRA DISLOCATIONS

The derivation of the stress fields produced by dislocations is straightforward in an infinite isotropic medium. For this special case the displacement induced by the presence of a dislocation in a solid can be derived from simple geometrical considerations as reported in [54]. The strain and stress fields associated with this displacement are easily calculated by means of the linear elastic theory of section 1.2. Let us consider for examples a right-handed screw dislocation in a solid bulk, as shown in Fig. 8(a). This defect corresponds to one of the dislocation types studied by Volterra during the 19th century to describe deformations in continuum solid mechanic.

As we can see the Burgers vector of such a dislocation produces a shear displacement in the positive z direction. The result is that the displacement in z direction has a discontinuity at the cut surface shown in figure. In x and y directions the displacements are null, so $u_x = 0$ and $u_y = 0$, but the discontinuity in u_z yields:

$$\lim_{\substack{y\to 0 \\ x>0}} u_z(x,-y) - u_z(x,+y) = b_z$$

and we can assume, in an isotropic material, that this discontinuity is produced by a uniform increase of u_z with the polar angle ϑ. So the resulting expression for the displacement induced by this screw dislocation is:

$$u_z = b\frac{\vartheta}{2\pi} = \frac{b}{2\pi}\arctan\frac{y}{x}$$

The stress fields associated with this displacement are easily derived from

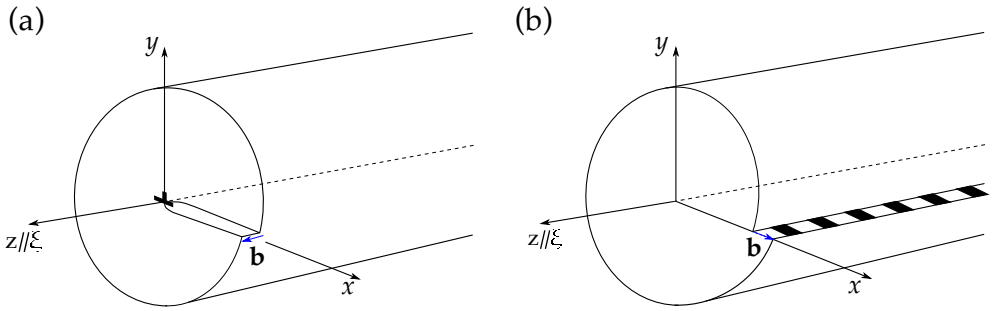

Figure 8: Dislocations as studied by Volterra to describe deformations of continuum solids. Dislocation line ξ, is parallel to the z axis, while the dislocations Burgers vector $\mathbf{b}$ is parallel to ξ for the screw dislocation in (a) and orthogonal for the edge dislocation in (b).

equations (4) and (6) yielding:

$$\sigma_{xz} = -\frac{\mu b}{2\pi}\frac{\sin\vartheta}{r} = -\frac{\mu b}{2\pi}\frac{y}{x^2+y^2}$$
$$\sigma_{yz} = \frac{\mu b}{2\pi}\frac{\cos\vartheta}{r} = \frac{\mu b}{2\pi}\frac{x}{x^2+y^2}$$
$$\sigma_{xx} = \sigma_{yy} = \sigma_{yy} = \sigma_{zz} = 0$$

The other possible kind of dislocation is the edge one, for which $\xi \cdot \mathbf{b} = 0$. This is another kind of dislocation studied by Volterra and can be represented as in figure 8(b). In figure we can see that the displacement in the direction of the dislocations line is null, so $u_z = 0$ and $\frac{\partial u_i}{\partial z} = 0$. The derivation of the remaining terms belongs to the class of problem of plane strain. The solution can be give in term of a stress function ψ known as Airy function (see [54] pag. 43 for reference). This function can be defined by noting that, for the condition of mechanical equilibrium:

$$\frac{\partial\sigma_{xx}}{\partial x} + \frac{\partial\sigma_{xy}}{\partial y} = 0 \qquad \frac{\partial\sigma_{xy}}{\partial x} + \frac{\partial\sigma_{yy}}{\partial y} = 0$$

and that these equations are immediately satisfied if σ_{xx}, σ_{yy} and σ_{xy} are defined in terms of function ψ as:

$$\sigma_{xx} = \frac{\partial^2\psi}{\partial y^2} \qquad \sigma_{yy} = \frac{\partial^2\psi}{\partial x^2} \qquad \sigma_{xy} = \frac{\partial^2\psi}{\partial x\partial y} \tag{24}$$

the function ψ can be derived from the conditions imposed above for an edge dislocation and yields:

$$\psi = -\frac{\mu b}{4\pi(1-\nu)}\log(x^2+y^2)$$

So, the stresses derived from definition of ψ as in (24) are

$$\begin{aligned}
\sigma_{xx} &= -\frac{\mu b}{2\pi(1-\nu)}\frac{y\left(3x^2+y^2\right)}{\left(x^2+y^2\right)^2}\\
\sigma_{yy} &= \frac{\mu b}{2\pi(1-\nu)}\frac{y\left(y^2-x^2\right)}{\left(x^2+y^2\right)^2}\\
\sigma_{zz} &= \nu(\sigma_{xx}+\sigma_{yy}) = -\frac{\mu\nu}{\pi(1-\nu)}\frac{by}{x^2+y^2}\\
\sigma_{xy} &= \frac{\mu b}{2\pi(1-\nu)}\frac{x\left(x^2-y^2\right)}{\left(x^2+y^2\right)^2}\\
\sigma_{xz} &= \sigma_{yz} = 0
\end{aligned}$$

Considering now a dislocation with Burgers vector generally oriented with respect to the dislocation line, we can provide the expressions for the stress field as linear superposition of the components derived before. So, by choosing a reference system with the z axis oriented along the dislocation line we can decompose the Burgers vector by projection on the axis of the reference system, $\mathbf{b} = (b_x, b_y, b_z)$. With this notation, the stress field for a dislocation with a generic Burgers vector are:

$$\begin{aligned}
\sigma_{xx} &= -\frac{\mu b_x}{2\pi(1-\nu)}\frac{y\left(3x^2+y^2\right)}{\left(x^2+y^2\right)^2} + \frac{\mu b_y}{2\pi(1-\nu)}\frac{x\left(x^2-y^2\right)}{\left(x^2+y^2\right)^2}\\
\sigma_{yy} &= -\frac{\mu b_x}{2\pi(1-\nu)}\frac{y\left(y^2-x^2\right)}{\left(x^2+y^2\right)^2} + \frac{\mu b_y}{2\pi(1-\nu)}\frac{x\left(x^2+3y^2\right)}{\left(x^2+y^2\right)^2}\\
\sigma_{zz} &= \nu(\sigma_{xx}+\sigma_{yy}) = \frac{\mu\nu}{\pi(1-\nu)}\frac{(b_y x - b_x y)}{x^2+y^2}\\
\sigma_{xy} &= \frac{\mu b_x}{2\pi(1-\nu)}\frac{x\left(x^2-y^2\right)}{\left(x^2+y^2\right)^2} - \frac{\mu b_y}{2\pi(1-\nu)}\frac{y\left(y^2-x^2\right)}{\left(x^2+y^2\right)^2}\\
\sigma_{yz} &= \frac{\mu b_z}{2\pi}\frac{x}{x^2+y^2}\\
\sigma_{xz} &= -\frac{\mu b_z}{2\pi}\frac{y}{x^2+y^2}
\end{aligned} \tag{25}$$

This stress fields are plotted in figure 9 for a dislocation with Burgers vector oriented at 60° with respect to the dislocation line.

2.2.1 Image effects on dislocations

Let us consider now a screw dislocation near the free surface of a system. The introduction of the surface requires, as seen for heteropitaxial systems in section 1.2.3, a condition of zero stress at the free surface. This requirement is easily obtained by means of an image construction in which the stress field in the system is obtained by the sum of stress fields of the dislocation itself and of an image dislocation placed symmetrically with respect to the free surface and opposite $\mathbf{b}$ of that of the dislocation, as shown in figure 10. This construction gives the required field in the physical region of the system, i.e.

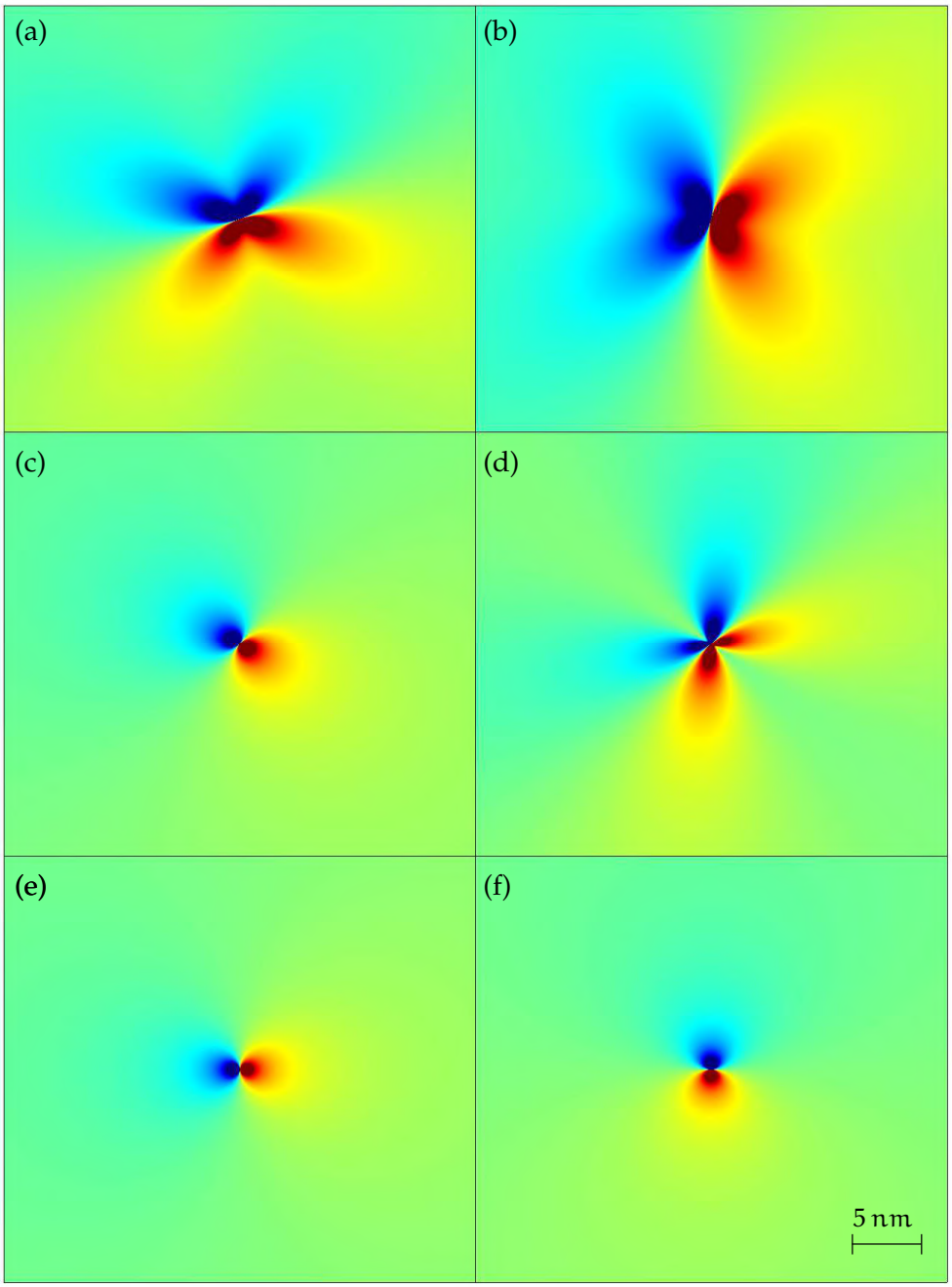

Figure 9: Components of a 60° dislocation stress field reported in equation (25) and plotted on the xy plane: (a) σ_{xx}, (b) σ_{yy}, (c) σ_{zz}, (d) σ_{xy}, (e) σ_{yz} and (f) σ_{xz}

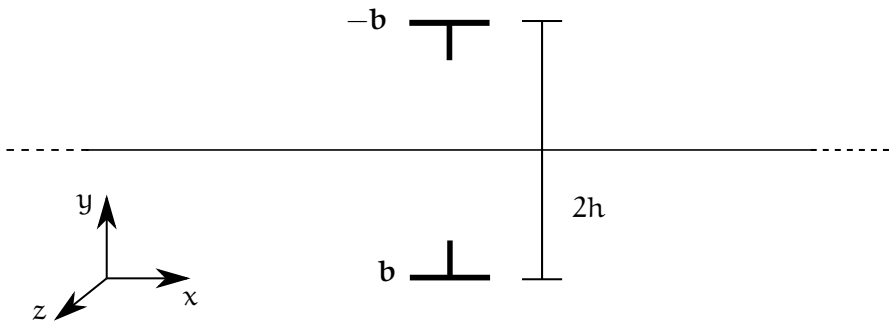

Figure 10: Scheme for the dipole construction used in this section. The image dislocation is in a position h above the free surface and with Burgers vector $-\mathbf{b}$ opposite to that of the real dislocation.

below the free surface, and meets the requirement of $\sigma \cdot \mathbf{n}$ on $y = 0$, as we can show explicitly:

$$\begin{aligned}\sigma_{yz} + \sigma_{yz}^{imm} &= \frac{\mu b}{2\pi}\frac{x}{x^2 + (-h)^2} - \frac{\mu b}{2\pi}\frac{x}{x^2 + h^2} \\ &= \frac{\mu b}{2\pi}\left[\frac{x}{(x^2 + h^2)} - \frac{x}{(x^2 + h^2)}\right] = 0\end{aligned}$$

The same holds for the other stress component σ_{xz}. Thus the stress fields of a screw dislocation near a free surface can be obtained by this simple dipole construction.

The correction of the bulk expressions must be accomplished also for the case of an edge dislocation near a free surface. For these dislocations there are two possibility for the orientation of the Burgers vector. The first one corresponds to $\mathbf{b} \cdot \mathbf{n} = 0$, i.e. $\mathbf{b}$ is perpendicular both to the dislocation line and to the free surface normal. The other possibility is $\mathbf{b} \cdot \mathbf{n} = b$, so the Burgers vector is parallel to the surface normal. In both these cases the condition for the zero stress at the free surface gives:

$$\sigma_{yy} = 0 \qquad \sigma_{xy} = 0 \qquad \text{at } y = 0 \tag{26}$$

This requirements can't be satisfied by the same dipole construction shown for a screw dislocation. Indeed, for the case with $\mathbf{b} \cdot \mathbf{n} = 0$ the sum of σ_{yy} of the real dislocation and its image yields:

$$\begin{aligned}\sigma_{xy} + \sigma_{xy}^{imm} &= 0 \\ \sigma_{yy} + \sigma_{yy}^{imm} &= \frac{\mu b}{2\pi(1-\nu)}\left[\frac{h\left(x^2 - h^2\right)}{\left(x^2 + h^2\right)^2} + \frac{h\left(x^2 - h^2\right)}{\left(x^2 + h^2\right)^2}\right] \\ &= 2\sigma_{yy}\end{aligned}$$

Also the other kind of edge dislocation, with $\mathbf{b} \cdot \mathbf{n} = b$ can't satisfy the condition (26) with the addition of a dipole term, and indeed it gives:

$$\begin{aligned}
\sigma_{yy} + \sigma_{yy}^{imm} &= 0 \\
\sigma_{xy} + \sigma_{xy}^{imm} &= \frac{\mu b}{2\pi(1-\nu)} \left[\frac{h\left(h^2 - x^2\right)}{\left(x^2 + h^2\right)^2} - \frac{(-h)\left(h^2 - x^2\right)}{\left(x^2 + h^2\right)^2} \right] \\
&= 2\sigma_{xy}
\end{aligned}$$

This results show that the dipole construction does not give the exact stress field for a system with a free surface when edge dislocations are considered, while it is exact for a screw one. In the following section is shown an exact solution also for the edge component of a dislocation near of a free surface.

2.2.2 Head correction for a free surface

As seen in the previous section, the effect of the presence of a free surface on a dislocations cannot be described by a simple dipole image construction, because the edge components of the dislocation stress field don't satisfy the requirement of zero normal stress at the surface $\boldsymbol{\sigma} \cdot \mathbf{n} = 0$. This problem was resolved by Head in the 50's and the corrected stress functions are reported in literature [55]. The exact solution requires a correction to the dipole construction, so that the total field results in:

$$\sigma^{total} = \sigma_{ij} + \sigma_{ij}^{dipole} + \sigma_{ij}^{Head}$$

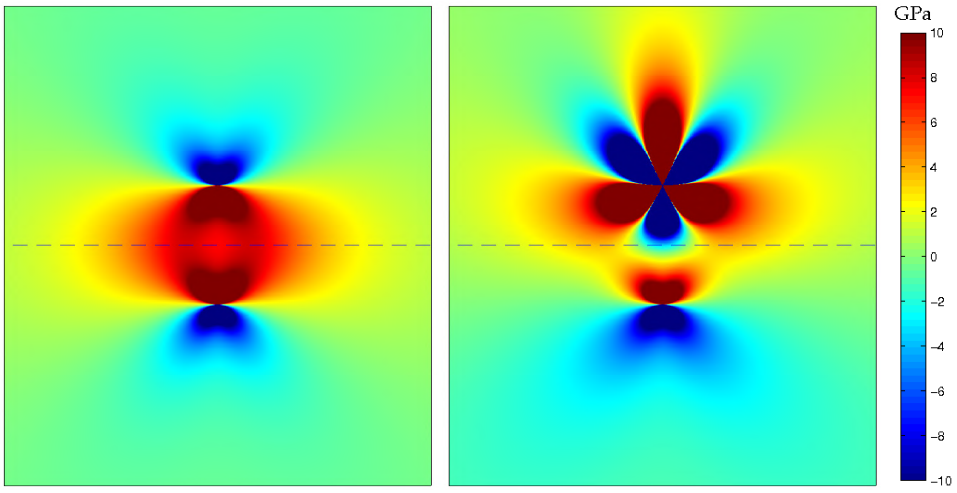

Figure 11: Comparison between the stress field of an edge dislocation near a free surface with a dipole construction on the left and the Head correction on the right. The region with physical meaning is only that below the dashed line.

This third term depends on the distance of the dislocation from the free surface and added to the other two solves the problems discussed in the

previous sections for the edge dislocations, both for the case $\mathbf{b}\cdot\mathbf{n}=0$ and $\mathbf{b}\cdot\mathbf{n}=b$. The resulting complete stress fields are:

$$
\begin{aligned}
\sigma_{xx} =& \frac{Eb_x}{4\pi(1-\nu^2)}\left[\frac{(y-h)\left[(y-h)^2+3x^2\right]}{\left[(y-h)^2+x^2\right]^2}-\frac{(y+h)\left[(y+h)^2+3x^2\right]}{\left[(y+h)^2+x^2\right]^2}\right.\\
&\left.-\frac{2h\left[6x^2y(h-y)+(-h-y)(h-y)^3+x^4\right]}{\left[(y-h)^2+x^2\right]^3}\right]\\
&+\frac{Eb_y x}{4\pi(1-\nu^2)}\left[\frac{(y-h)^2-x^2}{\left[(y-h)^2+x^2\right]^2}-\frac{4h\left[x^2(2h-3y)+(y-h)^2(2h+y)\right]}{\left[(y-h)^2+x^2\right]^3}\right.\\
&\left.-\frac{(h+y)^2-x^2}{\left[(h+y)^2+x^2\right]^2}\right]\\
\sigma_{yy} =& \frac{Eb_x}{4\pi\left(1-\nu^2\right)}\left[\frac{(y-h)\left[(y-h)^2-x^2\right]}{\left[(y-h)^2+x^2\right]^2}-\frac{(h+y)\left[(y+h)^2-x^2\right]}{\left[(y+h)^2+x^2\right]^2}\right.\\
&\left.+\frac{2h\left[6x^2y(h-y)+(y-h)^3(3y-h)-x^4\right]}{\left[(y-h)^2+x^2\right]^3}\right]\\
&+\frac{Eb_y}{4\pi(1-\nu^2)}\left[\frac{4hxy\left(3(y-h)^2-x^2\right)}{\left((y-h)^2+x^2\right)^3}-\frac{x\left(3(y-h)^2+x^2\right)}{\left((y-h)^2+x^2\right)^2}\right.\\
&\left.+\frac{x\left[3(h+y)^2+x^2\right]}{\left[(h+y)^2+x^2\right]^2}\right]\\
\sigma_{zz} =& \nu(\sigma_{xx}+\sigma_{yy})\\
\sigma_{xy} =& \frac{b_y E}{4\pi\left(1-\nu^2\right)}\left[\frac{(-2h+y-yo)\left[(2h-y+yo)^2-x^2\right]}{\left[(2h-y+yo)^2+x^2\right]^2}\right.\\
&\left.+\frac{2h\left(6x^2(h-y+yo)(2h-y+yo)+(y-yo)(2h-y+yo)^3-x^4\right)}{\left((2h-y+yo)^2+x^2\right)^3}\right]\\
&-\frac{b_x E}{4\pi\left(1-\nu^2\right)}\left[\frac{4hx(h-y+yo)\left(3(2h-y+yo)^2-x^2\right)}{\left((2h-y+yo)^2+x^2\right)^3}\right.\\
&\left.-\frac{x\left((2h-y+yo)^2-x^2\right)}{\left((2h-y+yo)^2+x^2\right)^2}\right]
\end{aligned}
\tag{27}
$$

As we can see in figure 11, the resulting stress field differs from the case of the image construction particularly in the region of the free surface.

2.3 DISLOCATION ARRAYS NEAR A FREE SURFACE

The stress field for a single dislocation running along z direction, including the corrections evaluated by Head in Ref. [55] to account for the presence of the free surface, is reported in Eq. (27). A closed solution for the stress field of an array of such dislocation can be obtained by summing the contribution coming from infinite dislocations displaced by a distance L from each other. The complete derivation of this sum is reported in Appendix A. Here we report the final solution in terms of the stress field. Using the same notation of Eq. (58), the analytical expressions for the stress fields of an array of dislocation with periodicity L, at a distance h from the free surface and a generic Burgers vector $\mathbf{b}=(b_x,b_y,b_z)$ are:

$$
\begin{aligned}
\sigma_{xx}^{xPBC} &= \frac{\mu b_x}{(1-\nu)L}\left[\frac{\pi Y_+(C_{Y_+}c_X-1)-S_{Y_+}\left(C_{Y_+}-c_X\right)}{\left(c_X-C_{Y_+}\right)^2}-\frac{\pi Y_-(C_{Y_-}c_X-1)-S_{Y_-}\left(C_{Y_-}-c_X\right)}{\left(c_X-C_{Y_-}\right)^2}\right]\\
&-\frac{\pi\mu b_x h}{(1-\nu)L^3}\left[\frac{-2\pi y\left(c_{2X}-3\right)S_{Y_-}-L\left(c_{2X}+3\right)C_{Y_-}+c_X\left(LC_{2Y_-}-2\pi yS_{2Y_-}\right)+3Lc_X}{\left(c_X-C_{Y_-}\right)^3}\right]\\
&+\frac{\mu b_y s_X}{2(1-\nu)L}\left[\frac{C_{Y_+}-c_X-2\pi Y_+S_{Y_+}}{\left(c_X-C_{Y_+}\right)^2}-\frac{C_{Y_-}-c_X-2\pi Y_-S_{Y_-}}{\left(c_X-C_{Y_-}\right)^2}\right]\\
&+\frac{2\pi\mu b_y h}{(1-\nu)L^2}\left[\frac{\pi Ys_XC_{2Y_-}-3\pi Ys_X+s_{2X}S_{Y_-}-s_XS_{2Y_-}+4\pi Ys_{2X}C_{Y_-}}{\left(c_X-C_{Y_-}\right)^3}\right]\\
\sigma_{yy}^{xPBC} &= -\frac{\mu b_x\pi}{(1-\nu)L}\left[\frac{Y_+\left(C_{Y_+}c_X-1\right)}{\left(c_X-C_{Y_+}\right)^2}-\frac{Y_-\left(C_{Y_-}c_X-1\right)}{\left(c_X-C_{Y_-}\right)^2}\right]\\
&-\frac{\pi\mu b_x h}{(1-\nu)L^2}\left[\frac{2\pi Y\left(c_{2X}-3\right)S_{Y_-}-\left(c_{2X}+3\right)C_{Y_-}+c_X\left(C_{2Y_-}+2\pi YS_{2Y_-}\right)+3c_X}{\left(c_X-C_{Y_-}\right)^3}\right]\\
&+\frac{\mu b_y s_X}{2(1-\nu)L}\left[\frac{2\pi Y_+S_{Y_+}+C_{Y_+}-c_X}{\left(c_X-C_{Y_+}\right)^2}-\frac{2\pi Y_-S_{Y_-}+C_{Y_-}-c_X}{\left(c_X-C_{Y_-}\right)^2}\right]\\
&-\frac{2\pi\mu b_y hY}{(1-\nu)L^2}\left[\frac{\pi s_X\left(C_{2Y_-}-3\right)+\pi s_{2X}C_{Y_-}}{\left(c_X-C_{Y_-}\right)^3}\right]\\
\sigma_{zz}^{xPBC} &= \nu(\sigma_{xx}^{xPBC}+\sigma_{yy}^{xPBC})\\
\sigma_{xy}^{xPBC} &= \frac{\mu b_x s_X}{2(1-\nu)L}\left[\frac{(C_{Y_+}-c_X)-2\pi Y_+S_{Y_+}}{\left(c_X-C_{Y_+}\right)^2}-\frac{(C_{Y_-}-c_X)-2\pi Y_-S_{Y_-}}{\left(c_X-C_{Y_-}\right)^2}\right]\\
&-\frac{2\pi\mu b_x hY}{(1-\nu)L^2}\left[\frac{\pi s_X\left(C_{2Y_-}-3\right)+\pi s_{2X}C_{Y_-}}{\left(c_X-C_{Y_-}\right)^3}\right]\\
&-\frac{\mu b_y\pi}{(1-\nu)L}\left[\frac{Y_+\left(C_{Y_+}c_X-1\right)}{\left(c_X-C_{Y_+}\right)^2}-\frac{Y_-\left(C_{Y_-}c_X-1\right)}{\left(c_X-C_{Y_-}\right)^2}\right]\\
&-\frac{\pi\mu b_y h}{(1-\nu)L^2}\left[\frac{-2\pi Y\left(c_{2X}-3\right)S_{Y_-}-\left(c_{2X}+3\right)C_{Y_-}+c_X\left(C_{2Y_-}-2\pi YS_{2Y_-}\right)+3c_X}{\left(c_X-C_{Y_-}\right)^3}\right]\\
\sigma_{yz}^{xPBC} &= \frac{\mu b_z}{2L}\left[\frac{s_X}{C_{Y_+}-c_X}-\frac{s_X}{C_{Y_-}-c_X}\right]\\
\sigma_{xz}^{xPBC} &= -\frac{\mu b_z}{2L}\left[\frac{S_{Y_+}}{C_{Y_+}-c_X}-\frac{S_{Y_-}}{C_{Y_-}-c_X}\right]
\end{aligned}
$$

The above formulae define the stress field of an array of dislocations running along the z direction. The stress field produced by a net of dislocations as in figure 59 can be obtained by summing this contribution with the one arising from a second array of dislocations running along the x direction. This can be achieved by a simple rotation of the reference system around the y axis of the functions reported above. The results is plotted in Fig. 12 where the hydrostatic stress field produced by a 2D network of dislocations $\sigma_{xyz} = \sum_i \sigma_{ii}$ is reported. Here also the effect of a biaxial stress field is added in the region above the plane containing the dislocation network, in order to mimick an heteroepitaxial system.

2.4 FORCE ON DISLOCATIONS

Let us now consider a solid in mechanical equilibrium which contains a dislocation and with an external stress field applied. The total free energy of the

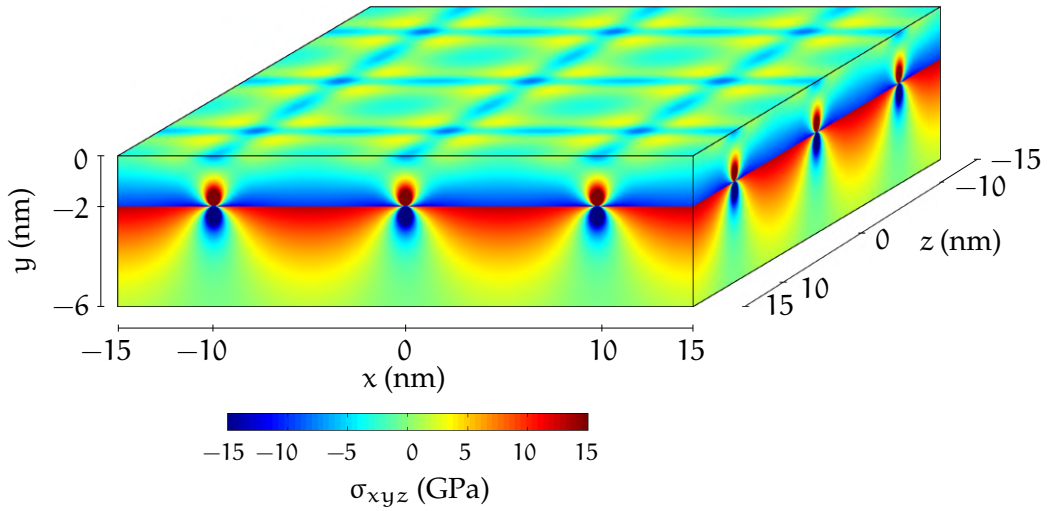

Figure 12: 3D plot of the hydrostatic stress field σ_{xyz} produced by a two dimensional net of edge dislocations with periodicity of 10 nm and placed at the interface of a biaxially stressed heteroepitaxial system.

system depends on the total elastic energy stored by the dislocation and the solids itself. According to a general thermodynamical principle the dislocation will move accordingly in order to minimize the total free energy. Thus, defining η as a general coordinate describing the dislocation line position, the force $\mathbf{F}$ acting on the dislocation will be given by the negative gradient of the total elastic energy:

$$\mathbf{F} = -\nabla_\eta E_{tot} \tag{28}$$

This expression is commonly written as the Peach-Koehler [54] equation:

$$\mathbf{F} = (\mathbf{b} \cdot \boldsymbol{\sigma}) \times \boldsymbol{\xi} \tag{29}$$

From Eq. (29) we can see that the force acting on a dislocation is always normal to the dislocation line $\boldsymbol{\xi}$. $\mathbf{F}$ can be further decomposed in a *glide* component along the plane containing the dislocations and a *climb* component normal to that. While under certain conditions it is possible to observe climb motion in heteroepitaxial systems [56], this has a much higher energy barrier than glide motion. Thus, in the remainder when treating dislocation motion we will focus exclusively on glide motion of dislocation segments on their glide planes.

2.4.1 Line tension

In the absence of an applied external stress a dislocation will straighten out in order to minimize its line lengths and strain energy. For the same reason a closed loop of dislocation will tend to collapse. The concept of *line tension* of a dislocation is defined in analogy with the line tension of a stretched elastic string. Formally the line tension is defined as the derivative of the dislocation self-energy E_{el} with respect to its line length L:

$$\Gamma = \frac{dE_{el}}{dL} \tag{30}$$

E_{el} can be defined as the elastic energy associated to the deformation field of the dislocation itself.

This concept implies that a dislocation loop of radius R will collapse if not equilibrated by an external stress field. It is thus possible to define a critical stress τ_a as the resolved shear stress needed to maintain an equilibrium between the force exerted on the loop by the external field and the line tension of the loop itself. This quantity can be evaluated once an expression for the line tension of Eq. (30) is provided. Different analytical procedures, based on an approximate expression of Eq. (30) can be found in literature. Here we report the results of the derivation described by Friedel [57]:

$$\tau_a(R) = \frac{\mu b}{4\pi R} \ln\left(\frac{R}{r_0}\right) \tag{31}$$

where r_0 is a cut-off radius and μ is the shear modulus of the material. This expression is plotted in Fig. 13 against corresponding results obtained from Dislocation Dynamics simulations that will be described in section 3.1. These results provide a condition for the insertion of a dislocation loops in a DD simulation of an heteroepitaxial system. Indeed, for a given magnitude of the biaxial stress caused by the lattice mismatch, only dislocation loops with radius equal or bigger than a certain critical value can open during the simulation.

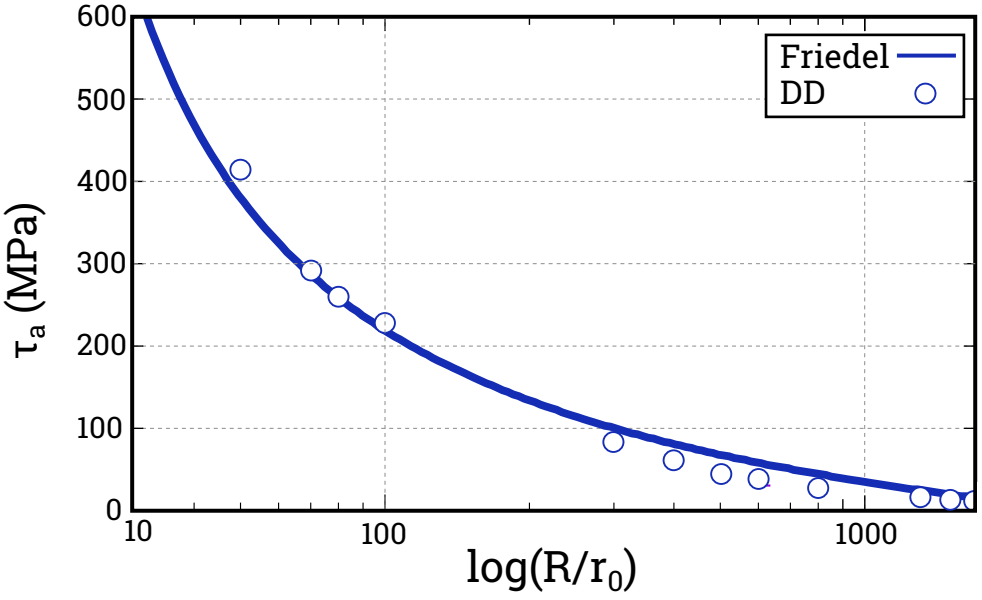

Figure 13: Critical resolved shear stress τ_a as function of the radius R of the dislocation loop. The predicion of the analytical model of Friedel is plotted against results obtained from DD simulations as described in section 3.1.

2.4.2 Dislocation velocity

As seen above, the force per unit length acting on a dislocation element due to an external stress field is given by the Peach-Koheler expression (29). If we are interested in evaluating the resulting glide velocity we can further decompose this force into an *effective* glide force, that is the component projected in the slip plane along the direction of the Burgers vector.

Modeling the velocity of single dislocation can be done in different ways according to the magnitude of the applied stress field and to the environment where it is moving, as the symmetry of the lattice or the presence of other crystal defects. Considering the mean effects of the crystal friction on the dislocation segment, its motion can be described as in the presence of a viscous coefficient B by the equation:

$$m_0 \frac{dv}{dt} + Bv = \tau_a b \tag{32}$$

where $m_0 = \rho_0 b^2$ represents the effective mass of the dislocaiton, with ρ_0 being the density of the medium. B and the solutions of this equation have the form:

$$v = v_s[1 - \exp -t/t_s] \tag{33}$$

This last equation show that after a steady-state velocity v_s is reached in a caracteristic time t_s:

$$v_s = \tau_a b/B \qquad t_s = m_0/B = \rho_0 b^2/B$$

the typical order of magnitude for the transient time t_s is about $10^{-10} \approx 10^{-11}$s that results in a traveled distance spanned by the dislocation line of the order of the nanometer in this transient regime. If this initial accelarated motion can be neglected the velocity equation (33) simply becomes:

$$v_s = \frac{\tau_a b}{B} \tag{34}$$

this is the free-flight velocity for a straight dislocation segment moving under an effective stress τ_a.The implementation of this equation in the Dislocation Dynamics approach will be described in chapter 3.

2.5 DISLOCATIONS IN HETEROEPITAXIAL SYSTEMS

As we have already introduced the system under study in this Thesis is composed of a thin film of germanium grown on a substrate of silicon. This represents an example of heteropitaxial growth in which both the film and the substrate have a diamond-like crystal structure. In crystals the most favorable Burgers vectors associated to a dislocation depends on the space arrangements of the atoms in the crystal. So, as we can see in figure 14, the possible directions for the Burgers vectors in FCC crystals lie on the edges of a tetrahedron, known as the Thompson tetrahedron. The facets of this tetrahedron corresponds to {111} planes, known as the *glide planes* of the dislocations. These are translation vectors for the lattice and by moving on the corresponding glide plane the dislocation can glide through the crystal onely by means of a rearrangement of atomic bonds.

The process of injection of a dislocation in a heteroepitaxial film is the subject of several investigation [58]. Despite the details about the nucleation procedure are still not totally clarified, a generic picture can be drawn as in Fig. 15. Starting from a closed loop (or a semi-loop) on a {111} plane in the

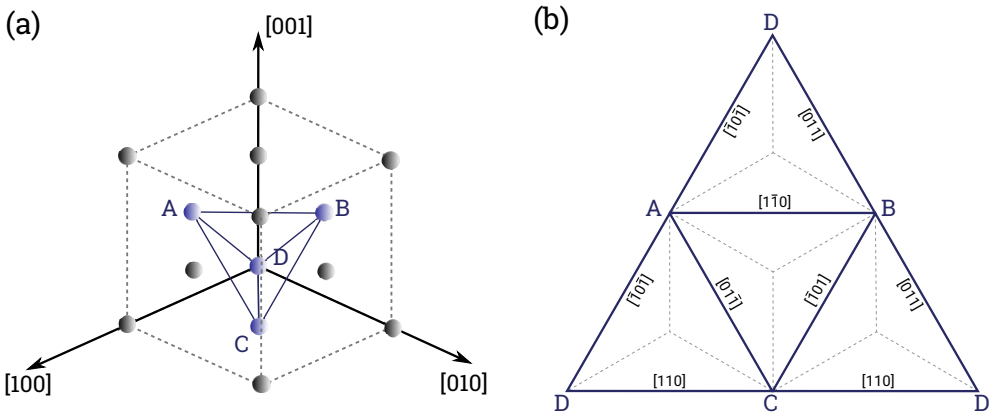

Figure 14: Possible orientations for the Burgers vector of a dislocation in a fcc crystal. The nearest neighbour points represents the directions of the most probable Burgers vectors for a dislocation and lie on the edge of a tetrahedron. If AB is the dislocation line, a Burger vector along AB itself represent a screw dislocation, one along DC an edge dislocation and one along AD, AC, BC or BD an edge dislocation.

film, the dislocation opens under the influence of the biaxial misfit strain. During this process the loop will eventually encounter the free surface and thus will open forming a semi-loop with two *threading arms* running through the layer. Furthermore, the loop will encounter the film-substrate interface and will deposit a dislocation segment that is called a *misfit dislocation* (MD). From this picture it is easy to understand that the direction of the misfit segments lies at the intersection of the {111} planes with the growth plane. For the case of growth on (001) substrates, MDs are thus oriented along ⟨110⟩ directions. With Burgers vector belonging to ⟨011⟩ directions, the loop will then deposit MD known as 60° *dislocations*, due to the angle between their Burgers vector and their dislocation line.

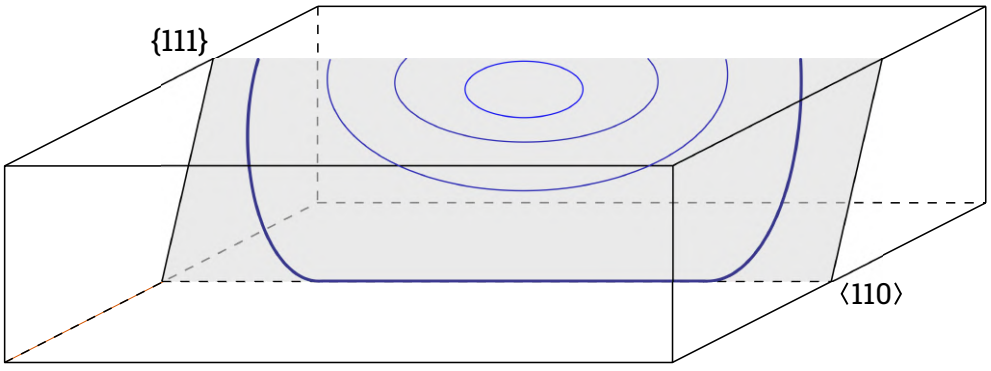

Figure 15: Schematic illustration showing the opening of a dislocation loop in a heteroepiaial system. The loop glides on the {111} plane and opens when it reaches the free surface. The misfit segment deposited at the interface lies along a ⟨110⟩ direction.

2.5.1 Critical thickness

Critical thickness is defined as the film thickness at which the energy difference in the system before and after the introduction of the dislocation is negative. So when:

$$\Delta E(h_c) = E_{dislocation}(h_c) - E_{film}(h_C) = 0 \tag{35}$$

the system has reached its critical thickness. By disregarding the difference in elastic constants between SiGe and Si, it is sufficient to add a trivial biaxial misfit stress in the SiGe film to the stress expressions defined in section 2.3 to obtain the complete stress field in a dislocations in a SiGe/Si system. Integrating the total elastic energy in the system with and without the dislocation yields the possibility to evaluate Eq. 35. Results for various Ge content x are reported in figure 16 for the representative cases of an edge and a 60° dislocation and compared to the well-known Matthews and Blakeslee formulation [59, 60]. Notice that this procedure yields results pretty similar to the very simple Matthews and Blakeslee model. In this approach the critical thickness is describe as the condition at which the total resolved shear stress on a threading dislocation is sufficient to start bending it. At this point the moving threading will deposit a segment at the interface and thus producing the formation of a misfit dislocation.

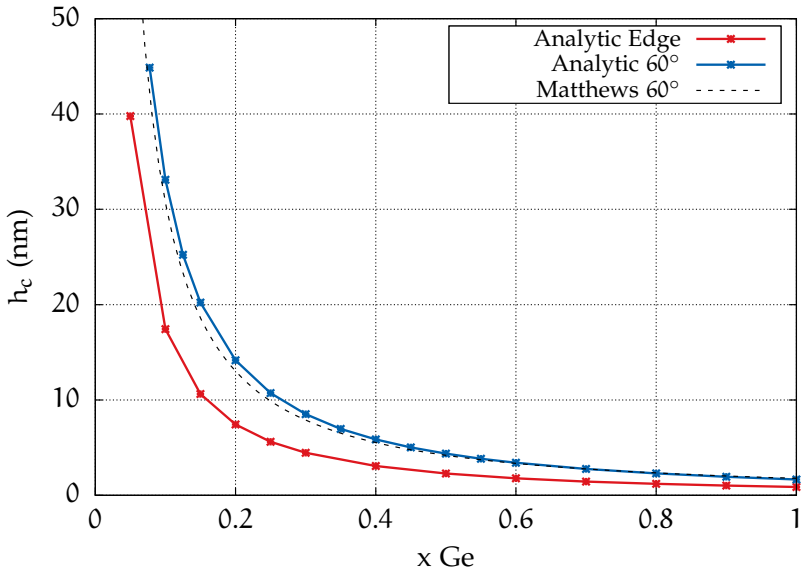

Figure 16: Comparison between calculated critical thickness layer h_c using a numerical integration of the elastic energy in the system and Matthews and Blakeslee criterion presented in Refs. [59, 60].

By exploiting the expression for an array of dislocation present in Appendix 2.3 we can further develop this evaluation. Defining the optimal distance d_0 between MDs in an array as the one that gives on average full strain relaxation:

$$d_0 = \frac{b_x}{\langle \varepsilon_{xx} \rangle} \tag{36}$$

we can now evaluate the distance d between edge dislocations in an array minimizing the total energy at an assigned film height h. In figure 17 we

plot this value normalized to d_0 for different Ge concentrations x. As we

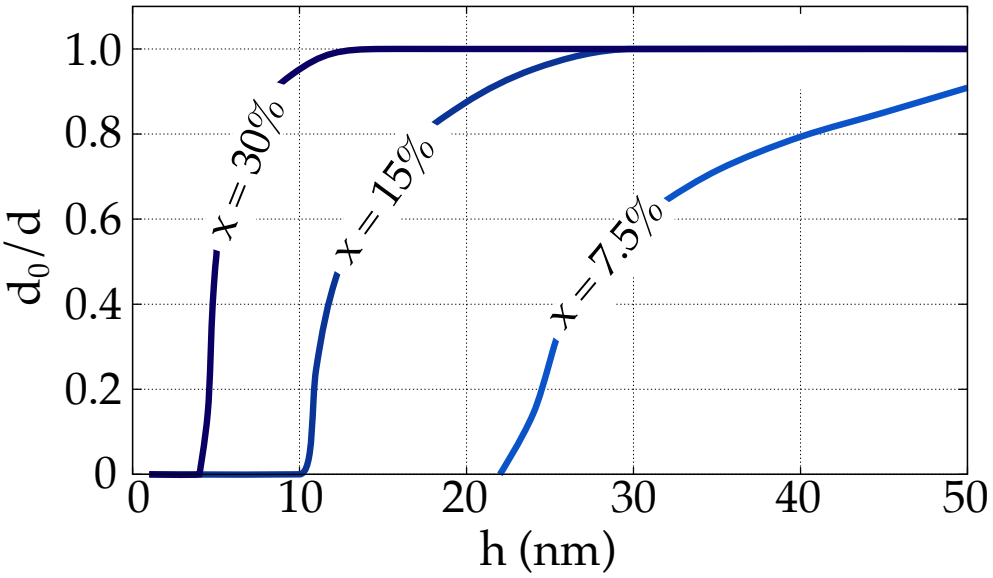

Figure 17: Optimal dislocation spacing d for different values of Ge composition x is plotted against film thickness h. Above the critical thickness this curves rapidly converge to the optimal dislocation spacing.

can see the transition between a non critical film, i.e. when the film can not sustain the presence of a single dislocation and so the spacing d in the array tends to infinity, and the fully relaxed film, when $d = d_0$ is sharper with increasing Ge concentration, as the driving force for the introduction of dislocations depends on the elastic energy stored in the film.

2.5.2 Dislocations in constant composition and graded layers

The distribution of dislocations in plastically-relaxed flat film is a rather complex topic and generally depends on the composition of the film and the growth parameters. A generalized theory of dislocations distribution in heteroepitaxial systems cannot be drawn since dislocations are high energy defects and their nucleation is usually the result of an irreversibile process. Thus, a thermodynamical equilibrium theory for their description do not exist. However, for the notable cases of constant composition and linear graded systems some general considerations can be made. These two systems are widely studied in literature (see Refs. [61]) and will be the subject of several investigations reported in this Thesis, as we shall see in chapters 5 and 6.

In constant composition films, the Matthews and Blakslee analysis for the critical thickness presented can be used to predicted the critical thickness for nucleation of dislocations. However, as soon as the film thickness exceed the critical thickness every position in the film would be equally favored for the introduction of a dislocation. In real systems injection of dislocation follows kinetic considerations and the presence of local defects or sources can favor the insertion of dislocations in specific positions [58]. However, when multiple sources are activated the nucleation of dislocations starts simultaneously in different positions resulting in the deposition of a two-dimensional network of misfit dislocations as can be aprreciated in Fig. 18.

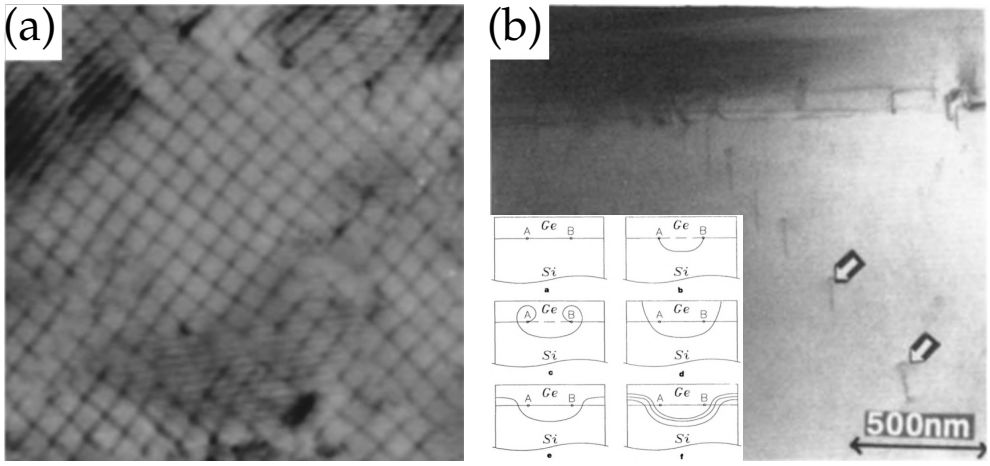

Figure 18: Examples of heteroepitaxial films relaxed by dislocations. In (a) a top view TEM image reveals a two-dimensional net of edge dislocations. Image adapted from Ref. [56]. In (b) a cross-sectional TEM of a heteroepitaxial film reveals the typical pileup of dislocation generated by the Frank-Read mechanism as sketched in the inlay. Image adapted from Ref. [62]

The linear grading of the Ge composition is another common growth modality in heteroepitaxy. This procedure is reported to have an effect on dislocations position and threading arms [62, 61]. The usual picture of the relaxation process in graded layers is considered to be an heterogenous nucleattion of dislocations from specific sources. This is due to the paucity of activated nucleation sources with respect to a constant composition film. The result is the injection of multiple identical defects from just a few nucleation sources. This process corresponds to the *Frank-Read* or the *modified Frank-Read* mechanism [63, 62, 61, 64]. In this case dislocations tend to form structures known as pileups, depicted in figure 18(b), where all dislocations are injected as loops from the source and start to extend themselves on their glide plane as shown in the inlay of figure 18(b). The result of this mechanism is the formation of structures of dislocations disposed on a single glide plane, known as *pileups* of MDs, well illustrated in the cross-sectional TEM image of Fig 18(b).

An explanation of the vertical distribution of dislocations in graded layers is provided by Tersoff in Ref. [65]. There, the author modeled the dislocation distribution in terms of a mean dislocation density ρ_{disl} and was able to derive by thermodynamical considerations the equilibrium configuration for this density as:

$$\rho_{disl} = \frac{\varepsilon(y)'}{b} \tag{37}$$

where $\varepsilon(y)'$ refers to the derivative of strain with respect to the vertical position y. So, for a linearly increasing graded layer the predicted density is expected to be constant.

3 MODEL DESCRIPTION

In this chapter we shall present the models developed during this Thesis to tackle elastic and plastic relaxation. These are continuum models developed on the framework of the Linear Elasticity Theory introduced in section 1.2. All the models here presented require the possibility to numerically solve Partial Differential Equations (PDEs). This is accomplished by exploiting the Finite Element Method (FEM).

The description of the plastic relaxation is performed by means of the Dislocation Dynamics (DD) approach that is discussed in section 3.1. In this Thesis we exploited the microMegas DD code [66]. In the same section an extension required to tackle the presence of free-surfaces, called Discrete Continuos Model (DCM) [15] is also introduced. When presenting the DCM, a discussion on the numerical solution of the PDE for mechanical equilibrium by means of the FEM approach is also reported.

The development of a model able to tackle elastic relaxation in heteroepitaxy requires the possibility to solve the PDE for surface diffusion discussed in section 1.3. Coupling this equation with the mechanical equilibrium condition permits to describe the evolution of the surface morphology of the epilayer during the growth. The implementation of this model is presented in section 3.2.

3.1 DISLOCATION DYNAMICS

In the Dislocation Dynamics (DD) [66, 67] approach the description of the evolution of a given dislocation configuration is made by means of a spatial discretization of each dislocation line into small segments with a given resolution Δl as in Fig. 19. Exploiting this discretization, the evolution of the dislocation line can be modeled by the movement of all its composing segments, where each one experience a driving force $\mathbf{F}$ given by the Peach-Koheler equation introduced in section 2.4:

$$\mathbf{F} = (\boldsymbol{\sigma} \cdot \mathbf{b}) \times \boldsymbol{\xi} \tag{38}$$

where $\mathbf{b}$ is the dislocation Burgers vector, $\boldsymbol{\xi}$ the direction of the considered segment and $\boldsymbol{\sigma}$ the local stress tensor. The latter can be due to the self-interactions with other segments composing the same dislocation line, to the interaction with other dislocations and to applied external stress loads like the heteroepitaxial biaxial stress field. The interaction between adjacent segments belonging to the same dislocation line is evaluated by means of a line tension approximation of Eq. 30. This is done in order to avoid numerical artifacts due to the divergence of the stress fields close to the segment positions. At each timestep t of the simulation, once all the acting forces have been evaluated, the dynamics is described (in the assumption of free-

flight dislocation movement, i.e. temperature high enough to activate glide motion [1]) by evaluating the velocity v_s of each segment starting from the equation discussed in section 2.4.2:

$$v_s = \frac{\tau_a b}{B} \tag{39}$$

where τ_a is the resolved shear stress obtained by projecting the force $\mathbf{F}$ of Eq. (38) on the glide plane of the considered dislocation loop, b is the modulus of the Burgers vector (0.3841 nm for Si) and B is a friction coefficient typical of the considered material (5.5×10^{-5}Pa $\cdot$ s for Si). In this way the code can displace each segment individually, eventually handling the possibility of local interactions between them. At this stage of the simulation also the discretization of the dislocation lines is recomputed if needed. Then the above described procedure is iterated starting from the resulting configuration of dislocations and recomputing the forces by means of Eq. (38) in order to describe the evolution for the following time-steps.

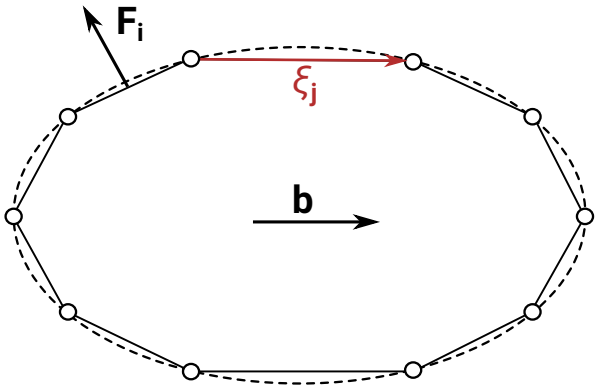

Figure 19: Discretization of a dislocation loop of Burgers vector b into small segments of dimension Δl and line direction ξ_j. The Peach-Kohler forces F_i can be evaluated on each of the discretized segments individually.

An example of a DD simulation showing the opening of a dislocation loop under the influence of a biaxial stress field is reported in Fig. 20. In this simulation a dislocation loop of radius 50 nm and Burgers vector oriented along the [011] direction is opening under the effect of a resolved shear stress of 200 MPa. The results of this kind of simulations have been already discussed in section 2.4.1 in order to provide a comparison with the analytical model of Friedel [57] for the critical stress required to open dislocation loops.

In order to correctly simulate the stress field of a dislocation in a thin film, the requirement of zero normal stress at the surface ($\sigma \cdot \mathbf{n} = 0$) must be satisfied in order to compute the correct stress field to be used in Eq. (29). Analytical solutions are known for the case of straight dislocations segments lying parallel to the free surface (see section 2.2.2), but a general treatment of the dislocation line cannot be done without numerically evaluating the stress field by means of a Finite Element (FE) solver. Indeed, the stress field produced by dislocation segments are known analytically only for bulk systems [54]. Furthermore, accounting for the presence of non-homogenous loadings resulting from a generic geometry of the system, as in the heterostructures that we will present in section 6.2, cannot be done analytically

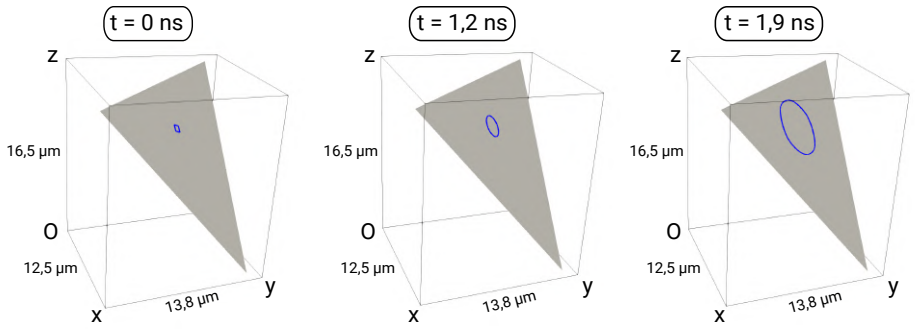

Figure 20: Dislocation Dynamics simulation showing the opening of a loop on a {111} plane under the influence of a biaxial stress field.

and again requires the numerical evaluation of the stress field by a FE solver. The next section will present the approach followed in this Thesis to couple the DD approach here described to an external FE code.

3.1.1 Discrete Continous Model

In this section we will present a methodology developed to couple the DD code described above to an external FE solver. In this Thesis this was implemented in the open-source FE framework, FEniCs [12, 13], following the approach called Discrete Continuous Model (DCM) presented in Ref. [15]. In this description, the problem of mechanical equilibrium is set in terms of a partial differential equation linking the unknown displacement field $\mathbf{u}$, to a generic applied deformation ε^*, called *eigenstrain* and introduced in section 1.2.2, through the relation:

$$\begin{cases} -\nabla\boldsymbol{\sigma}(\mathbf{u}) = 0 & \text{on } \Omega \setminus \partial\Omega \\ \boldsymbol{\sigma}(\mathbf{u}) = C(\boldsymbol{\varepsilon} - \boldsymbol{\varepsilon}^*) & \text{on } \Omega \setminus \partial\Omega \\ \mathbf{u} = 0 & \text{on } \Omega_D \\ \boldsymbol{\sigma} \cdot \mathbf{n} = 0 & \text{on } \Omega_N \end{cases} \tag{40}$$

where Ω is the integration volume and $\partial\Omega$ its external boundary.The bottom boundary $\partial\Omega_d$ is kept fixed by applying Dirichlet boundary conditions (zero displacement), while $\partial\Omega_n$ is the top free surface with Neumann boundary conditions (zero normal stress). On the lateral boundaries periodic boundary conditions are applied.

The PD problem defined in Eq. (40) is generally formulated in order to describe the response of a system to an applied deformation ε^*. This generalization can be easily used to describe the plastic deformation induced by a dislocation exploiting a modified version of the eigenstrain formalism, originally formulated by Elsheby to describe inclusions in solids [68] and discussed by Mura in Ref. [28]. This was done by following the DCM approach. Here the elementary plastic deformation $d\varepsilon_p$ produced by the motion of dis-

location segment is regularized by a distribution function $\tilde{w}$ as introduced by Wei Cai and coworkers in Ref. [69]:

$$d\varepsilon_p = \tilde{w}(h)\frac{\mathbf{b}\otimes d\boldsymbol{A} + d\boldsymbol{A}\otimes\mathbf{b}}{2} \tag{41}$$

where $d\boldsymbol{A}$ is the (oriented) area swept by the dislocation segment during its motion and h is a characteristic thickness for the regularization function $\tilde{w}$. By integration of the $d\varepsilon_p$ term over all the swept area dA and by summing this contributions for all the moving dislocation segments at a given time-step t of the simulation we obtain the applied plastic deformation for the whole dislocation microstructure, ε_p. The procedure described above is schematized in Fig. 21.

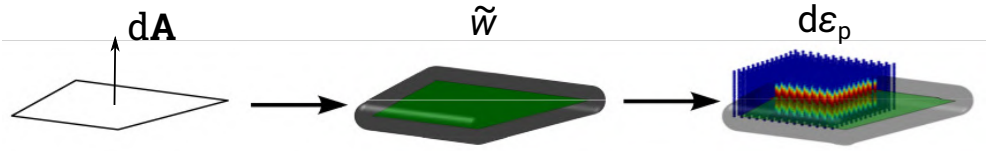

Figure 21: Regularization procedure for the DCM approach. The movement of each dislocation segment in the DD code produces an elementary swept area $d\boldsymbol{A}$ that is traduced in a regularized plastic eigenstrain by means of Eq. (41) and finally passed to the FEM code to compute the resulting stress field. Image adapted from Ref. [15]

3.1.2 Weak formulation for mechanical equilibrium

Explicitating the mechanical equilibrium equation (40) in terms of the displacement field $\mathbf{u}$ by means of equations (6) and (4) we obtain:

$$-\nabla\cdot[\mu_L(\nabla\mathbf{u}+\nabla\mathbf{u}^T)+\lambda_L(\nabla\cdot\mathbf{u})\mathbf{I}] = 0 \tag{42}$$

with μ_L and λ_L the Lamé constant for the material under consideration. In order to apply the FEM to approximate the solution $\mathbf{u}\in V$ we shall express it in the weak formulation by multiplicating Eq. 42 by a test function $\boldsymbol{v}\in V$ that satisfies the same boundary conditions of $\mathbf{u}$, and then by integration over Ω. V is generally defined as an Hilbert space and is called *function space* in the context of the Finite Element Method. Within this approach we can explicitate the *weak formulation* for Eq. 40. This can be expressed as the problem of finding a function $\mathbf{u}$ such that:

$$\int_\Omega \frac{\mu_L}{2}(\nabla u+\nabla u^T)\cdot(\nabla\boldsymbol{v}+\nabla v^T)+\int_\Omega \lambda_L(\nabla\cdot\mathbf{u})(\nabla\cdot\boldsymbol{v}) = 0, \qquad \forall v\in V \tag{43}$$

This equation can now be reduced to a finite dimensional subspace $V_n\subset V$ of dimension n

$$\int_\Omega \frac{\mu_L}{2}(\nabla\mathbf{u}_n+\nabla\mathbf{u}_n^T)\cdot(\nabla\boldsymbol{v}_n+\nabla\boldsymbol{v}_n{}^T)+\int_\Omega \lambda_L(\nabla\cdot\mathbf{u}_n)(\nabla\cdot\boldsymbol{v}_n) = 0, \qquad \forall\boldsymbol{v}_n\in V_n \tag{44}$$

The finite function space V_n will be taken as the space of Lagrange piecewise polynomials of order 1, defined at the nodes of the FE mesh. The corresponding basis set is indicated by ψ_k, $k = 1, \dots, N$. Now the unknown solution can be expanded on this basis set, $u_n = \sum_{k=1}^{N} u_k \psi_k$, and the test functions can be chosen as the basis functions $v_k = \psi_k$. Thus, for the orthogonality of the dot product between basis functions, Eq. (44) can be reduced to n indipendent equations:

$$\sum_k u_k \int_\Omega \frac{\mu_L}{2} (\nabla\psi_k + \nabla\psi_k^T) \cdot (\nabla\psi_j + \nabla\psi_j{}^T) + \int_\Omega \lambda_L (\nabla \cdot \psi_k)(\nabla \cdot \psi_j) = 0, \quad \text{for } j = 1, \dots, N \tag{45}$$

This set of equations can be now rewritten as a linear problem of the form

$$A \cdot \mathbf{u} = L \tag{46}$$

with $\mathbf{u} = (u_1, \dots, u_n)$, the unknown of the problem. A is usually called the *stiffnes matrix* and once the discretization is defined by means of a meshing algorithm it only depends on the material constants. L is a vector defining the imposed loadings and in our description depends on the eigenstrain ε^*. Thus, it should be updated at each time step of the simulation whenever the configuration of dislocation changes.

The solution of the linear problem defined in Eq. (46) will provide the unknown displacement field $\mathbf{u}$. Once this problem is solved, the stress field can be evaluated back from equations (4) and (6) and plugged into Eq. (38) in order to find the displacements of the dislocation segments at the next time-step of the simulation. By iterating this procedure a simulation of the evolution of the dislocation configuration is possible.

3.2 SURFACE DIFFUSION

The model implemented in this Thesis for the surface diffusion relies on an explicit description of the film profile. The film free surface is traced by a function $h = h(\mathbf{x})$ with $\mathbf{x} = (x, y)$ for a 2+1D description and $\mathbf{x} = (x)$ for a 1+1D description as the one schematically illustrated in Fig. 22. The equation determining the evolution of the profile h is the diffusion equation introduced in section 1.3. For a 1+1D description the diffusion equation takes the form:

$$\frac{\partial h}{\partial t} = \Phi + M \frac{\partial}{\partial x} \left[\frac{1}{\sqrt{1 + h'^2}} \frac{\partial \mu}{\partial x} \right] \tag{47}$$

where prime means differentiation with respect to $\mathbf{x}$. M is the mobility coefficient, setting the time scale for the evolution. Deposition can be included by assuming a vertical material flux Φ, mimicking typical Molecular Beam Epitaxy conditions. Once defined μ, the evolution is determined by integrating in time Eq. (47). At each time-step t, the profile evolution is defined by the solution of Eq. (47), tracing the motion of each point of the profile.

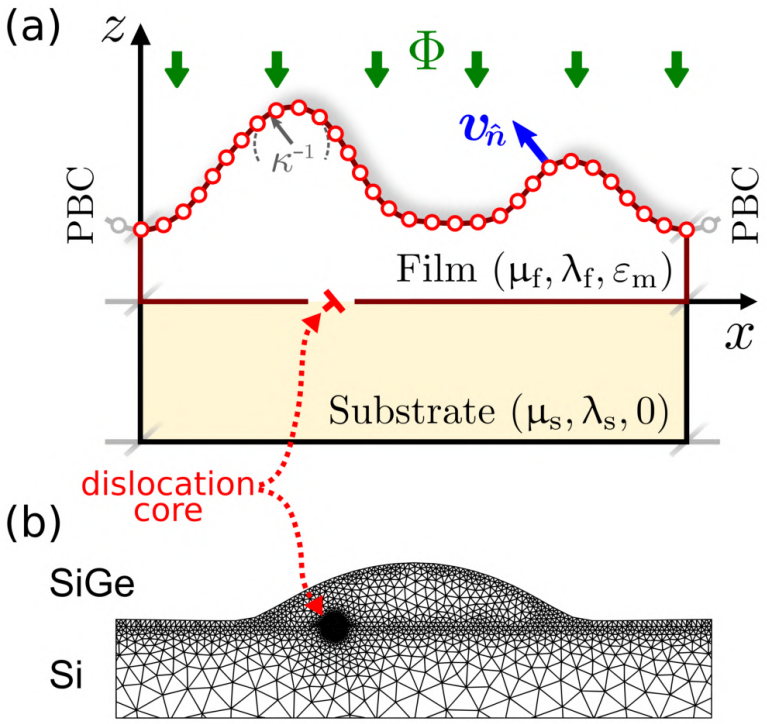

Figure 22: (a) Definition of the surface profile. (b) Example of locally refined mesh used in the simulations when describing the presence of dislocations. The region near defect cores is finely refined in order to better describe the high variation in the stress/strain field close to dislocations.

The chemical potential μ comprises three major contributions: surface, wetting and elastic energy. It takes the form:

$$\mu = \kappa\gamma + \frac{1}{\sqrt{1+z'^2}}\frac{dW}{dh} + \rho_\varepsilon \tag{48}$$

The first term accounts for the cost of exposing free surfaces and, for isotropic surface energy density γ, it is proportional to the local profile curvature κ. The second term accounts for film/substrate wetting [47, 46], as discussed in section 1.4.1. The last contribution in eq. (48) corresponds to the elastic energy density ρ_ε at the surface, calculated in the assumption of mechanical equilibrium. This is performed by solving the PD problem of Eq. (40) at each time-step on the entire simulation volume Ω. The resulting elastic energy density can be evaluated, once the stress and strain fields are known, starting from Eq. (7), and then plugged into Eq. (48) by restricting ρ_ε at the free surface. This procedure is shown for the 2+1D implementation of the model in Fig 23. The surface dynamics requires the modification of the surface profile during the simulation and this implies that the entire integration volume Ω follows the evolution. Thus, at each time-step the free-surface is updated together with the Neumann boundary conditions of Eq. (40).

Solving the mechanical equilibrium by means of the PD problem of Eq. 40 permits also to take into account inelastic effects by means of the eigenstrain term ε^* as already described in section 3.1. This allows for the description

of a heteroepitaxial misfit strain but also for the description of dislocation in our diffusion model.

In principle, in order to take into account the presence of dislocations ε^* should be defined as in Eq. (41). However, another possibility consists in following the approach discussed in Refs. [70, 71], setting the eigenstrain as the initial approximated solution provided by the analytic functions of the strain field produced by dislocations. The appealing aspect of this approach is that convenient local mesh refinement can be defined only for regions close to dislocation positions. These are indeed the regions where a higher precision is required, in order to correctly describe the highly non-uniform stress field close to dislocation cores. An example of a meshing procedure showing this approach is reported in the bottom part of Fig. 22.

In this work, whenever considering the stress field of a dislocation in a simulation cell with periodic boundary conditions (PBCs), we exploited the analytic function reported in Appendix A. Furthermore, the stress field in the proximity of the dislocation core is regularized by exploiting the convenient procedure suggested in Ref. [69]. Again, analytic expressions for the regularized stress field of arrays of dislocations are reported in Appendix A. In this model these expressions are exploited in order to avoid numerical divergence during the integration of the elastic energy.

The previously described model is implemented in the same FEniCS environment described in section 3.1. This is a tool that provide an interface to solve PDEs. The coupled problem of elasticity and surface diffusion is setted by projecting the free surface of a 3D cell on a plane that is the support for the 2D finite element space needed to solve the diffusion equation. The parallel capabilities of the code exploits a spatial discretization by decomposing the domain into separate regions as can be seen in Fig. 23. The assembly of the matrix element defining the FEM model, Eq. (46), can thus be performed in parallel. The required communications for evaluating mesh elements shared by two adjacent volumetric regions made possible by openMPI calls between the parallel processes.

3.2.1 Weak formulation for surface diffusion

The weak formulation of the diffusion equation is analogous to the derivation described in section 3.1.2 for the mechanical equilibrium equation. However, Eq. (47) implies fourth-order spatial derivatives and cannot be solved by means of first order Lagrange polynomials. Eq. (47) is thus re-written as two coupled second order equation defined on a mixed finite element space $V_n \times V_n$ where V_n is a standard Lagrange finite element space of dimension n. The two PDEs that we need to solve can thus be written as:

$$\frac{\partial h}{\partial t} - \nabla M \nabla \mu = 0 \tag{49}$$

$$\mu - \frac{\partial W}{\partial h} - \rho_\varepsilon = 0 \tag{50}$$

The resulting derivation for the weak form of these equation follows the approach described in section 3.1.2.

The time integration of Eq. (47) is performed by means of a semi-implict approach. The timescale of the simulations reported in this work are al-

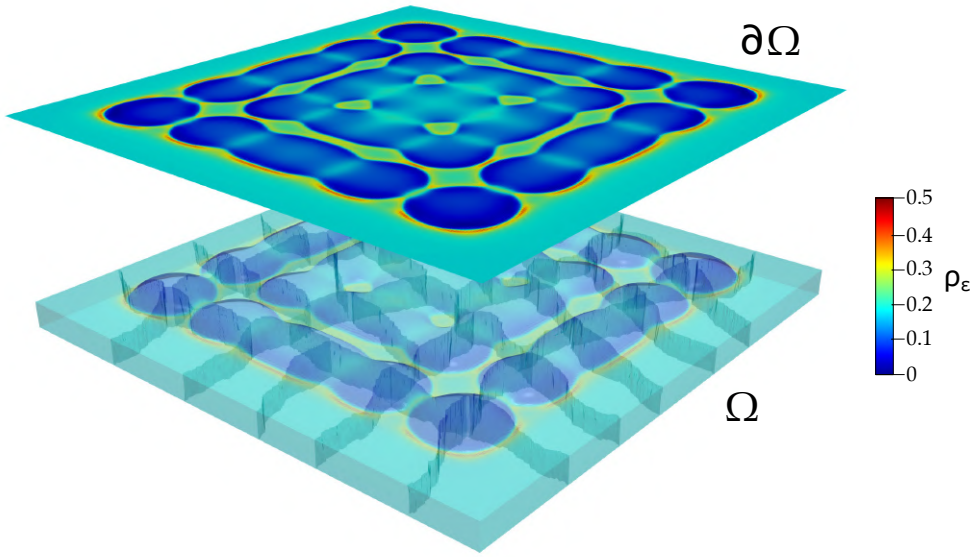

Figure 23: Considered system, Ω is the full 3D volume under consideration, while the top plot $\partial\Omega$ defines the 2D mesh used for solving the diffusion equation.

ways left in arbitrary units unless indicated. However, the mobility coefficient M can, in principle, be estimated from the diffusion coefficient $M = h_l V_a D_0 (kT)^{-1} \exp[E_b/(kT)]$, with h_l the thickness of a monolayer, V_a the volume per atom, D_0 the material diffusion coefficient, E_b the energy barrier for site hopping, k_b the Boltzmann constant, and T the temperature. Typical values for the Ge/Si system can be set as $h_l = 0.146$ nm, $V_a = 0.02$ nm^3, $D_0 = 8.5 \times 10^8$ nm^2/s [72], $E_b = 1.1$ eV [73].

4 FROM ELASTIC TO PLASTIC RELAXATION

As described in the Introduction, there exist two qualitatively different paths leading to strain relief in heteroepitaxial systems. The first possibility is the elastic relaxation by deformation of the flat geometry of the growing film into three-dimensional islands, partially relaxing the in-plane strain thanks to the exposure of lateral free surfaces. This is the path followed by systems displaying the Stranski-Krastanow (SK) growth mode, after the completion of a wetting layer (WL), as the Ge/Si system considered in this Thesis. Alternatively, the stress load can be released by misfit-dislocation injections. However, these two qualitatively different relaxation paths are competing together in the overall relaxation of the heteroepitaxial film and thus a model able to tackle both this effect simultaneuosly is required in order to describe some of the peculiar effects widely investigated in the literature.

In this chapter are presented some applications of the model for surface diffusion introduced in section 3.2. First, we will study the elastic relaxation of a strained film. We will present some simulations of the formation and coarsening of heteroepitaxial islands for a SiGe/Si system following the Stranski-Krastanow growth regime. This was done by implementing in the surface diffusion model the wetting potential introduced in section 1.4.1, fitted on ab-initio simulations for Ge/Si systems. Furthermore, by exploiting the wetting potential discussed in section 1.4.2 we were able to model the behavior of thin films exhibiting a finite contact angle with their substrate whithin the very same model. A brief collection of simulation results about this topic is reported in section 4.2.

Finally, in section 4.3 and 4.4 we will analyze more in details the behavior of SiGe/Si systems, by accounting also for the possibility of inserting misfit dislocations on the fly during the growth simulations. We will show that this permits to identify two different growth regimes, one reproducing the well known effects of cyclic growth for heteroepitaxial islands [62], the other leading to nearly-flat, plastically-relaxed thin films [56].

4.1 ELASTIC RELAXATION OF HETEROEPITAXIAL FILMS

As treated extensively in Section 1.3 the competing effects of surface and elastic energy minimization, with the former leading to a flattening of the surface, while the latter favoring the formation of islands to release the elastic energy of the film, results in unstable solutions of the diffusion equation (17). This lead to the growth of a perturbation with typical time-scale and dimension dependent on the misfit strain between the film and the substrate. The typical example of this is the growth of high concentration SiGe films on Si(001) substrates. As reported in Fig. 24 for the deposition of a pure

germanium film on Si(001), the elastic relaxation results in the formation of three dimensional islands.

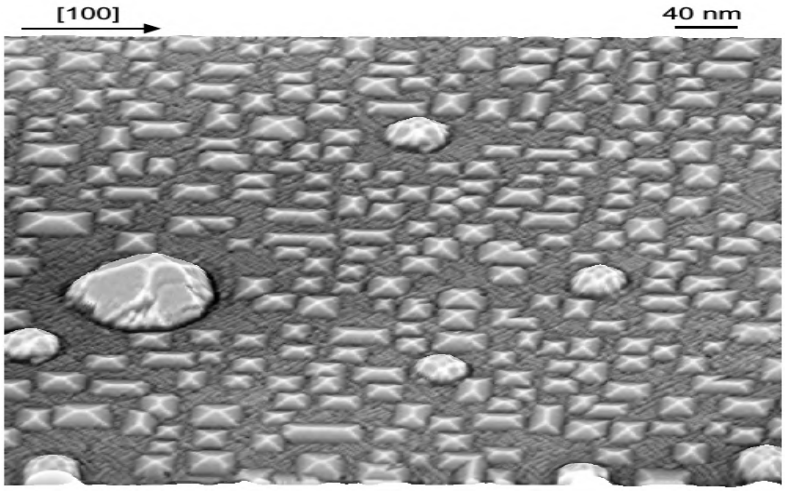

Figure 24: STM image showing germanium germanium islands grown on Si(001). Image adapted from Ref. [74].

The initial stages of the islands growth can be modeled by the Asaro-Tiller-Grinfeld (ATG) instability [30, 31, 38], described in section 1.3. The ATG model considers the evolution process of a semi-infinite Ge film, under the influence of a biaxial stress, in a linear approximation. This description can be used to explain the growth of islands in a continuum model where an initial perturbation of the profile whose wavelength is above the critical wavelength defined in equation (19) can be amplified by this mechanism. The model developed in this Thesis, thanks to the FEM solver described in section 3.2, takes into considerations both linear and non-linear contributions for the elastic energy, therefore it is also able to simulate evolution stages that go beyond the initial linear ATG approximation. This is well illustrated in figure 25 where the amplification of an initial cosine perturbation of $\lambda = 15\,\mathrm{nm}$ and initial amplitude of $0.01\,\mathrm{nm}$ representing the free-surface of a thick Ge layer on a Si substrate is shown. The initial stages show the behavior predicted by the linear ATG model, with the amplification of the initial cosine perturbation. As soon as the linear approximation of the ATG model ends, a deviation from this simple amplifications can be seen. Indeed, later stages show a modification from the cosine shape. This happens when the top tends to be more relaxed, so the surface energy cost tends to round it [75]. On the contrary, the trenches between islands are more elastically-stressed and so tend to form higher curvature regions. The evolution thus tends to increase these cusp singularities until the divergence of the profile. Although this cycloid shape can be actually observed in experiments [76, 77] as reported in Fig. 26, this behavior of the model will lead unavoidably to a divergence, that does not permit the description of later stages of the evolution. Furthermore, this description explains the growth of heteroepitaxial islands as the amplification of an initial perturbation and so does not account for a complete description of nucleation process of islands, particularly important in the case of high Ge content [78].

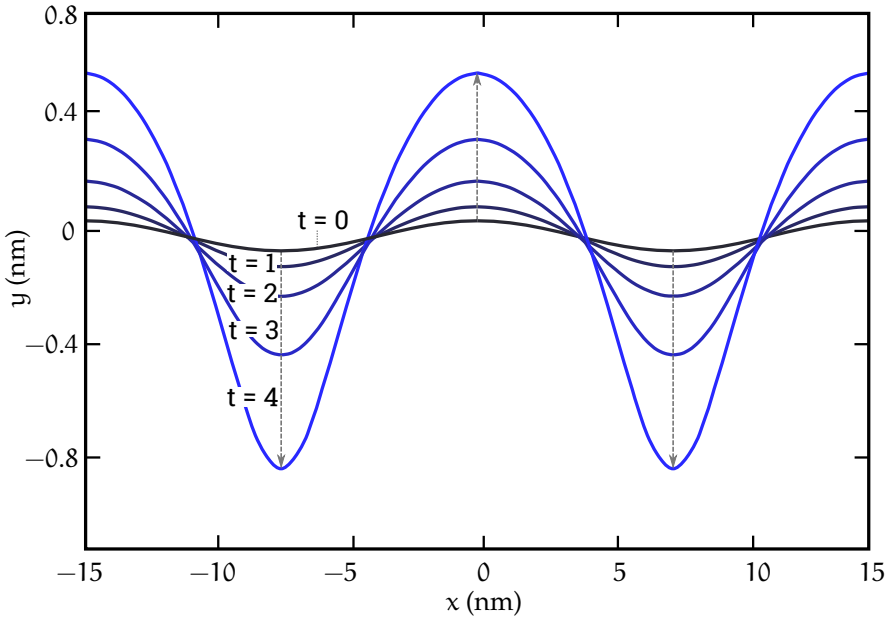

Figure 25: Evolution of a cosine perturbation following the law of surface diffusion. Here are shown stages that go beyond the ATG linear stability analysis, thanks to the exact solution implemented for the elastic field. Time is in arbitrary units.

4.1.1 Long time process: Coarsening of Islands

A more realistic approach to model the growth process requires to start from a few-monolayers thick thin film and to account for the modification of the surface energy that affects this wetting-layer compared to the rest of the film. This leads to a growth mode similar to the Stranski-Krastanov regime, with a finite wetting layer that separates the surface islands from the substrate. In a Ge/Si system, it is known that Si has an higher surface energy density than Ge: this property causes the formation of the Ge wetting layer, which covers all the Si surface, lowering the surface energy of the system. The surface energy density function used to reproduce this behavior is the γ of Eq. (20). This function, as discussed in section 1.4.1, is an exponential function of the distance from the film/substrate interface.

The best way to carry out a simulation limiting the influence of the initial profile is to use a random perturbation. The idea of the random method is to include all the possible wavelengths, but using a very small amplitude. Therefore, depending on the elastic energy in the film, and thus on the amount of misfit strain, one mode, corresponding to the λ_{max} derived in the linear ATG theory, grows faster than all the others dominating the resulting island profile.

Figure 27 shows a two-dimensional simulation of the evolution of a random perturbation on a $Si_{0.2}Ge_{0.8}$ thin layer. The simulation starts with a thin film of a few mono-layers (1 nm) and a deposition flux is included in order to simulate a growth process. The relaxation of the film into islands can begin only when the film has reached a certain critical thickness [79]. This

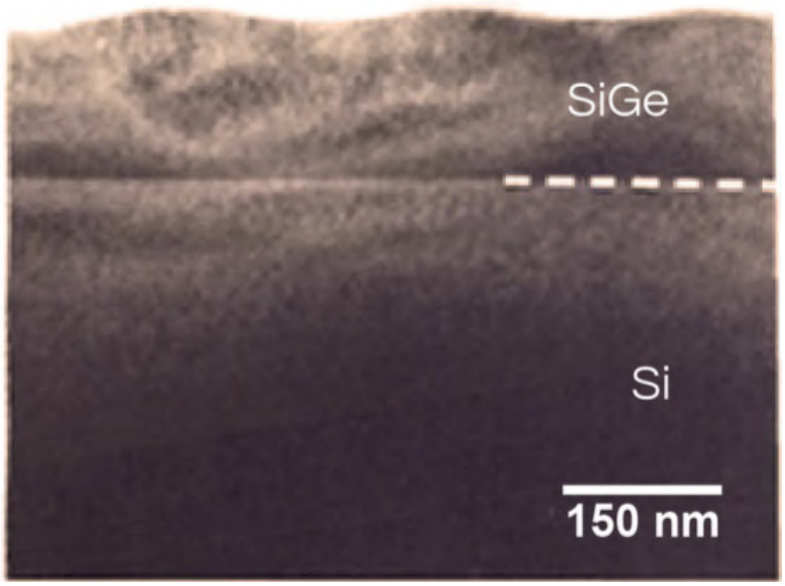

Figure 26: TEM cross-section image showing the development of the ATG instability in a SiGe/Si heteroepitaxial systems. Image adapted from Ref. [76]

behavior depends also on the deposition flux, as a strong rate has the effect of shifting this thickness producing thick out of equilibrium film before elastic relaxation can begin. Instead, a lower flux compared to the diffusion timescale, let the system free to relax elastically while only adds new material. This is an example of a near-equilibrium growth process. The first stages of this simulation show the growth of perturbation with locally random wavelengths, but instead of continuing the growth up to reach the wetting layer, smaller islands prefers to coalesce with larger ones, in order to adjust the local wavelengths to more favored ones as explained by the ATG model. After the deposition of a sufficient amount of material the flux stops and the system is let evolve by annealing. At this point, at variance from the standard ATG model description, all the islands have reached the substrate and they start exchanging material. This is a long time process known as *coarsening*. It is due to little differences in islands size that favor the transfer of material between a slightly less relaxed islands to one more relaxed. The result of this process is that smaller islands disappear and larger ones tend to grow in dimensions attracting more material. At the last stage represented only a small number of the initial islands remains, those randomly more relaxed with respect to the other and so favorable in terms of attraction of material. Further coarsening process among them requires much longer time-scale and the limiting result is the surviving of only one large volume islands [46, 80, 81, 82].

The same kind of behavior can be appreciate in Figure 28 where the same simulation is reproduced in three dimension by exploiting the approach described in Section 3.2. Here again we see a thin layer of a few monolayers of Ge deposited on a silicon substrate. The simulation cell is 500×500 nm of lateral sizes and 50 nm in the vertical direction. During the simulation the surface of the deposited films starts to deform from the planar geometry

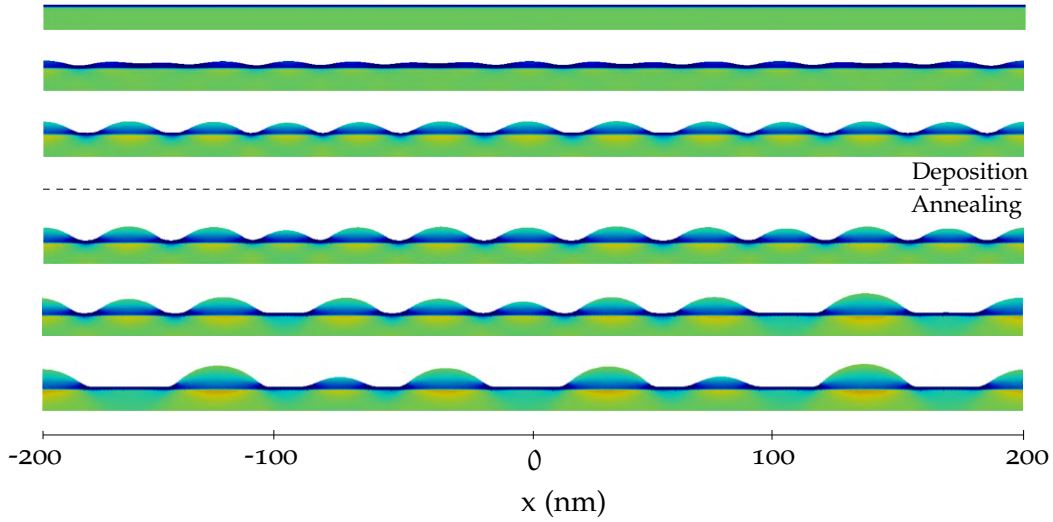

Figure 27: Representative stages of a growth simulation illustrating long-time coarsening process of islands. In the first three stages a deposition flux is imposed to simulate a growth, in the last three the system evolves by annealing. Color map refers to the in-plane component ε_{xx} of the strain field.

and elastically relax by the formation of islands. In the later stage of the simulation the differences in relaxation between islands leads to coarsening phenomena where the bigger ones tend to attract material from the smaller neighbour due to the fact that they are elastically more relaxed.

The resulting organization and shape uniformity of these randomly nucleated island is however very poor. This limit the applicability of these simple form of self-organization since in most of applications the key requirement is control over these parameters. Various possibility have been developed to address this drawback, such as pre-patterning the substrate via etch-pits in order to guide island formation [83], or exploiting stressors. Another recently proposed approach is the exploitement of pre-patterned film patches. This allows a precise control over the self-assembled process and thus can be a viable path to overcame the limitations of self-assembled islands. In the next section we will present results showing how this process can be tuned for the dewetting of a strained film. This is done by applying the very same model exploited in this section but replacing the wetting potential with the one introduced in section 1.4.2.

4.2 SOLID-STATE DEWETTING OF STRAINED FILMS

As anticipated in the introduction of this chapter the model developed to study the elastic relaxation of heteroepitaxial systems proved to be general enough to be applied also to the description of the solid-state dewetting of thin strained films. In order to take into account the presence of a contact angle ϑ we replaced the wetting potential mimicking the SiGe/Si interface with the potential introduced in section 1.4.2. This section will show simulations performed with the code described in section 3.2 aimed at inspecting

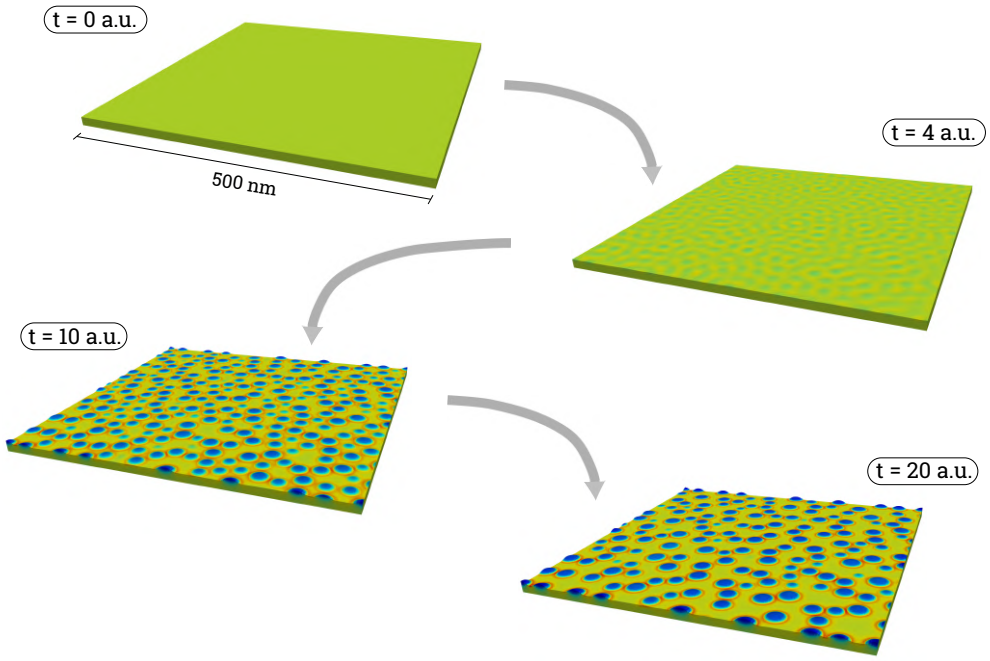

Figure 28: Representative stages of a 3D simulation of the elastic relaxation of a stressed film into islands. Starting from a few nanometer-thick wetting layer the system evolves under annealing and tends to deform the flat morphology into islands in order to elastically relieve the imposed misfit strain.

the competition between the phenomena of dewetting and ATG instability, however, the treatment reported here is not intended to be exhaustive of the topic and further details can be found in Refs. [84, 85, 86, 87].

The simulation presented here are performed in adimensional units for the time and space scale considered. Here the focus is on showing the general behavior of the competition between elastic relaxation of an imposed elastic energy density ρ_ε and the dewetting instability in thin solid films, without attempts to reproduce the parameters of a specific system.

As extensiveley treated in section 1.3 the ATG model predicts the mode of the fastest growing mode q in terms of the elastic energy density in the film. This defines a characteristic length λ_{ATG} that as can be seen in Eq. (19) is inversely proportional to the elastic energy density ρ_{el}. The same is true for the so-called pinching instability. This is an instability that lead to the retraction of a film edge via mass transport at its surface, eventually leading to the exposition of the substrate and the formation of a solid "droplet" or island separated from the retracting film. In Ref. [14] the authors showed how the characteristic length of the pinching instability can be realated to forth inverse power of the contact angle ϑ. Thus, it is possible for a strained film exhibiting a contact angle with its substrate to find a set of parameters for which the characteristic length (and time) of ATG and pinching instabilities are close enough to see the co-existence of these two phenomena.

An example of a 2D simulation showing this effect is reported in Fig. 29. This is a simulation of a thin film of thickness $h = 8$ and with parameters for the wetting potential $h^* = 6$ and $\vartheta = 10$. The elastic energy density is set to $\rho = 0.2$, and a small random perturbation (of average amplitude

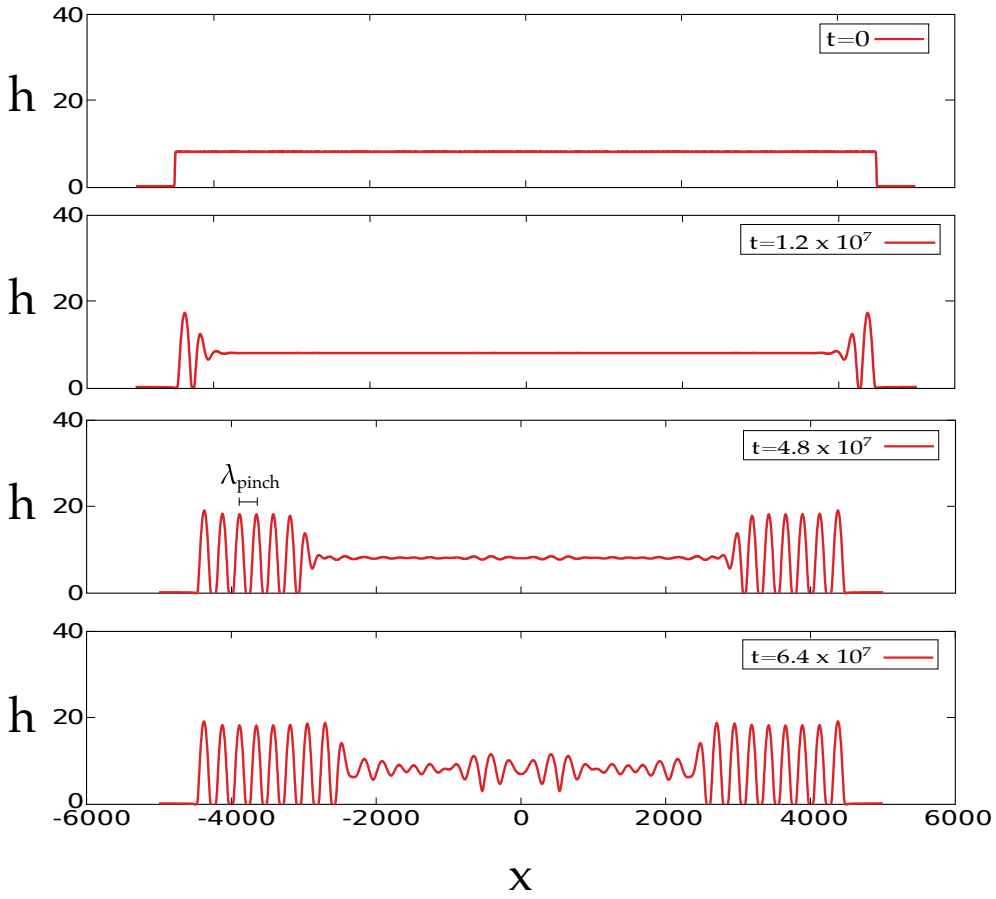

Figure 29: Simulation competition between the dewetting and ATG instabilities. The mass shredding starts at the edges of the thin layer by producing islands with a characteristic size λ_{pinch}. In later stages of the simulation the ATG instability starts also to develop arund the center of the thin layer.

10^{-5} is added to film profile as trigger for the ATG instability. As can be seen in the figure, the mass shredding starts at the edges of the thin layer and islands are produced by the pinching of the retracting film. In later stages the ATG instability starts also to develop around the center of the simulation cell. A detailed analysis of the results of these simulations for different combinations of the (ρ, ϑ) parameters showing can be found in Ref. [84].

Finally, the competition between the elastic relaxation of the misfit strain in the layer and the pinching instability can be appreciated by the three-dimensional simulations as reported in Fig. 30. Here the starting condition of the simulations are square patches of a thin film deposited on a substate. The thickness of the film is set at $h = 4$ and the characteristic length for the dewetting potential is $h^* = 3$. The contact angle parameter ϑ is set to 45° and the lateral sizes of the square patches are choosen to be integer multiples of the characteristic length λ_{pinch}. This means that for each pair of parameters (ρ, ϑ) simulations similar to the one reported in Fig. 29 were performed in order to find the corresponding λ_{pinch}. This was then used as parameter for the 3D simulations. In Fig. 30 are reported the results for the largest considered simulation cell, corresponding to a lateral patch size of $4\lambda_{pinch}$.

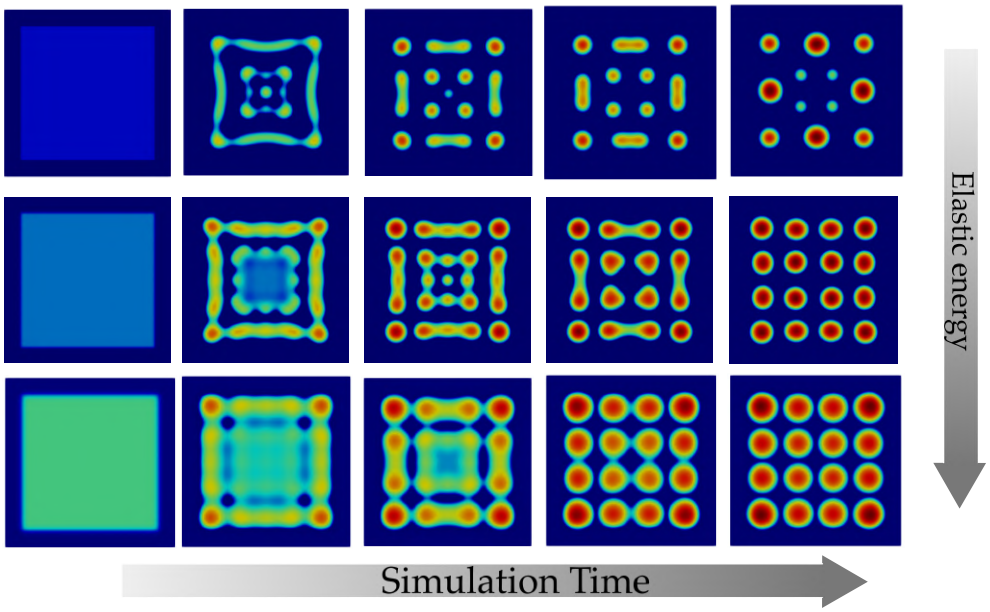

Figure 30: 3D simulations showing the evolution under the combined effects of elastic ATG instability and dewetting intability. The starting condition are square patches of a thin film deposited with lateral size corresponding to 4λ. The top row correspond to simulation performed with $\rho_\varepsilon = 0$, the center row with $\rho_\varepsilon = 0.2$ and the bottom $\rho_\varepsilon = 0.4$.

As can be seen from the figure the effects of increasing the elastic energy is to force a lateral and size. However these results are still preliminar and should be further investigated.

4.3 CYCLIC GROWTH

Experimental evidence by LeGoues et al. [88], dating more than 20 years ago, has shown the peculiarity of heteroepitaxial-growth dynamics under the simultaneous effect of elastic and plastic relaxation. By in-situ electron microscopy, the authors showed oscillations in island shapes, attributed to successive insertion of misfit dislocations in SK Ge islands on Si(001). Beside the dramatic evidence of such cyclic growth supplied in Refs. [88], the influence of dislocations on SK islands has been inferred by simple height-to-base aspect ratio (AR) vs. volume (V) plots. As highlighted in several papers [52, 53, 89], the onset of plasticity is signaled by a transition, beyond a critical volume, from a monotonous AR increase vs. V, to a less well-defined (due to fluctuations) behavior, almost a plateau.

In this Section we will further develop the simulations reported in section 4.1 by modeling the plastic relaxation of partially relaxed SiGe islands. For this, a suitable approach to determine the conditions for the insertion of a dislocation on the fly during a growth simulation was developed. Insertion of a defect within an island lowers the need for strain relaxation, so that a flatter configuration becomes energetically favorable. Static calculations investigating the onset of plasticity and the shape of dislocated islands have been reported in several papers [88, 89, 90].

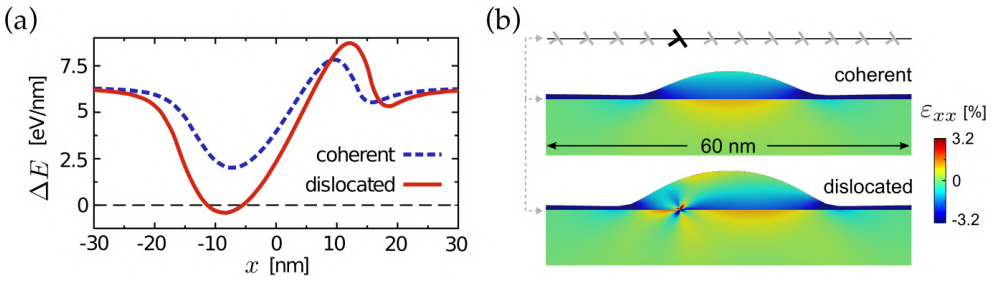

Figure 31: During the evolution of the film profile, lateral scans are made to check whether the presence of a further dislocation lowers the energy of the system ($\Delta E < 0$). (a) Energy difference between the system with and without dislocation for a small (dashed curve) and a large island (continuous line). (b) Morphology of the two islands and corresponding ε_{xx} strain map, including the effect of the dislocation for the larger one.

All simulations here reported were run by setting parameters for the same parameters as those of section 4.1, A $Ge_{0.8}Si_{0.2}$ is grown on a Si(001) substrate, considering an exponential wetting potential. The ratio M/Φ of Eq. (17) was set equal to 10^4 when considering close-to-equilibrium conditions and decreased to 10^2 for simulations far-from-equilibrium of section 4.4.

The introduction of dislocation in these simulations follows the approach-proposed in Refs. [70, 71] and discussed in chapter 3, setting the eigenstrain as the initial approximated solution provided by the analytic functions available for arrays of dislocations [54], as required by PBCs. A dipole construction is also exploited to suppress spurious lateral interactions resulting from the long-range (r^{-1}) dependence of the dislocation strain field. Furthermore, the stress field in the proximity of the dislocation core is regularized by exploiting the convenient procedure suggested in Ref. [69], in order to avoid numerical divergence (this is especially needed in order to integrate the elastic energy).

The introduction of dislocations into the system is performed on the fly during the growth simulation. In particular, the variation in the total elastic energy is probed by placing the dislocation at different sites along the film/substrate interface. In case a position leading to energy lowering is found, the dislocation is placed there and the corresponding stress field (see Ref. [70]) is added to the purely elastic one. The procedure is illustrated in Fig. 31. It is worth noting that this energetic criterion totally neglects the process of nucleation of dislocations discussed in section 2.5, and the associated activation energies. This approximation typically leads to an underestimation of the critical thickness for the growth of flat epilayers, as reported in several experimental observations [91]. However, when dealing with the plastic relaxation of islands, it has been shown that a purely purely thermodynamic criterion fits the experimental critical sizes with considerable agreements [90, 70]. This is likely due to the highly inhomogeneous distribution of the stress field in the island, exceeding some GPa close to the island edges, thus favoring the process of dislocation injection, as soon as the thermodynamic limit has been overcome [91].

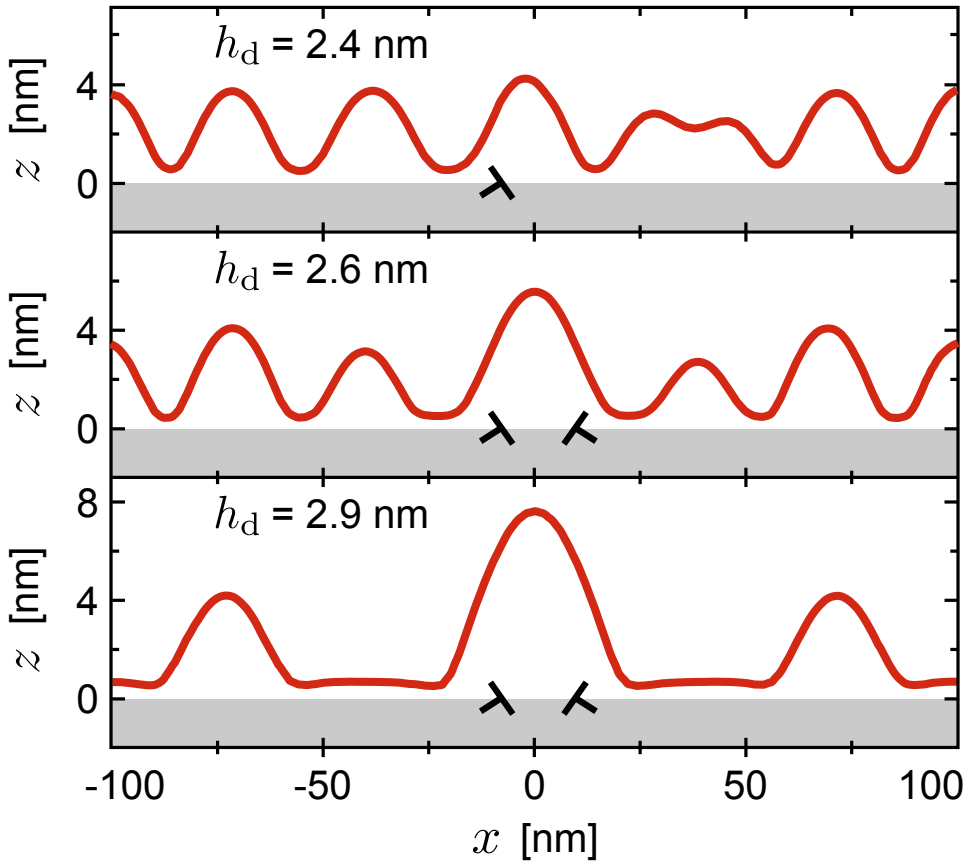

Figure 32: Temporal evolution of the film profile for different amounts of material deposition h_d (directly proportional to time), corresponding to the injection of the first (h_d=2.4 nm) and second (h_d=2.6 nm) dislocation and to a later stage (h_d=2.9 nm) where the island hosting the dislocations has quickly grown while the two adjacent coherent islands disappear.

Simulation results corresponding to quasi-equilibrium growth are displayed in Fig. 32. Film profiles at different times are shown, starting from the stage where our automatic procedure first leads to insertion of a dislocation. Previous stages, including WL formation, onset of the Asaro-Tiller-Grinfeld (ATG) instability, are as reported in section 4.1, and the long time coarsening process in the absence of defects has already been widely discussed in the literature (see e.g. Ref. [46]). Following Ref. [90], we considered only 60° dislocations, whose lowest-energy position is laterally displaced with respect to the island center [90]. As a result only one side of the island strongly benefits from plastic relaxation. Thus, a second defect is quickly added to the other side. Then, the system evolves for significant time without introducing further dislocations. As the chemical potential of the defected island is much lower with respect to the one of the coherent islands, coarsening is observed, the dislocated island enlarging at the expenses of the two lateral ones which disappear. The presence of large plastically relaxed islands surrounded by a depletion zone was clearly reported in several experiments (see, e.g., Fig. 1 of Ref. [53]).

Let us now follow the long-time evolution of a single dislocated island surrounded by a flat substrate. As more material is deposited, the island keeps

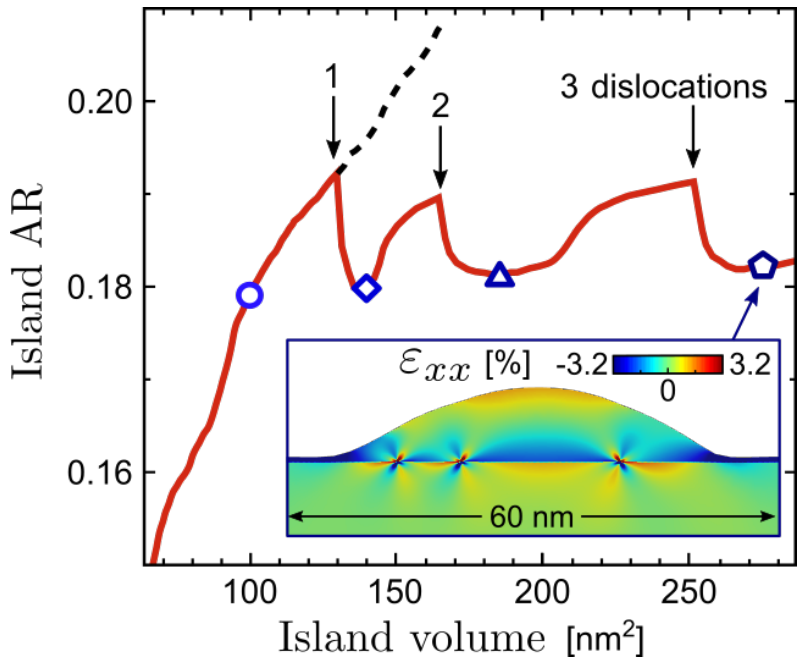

Figure 33: Evolution of the island AR as a function of the deposited material. A sharp change in behavior is seen when the first dislocation is introduced. From this stage the evolution substantially deviates from the corresponding one obtained by suppressing the injection of defects (dashed curve). Inset: Strain map (ε_{xx} component) at the latest stage of evolution.

on growing and dislocations are added each time a critical-volume condition is met. The full development of the island is conveniently followed by the heigth-to-base Aspect Ratio (AR) vs. V curve reported in Fig. 33. Until the island is coherent, the AR grows with V, as expected from simple static models [70]. When the first dislocation is introduced the behavior changes. A sudden drop in the AR is observed: the effective lattice mismatch in the island is lowered, and flattening occurs to reduce the exposed surface. As the volume increases, however, the tendency towards increasing the AR to better release the strain dominates again, until a new dislocation is introduced. Our simulation predicts an oscillatory behavior of the AR and, thus, cyclic growth. This sudden change in behavior in the AR vs. V curve has been reported in several experiments [52, 53, 89]. Actual oscillations are compatible with the observations, despite not being evident in curves derived from experiments due to the scatter among measures on several islands. The in-situ observations by LeGoues et al. [88], however, leave little doubts on the presence of shape oscillations. Notice that islands profiles in the presence of an odd number of dislocations are typically non-symmetric (panel b), as a direct consequence of the strain field (inset in panel a). The lack of lateral symmetry of some dislocated islands is quite evident in the experimental results of Ref. [53].

4.4 GROWTH OF PLANAR FILMS

Let us now show that the very same model also predicts the possibility to grow flat films by kinetically suppressing island formation. The evolution reported in Fig. 55 was obtained by decreasing the mobility by a factor 100 with respect to the previous case, thereby mimicking the low-temperature growth stage used in experiments to stimulate dislocation injection prior to island growth [92, 56].

The reduced mobility slows down the development of the ATG instability, so that the film grows almost flat until it reaches the critical thickness for dislocation injection (around ~1.2 nm with our parameters). When this occurs a first dislocation is introduced (an array of dislocations distanced by the cell size is actually introduced, due to PBCs). Others follow at larger thicknesses. No islands are formed. As evident from the strain maps of Fig. 55, in these simulations we have considered 90° and not 60° dislocations. This is because in flat Ge/Si(001) films 60° dislocations tend to combine in 90° Lomer pairs [93, 94]. Importantly, it is not the change in the defect character to cause the different behavior with respect to the close-to-equilibrium case: we directly verified (not shown) that the qualitative behavior is unchanged by replacing 60° (90°) dislocations with 90° (60°) dislocations in close-to-equilibrium (out-of-equilibrium) conditions.

Some undulations, as also reported in the low-T experiments of Ref. [93], are seen in Fig. 34(a), and can be appreciated by the plot in Fig. 34(b). They are indeed caused by the modulation in chemical potential induced by the presence of the dislocations. At variance with SK islands, such undulations are suppressed when the film is thick enough (leading to a uniform chemical potential at the free surface), and dislocations relax the misfit strain [95]. Under these conditions there is no further need of forming islands, and the kinetic constraints can be removed while growing a thicker flat film.

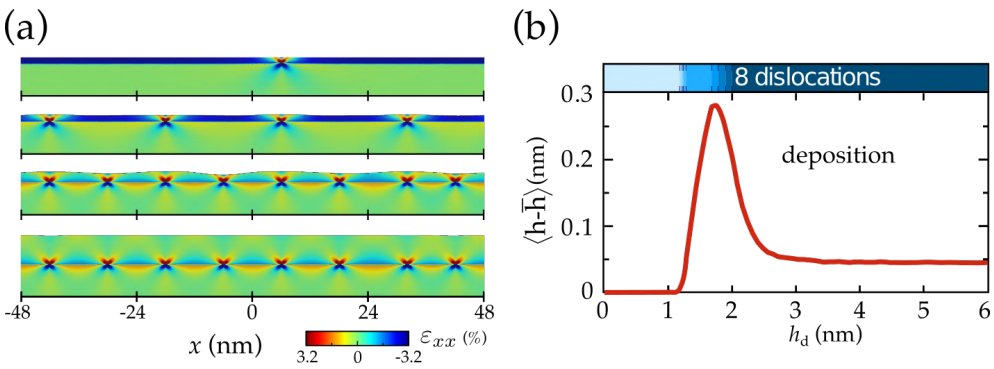

Figure 34: (a) Relevant simulation stages for the evolution observed during out-of-equilibrium growth. Undulations are caused by the underlying dislocations. When full plastic relaxation is achieved the film becomes flat again. (b) Temporal evolution of the film roughness evidencing the onset of undulations, slowing disappearing with thickness. Once dislocated, the film is stable against annealing as shown by the simulation continuation without deposition (dashed line on the right). The number of dislocations is reported in the top colored bar.

Finally, we notice that also dislocation-induced undulations can be suppressed by reducing the temperature further. In that extreme regime diffusion would be totally frozen and our model would predict conformal growth. However, the validity of the approach would be questionable as mono-atomic surface steps created by dislocations are not included in our model, while known to influence the film roughness in the absence of surface diffusion [96].

5 MISFIT DISLOCATIONS DISTRIBUTION IN HETEROEPITAXY

The growth of planar heteroepitaxial films and the surface roughness developed at their free surface, simulated at the end of the previous chapter, is a widely investigated topic *per se* due to the possible exploitment of these systems as substrates for technological application in the microelectronics industry. The growth of flat films is usually performed with heteroepitaxial systems exhibiting relatively small misfit strain $f \lessapprox 0.02$. Indeed, under these conditions the elastic relaxation is slow with respect to the growth rate (in the terms discussed in the previous chapter) and the film grows with a nearly flat-morphology until plastic relaxation sets in. At this point the formation of regular surface undulations at its free surface, known as *crosshatch pattern* (CHP), are commonly observed. References to this phenomenon can be found in literature for a wide variety of heteroepitaxial systems [97, 98, 99]. Indeed CHPs are typically recognized as a fingerprint of the plastic relaxation itself. However, despite its popularity, the fundamental parameters linking the CHP to the underlying network of misfit dislocation is still not entirely understood. This is due to several competing phenomena occurring at the same time and to the inability of too simple models in capturing the main features of the CHPs dynamics as we will show later in section 5.2.1.

In this chapter we will show that the CHP dynamics can be understood and reproduced on the theoretical ground once the underlying distribution of misfit dislocations is known. First in section 5.1 we will analyze in detail, by linking several experimental observations by means of a theoretical model, the network of misfit dislocations formed during the relaxation of a low-misfit $Si_{0.92}Ge_{0.08}$ film. This will permit us to generalize the functional form describing the position of MDs. Then, in section 5.2 we will exploit this result to develop realistic model able to reproduce the main features of CHPs evolution, providing direct comparison of the model predictions with dedicated experiments.

5.1 TILTING ANGLES MAPS

The characterization of the distribution of misfit dislocations inside an heteroepitaxial film represents a great challenge for the experimental techniques available nowadays. X-Ray diffraction (XRD) permits a precise evaluation of the lattice distortions and thus can be used to un-directly reconstruct the presence of misfit dislocations in a thin layer [100]. However, even the high-resolution micro-XRD obtained by high-energy synchrotron beam cannot be used to detect individual defects when the average separation of these becomes of a few tens of nanometers. On the contrary, TEM investigations are capable of detecting single misfit dislocations but presents two major drawbacks: they require a destructive processing, since the sample must be

thinned to a thin lamella before the analysis, and they cannot explore large area without a time-consuming procedure of image alignment, thus limiting the statistical power of these characterization. In this section we will show how these two analysis can be combined together by means of a theoretical model, finally providing an explanation of the spatially-resolved tilting angles maps obtained from micro-XRD analysis in terms of single-defects contributions.

5.1.1 Experimental characterization

The system under consideration in this Section is a 600 nm-thick $Si_{0.92}Ge_{0.08}$ film grown by SILTRONIC on a 300 mm Si(001) wafer using a high temperature (1050°C) CVD process. Details about the growth process can be found in Ref. [101].

The experimental characterization was performed at IHP where, by means of Focused Ion Beam (FIB) a 40×40 μm^2 area was marked into the layer to define a region for Scanning X-Ray Diffraction Microscopy (SXDM). The micro-XRD analysis showed an average Ge content of $x \approx 0.08$ and a 35% of strain relaxation. Both the limited thickness of the film, yielding only partial strain relaxation, and the low Ge content were chosen in order to avoid a too dense (and too complex) dislocation network which would have make the following analysis more complex. The results were also analyzed in order to produce the spatially-resolved tilting angle map reported in Fig. 35(a). In the figure we display the $\Omega(x,y) = \Omega_{xz}(x,y) + \Omega_{yz}(x,y)$ tilt-angle map over the marked 40×40 μm^2 film region. In tilt-angle maps, the contributions coming from dislocations running along mutually perpendicular directions can be easily separated [102], and the resulting map for only the $\Omega_{xz}(x,y)$ component produced only by the dislocations running along the y direction is reported in Fig. 35(b). The pattern is particularly simple, presenting a negligible dependence on the y coordinate. Indeed, due to the low misfit, the heterostructure here considered is expected to display long misfit segments [91], leading to the (quasi) one-dimensional tilt-angle distribution observed. Notice that threading arms, in any case rather unlikely to be present in the sampled area (we measured a threading dislocation density of the order of 10^5 cm^{-2}), would produce no detectable signal in the X-ray diffraction [103].

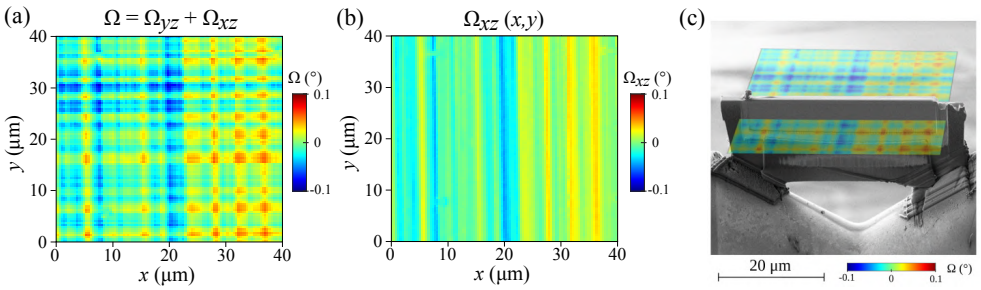

Figure 35: Tilt maps recorded by SXDM. Panel (a) Total tilt angle $\Omega = \Omega_{xz} + \Omega_{yz}$. Panel (b) Ω_{xz} tilt angle. (c) Schematic representation of the alignment between the 40 μ-long TEM lamella, imaged by SEM microscope, and the X-Ray map, obtained through FIB markings on the sample.

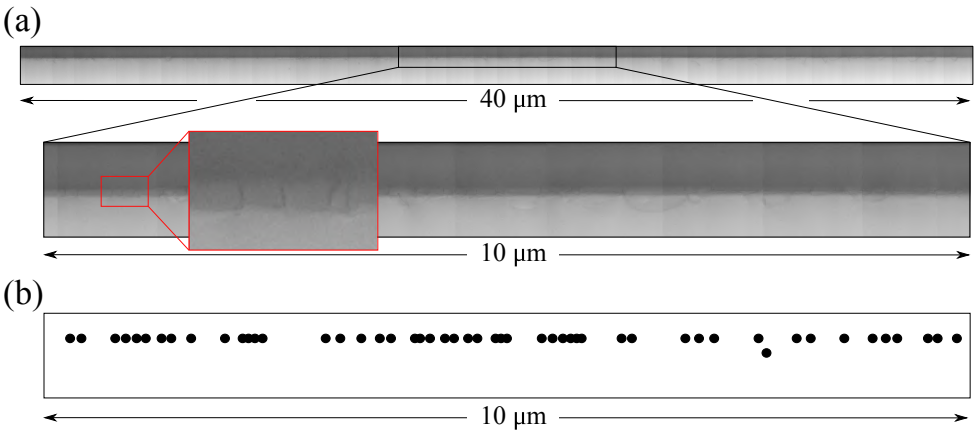

Figure 36: (a) Full lamella used to individuate dislocation positions, and zoom-in on a 10 µm region, better revealing the presence of dislocations. (b) Positions of the dislocations as inferred from analysis of the highlighted region of panel (a).

Afterwards, the sample was prepared for TEM analysis by cutting a thin lamella (final thickness of about 200 nm) inside the FIB-marked area of interest, obtaining a 40 µm long lamella exactly in the region previously analyzed by SXDM. A schematic representation of the resulting alignment between the X-ray map and the TEM lamella is depicted in Fig. 35(c). The lamella was tilted about 10° to visualize misfit dislocation lines at the SiGe/Si interface as streaks. Thus, misfit dislocations running along the beam direction could be identified and distinguished from defects running parallel to the lamella. About 80 TEM images were taken along the whole 40 µm long lamella, obtaining a continuum TEM image still maintaining the required precision to detect single defects. The final image is reported in Fig. 36.

5.1.2 Modeling tilting angle maps

In this section we demonstrate how the two experimental characterizations described above can be linked together on theoretical grounds. We recall here that tilt angles, as introduced in section 1.2, can be evaluated from the anti-symmetric part of the displacement field $\boldsymbol{u}$ using the relation:

$$\Omega_{\alpha\beta} = \frac{1}{2}\left(\frac{\partial u_\alpha}{\partial r_\beta} - \frac{\partial u_\beta}{\partial r_\alpha}\right) \tag{51}$$

Where $\alpha, \beta = x, y, z$; $r_x, r_y, r_z = x, y, z$ and Ω_{xz} (Ω_{yz}) represents a rotation about the y (x) axis. As we have seen in Fig. 35(b) the tilt angles can be easily separated into contributions coming from dislocations running along only one of the two $\langle 110 \rangle$ directions of the dislocations network. Thus in the following we will develop a two dimensional model with dislocations modeled as infinite straight line running perpendicular to the simulation cell. As an example, the tilt angle distribution produced by a 60° dislocation placed at the interface of a 600 nm-thick layer is reported in Figure 37(a). The complete expression of the displacement field induced by dislocations can be found in Appendix A.

In order to model the actual SXDM signal at a specific point of the acquired map, the tilt-angle field must be averaged in the full film volume sampled by the beam defined by the film thickness h (600 nm), the beam impinging angle (35.3° for our experimental setting), the position x, and the FWHM of the beam (120 nm). By scanning over all x positions, a sampling of the Ω_{xz} tilt angle is obtained. The volumetric region contributing to the locally recorded Ω_{xz} value is shaded in gray and the corresponding value is highlighted in the upper plot.

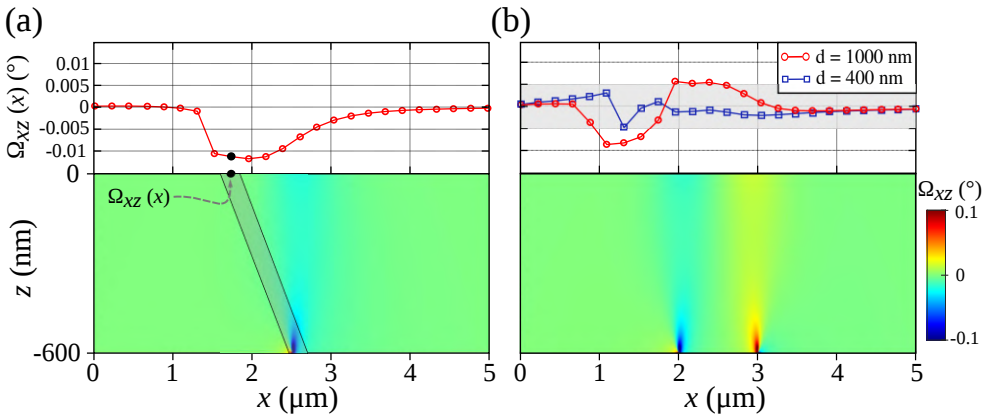

Figure 37: (a) Tilt-angle field produced by a single dislocation with dislocation line along the [110] direction and Burgers vector along the ⟨011⟩ direction. Panel (b) Tilting angles produced by a pair of dislocations with lines along the [110] direction but with Burgers vector with opposite out-of-plane components, placed at a distance $d = 1000$ nm between each other. In the upper plot are reported the signals for this configuration with $d = 1000$ nm and 400 nm. The experimental resolution limit is shaded in gray.

Reproducing the full experimental signal of Figure 35(b) is more difficult as the above-described averaging procedure must be applied to the local tilt angles produced by all contributing dislocations, which requires the knowledge of their individual (x) positions and Burgers vectors. Furthermore, the experimental resolution poses another limit to the possibility to detect single defects. As can be see in Fig. 37(b) the tilt angles signal produced by 60° dislocations with opposite z (growth direction) components of the Burgers vector produces individual tilt angles of opposite sign. Thus, when two dislocation of this kind are too close together (at a spacing of 400 nm for the reported example) their contributions overlap and the resulting signal can become impossible to detect given our experimental resolution limit.

Thus the task of determining the position of individual dislocations was carried out by means of an image analysis of the TEM lamella of Fig. 36(a) carved, as explained above, in the same region previously scanned by SXDM. The informations on the dislocation positions are extracted as in Fig. 36(b), with the possibility of detecting every single MDs running in the direction perpendicular to the lamella. The analysis of the very long (40 μm) lamella revealed the presence of more than 200 dislocations. The abundance of analyzed defects allowed us to directly evaluate, in a statistically significant way, the distribution of distances between adjacent dislocations, which, as clearly

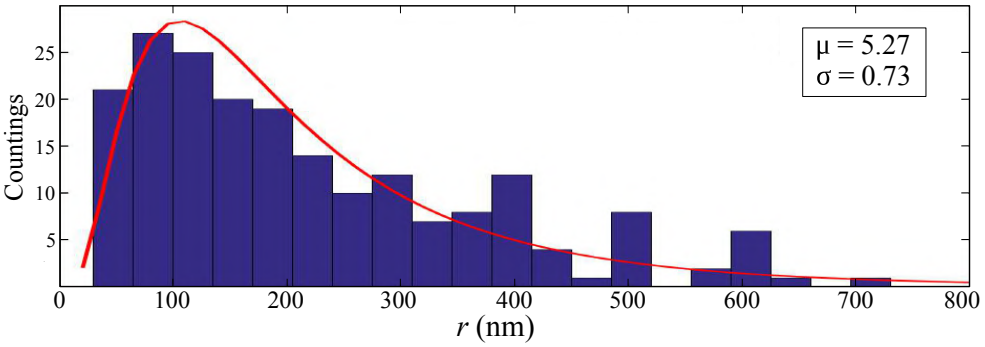

Figure 38: Histogram of the distance between adjacent misfit dislocations and best fit obtained via a log-normal distribution.

shown in Figure 38, is nicely described by a log-normal distribution, defined from the expression:

$$f(r) = \frac{1}{r\sqrt{2\pi}\sigma} \exp -\frac{(\ln r - \alpha)^2}{2\sigma^2} \tag{52}$$

In Eq. (52) α represents the logarithm of the mean distance between adjacent MDs, while σ represents the dispersion of the distribution. We point out here that the same distribution was obtained by Kaganer et al. [104] for the description the nearest neighbor dislocation distribution in $Si_{0.4}Ge_{0.6}/Si(001)$ films. Furthermore, we observed the same kind of behavior in even lower misfit $Si_{0.98}Ge_{0.02}$ system, that will be described in chapter 6. All of these observations give independent and directly measured proofs of the same behavior for systems with different misfit, suggesting a possible general behavior of the defect network.

In order to calculate the complete lattice tilt field and compare it with its distribution reported in Fig. 35(b), we should consider the contribution of all the misfit dislocations located in the position determined by TEM. However, each 60° dislocation can feature one of the two possible Burgers vector orientations (as represented in the example of Figure 37(b)), leading to stress relaxation (called "+" and "−" in the following). Unfortunately, the assessment of the individual Burgers vectors of more than 200 dislocations by high-resolution TEM is an extremely challenging task. To overcome this problem, we have exploited a modeling procedure, based on a Monte-Carlo (MC) algorithm.

In Figure 39(a) the distribution of the tilt angles produced by an array of dislocations positioned precisely as revealed by the TEM analysis and with randomly assigned "+" or "−" Burgers vector is compared with the experimental results (after averaging over the weak dependence on the y coordinate). The agreement is rather poor. Indeed, the tilt-angle maps are very sensitive to local sign of the Burger vectors. To obtain a better correspondence between theory and experiments, we implemented an Ising-like MC procedure where a pair of dislocations is randomly chosen and their Burgers vectors are exchanged ("flipped"). The corresponding theoretical tilt-angle map is re-computed and compared, in norm, with the experimental map.

The total error between the theoretically-predicted and the experimental tilt angles is simply defined as:

$$\Sigma = \sqrt{\int (\Omega_{\text{theor}}(x) - \Omega_{\text{exp}}(x))^2 \, dx} \tag{53}$$

and, if this quantity is lowered after the switch, this one is accepted by the algorithm, otherwise the previous configuration is restored. By iterating the procedure a perfect fit of the experimental data is obtained, as evidenced in Figure 39(b).

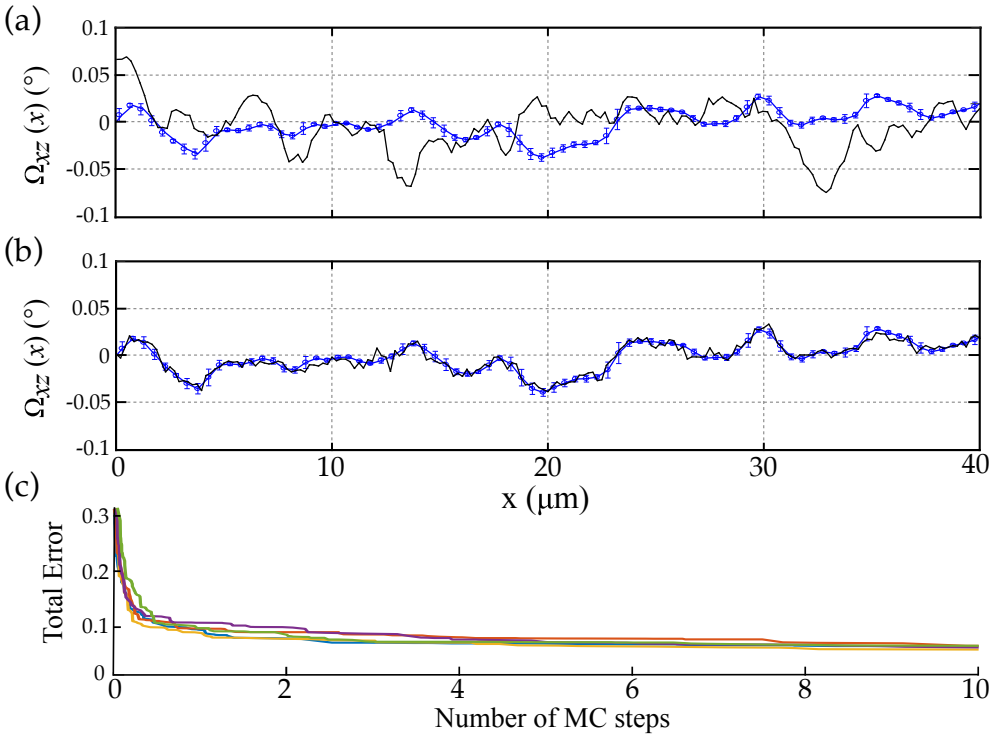

Figure 39: Panels (a) and (b) Comparison between the experimental (blue points with error bars) and the theoretical (black line) tilting angles. Panel (a) Theoretical prediction based on randomly assigned Burgers-vector signs. Panel (b) Theoretical distribution after the Monte Carlo fitting procedure converges. (c) Plot of the total error as function of the simulation step for the converge for a few independent MC simulations.

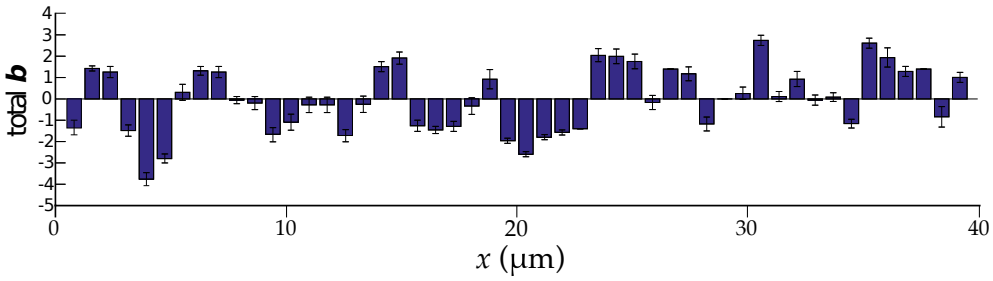

Figure 40: Total Burgers vector computed by summing individual contributions on 800 nm-wide regions. Error bars are estimated based on 100 independent MC simulations.

The convergence of the MC procedure to a tilt-angle map in good agreement with the experiments can be better appreciated by comparing the starting guess map of Fig. 41(a) with the ones corresponding to the converged solution (Fig. 41(c) and to the actual experimental SXDM map of Figure 41(b).

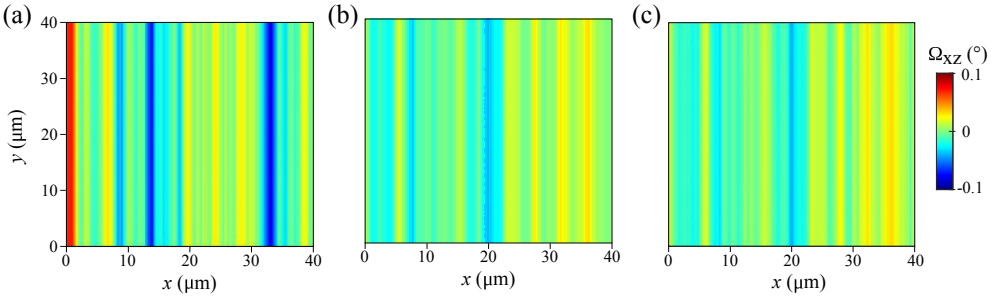

Figure 41: Comparison between theoretically predicted and experimental tilting maps. (a) Starting guess map with random distribution of Burgers vector. (b) Experimental SXDM map and (c) converged solution.

Once a distribution of dislocations and Burgers vector reproducing the tilt-angle maps has been found, it is important to check whether the MC solution is unique. To this goal, we ran a set of 100 independent MC simulations, starting with different initial random distribution of Burgers vectors. A few examples of the converging procedure for some of the MCs runs are reported in Fig. 39(c). From their analysis, it turned out that the best-fit solution in terms of attribution of the Burgers vector sign to all dislocations is not unique, since simulations converging to very similar total error value Σ do not have the same distributions in terms of Burgers vector of the dislocations. This could have been suspected already from Figure 37(b), where it is evident that the signal coming from closely-spaced dislocations with different Burgers vector is mutually canceled [105]), so that inverting their relative position does not change the resulting tilt angle. However, it is sufficient to sum the $+/-$ signs of the Burgers vector over $\approx$ 800 nm (corresponding, on average, to only 4 adjacent dislocations) to obtain a unique best-fit solution. This is well clear from Figure 40, where such sums were performed over the 100 independent converged fitting procedures, and considering all the defects falling inside lateral regions of 800 nm. As can be observed from the error bars in the histograms, with the average performed over independent MC runs, we can assign with good reliability the mean polarization in terms of Burgers vector. In these terms Figure 35(b) uniquely reveal the "local" sign of the Burger vectors distribution, where "local" means $\approx$ 800 nm [106].

5.2 CROSSHATCH PATTERNS

One common phenomena observed during the growth of plastically-relaxed thin films, as the one described in the previous section, is the appearance of a CHP at their free surface. These patterns are particularly simple, featuring two arrays of lines oriented along two orthogonal [110]-equivalent directions. As this reflects the symmetry of the MD network, a link between the epi-layer morphology and plastic relaxation could be easily argued. How-

ever, this one-to-one correlation of the CHP geometry with the MD network is far to be understood, with several experimental observations still remaining unclear. For instance, the distance between adjacent undulations of the CHP, which is not truly periodic, can be orders of magnitude larger than the average distance between dislocations [107]. Even the origin of the undulations is still debated. Both bunching of the surface steps produced by the nucleation and gliding of dislocation loops [107, 104], and the redistribution of surface adatoms induced by inhomogeneities of the strain field at the free surface [108, 109] have been proposed as the root cause for the CHP formation. In this section we will apply the understanding of the misfit dislocation network described above to model the phenomena of CHP formation exploiting the model of surface diffusion presented in Chapter 3 and we will provide direct comparisons with dedicated experiments.

5.2.1 Ideal distribution of dislocations

The approach exploited to describe the CHPs formation is based on surface diffusion, where the flux of adatoms is determined by the gradients in the surface chemical potential μ. The evolution of the surface profile h is determined by the same surface diffusion equation introduce in section 1.3.3:

$$\frac{\partial h}{\partial t} = \nabla M \nabla_s \mu \tag{54}$$

with M the adatoms mobility. This equation is numerically solved by means of the 1+1D model presented in Chapter 3. The introduction of misfit dislocations with assigned Burgers vector and position is made possible by the eigenstrain formalism exploiting the periodic function for the stress/strain fields produced by infinite misfit dislocations reported in Appendix A.

First, this model is applied to a 600 nm-thick $Si_{0.92}Ge_{0.08}$/Si(001) film, fully relaxed by an array of 60° dislocations located at the heterointerface and evenly spaced. In Fig. 42 are reported the results for ideal distributions of dislocations, one with identical Burgers vectors, the other consisting in an array of dislocations with alternated Burgers vector between the two allowed for strain relaxation. The dislocation-dislocation separation is fixed at $d \approx 70$ nm, as required for the complete plastic relaxation of the strain. The simulation cell was set to $L = 1200$ nm with periodic boundary conditions. The initial profile is taken to be perfectly flat, so that the only source of inhomogeneities in the chemical potential is due to the presence of the strain field associated with the network of MD itself, which generates a gradient in the chemical potential. The latter induces a deformation of the surface profile, which is controlled by the balance between elastic and surface energy. As can be observed in Fig. 42(a), undulations develop and evolve in time until the surface reaches a final equilibrium configuration. Under these ideal conditions the final periodicity matches the one of the underlying MD arrays. This is in accordance with the static model of Ref. [109]. Notice that simulations strongly underestimate the roughness. Actually, the predicted value has no physical meaning, being much smaller than a single lattice parameter. Furthermore, as stated in the introduction of this section, the

typical roughness observed in these low-misfit SiGe films is at the micron scale, with a periodicity several orders of magnitude greater than the typical dislocation-dislocation spacing. In summary the experimental observations cannot be reproduced if an ideal distribution of dislocations is considered.

5.2.2 Design of Experiments

The simulations presented above based on ideal distribution of dislocations even if being too to capture the main features of the CHP clearly show a convergence in evolution from the starting flat geometry to a rough surface profile. Therefore we have designed experiments carefully, in order to analyze the temporal evolution of CHPs, following its evolution during an annealing procedure.

In order to keep, on average, the same distribution of dislocations, we ensured to growth a series of samples already achieving full relaxation. Thus, series of $Si_{0.92}Ge_{0.08}$/Si layer were grown up to a thickness of 3000 nm, ensuring full relaxation. After the growth, we thinned the three sets to different thickness by Chemical Mechanical Polishing (CMP). The first set was negligibly polished reducing the film thickness of less than 20 nm, the second set was thinned down to a thickness of 1500 nm and the third one down to 600 nm. After the CMP process, the roughness of all the samples was in

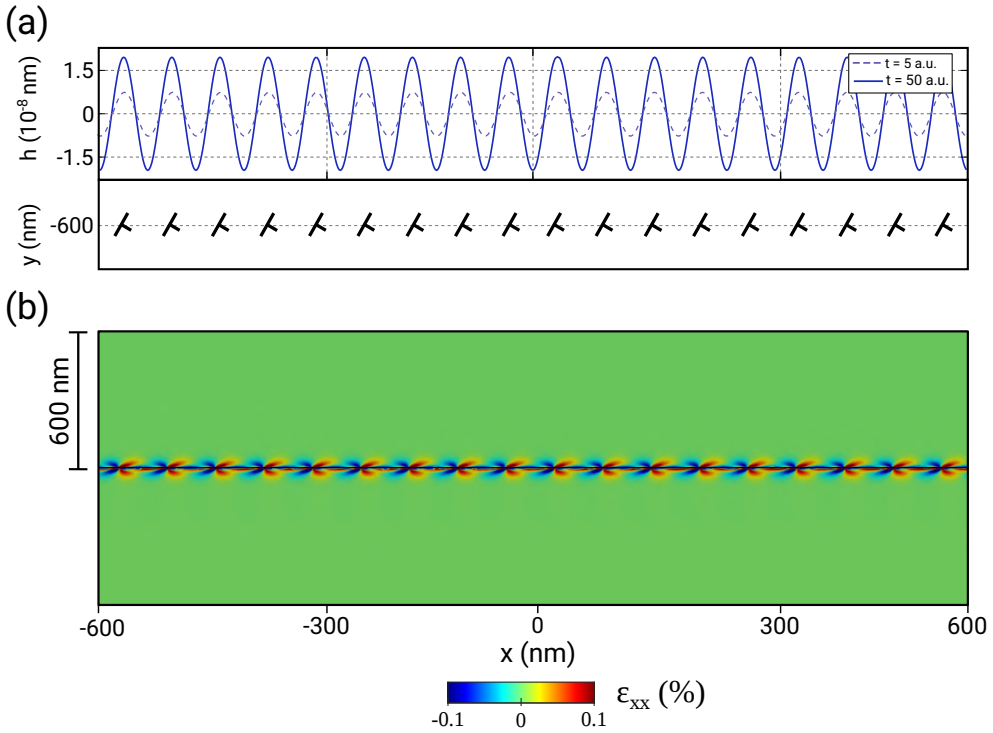

Figure 42: Results for an ideal array of 60° dislocations. (a) Surface profile obtained after the annealing of the initially flat film for t = 5 a.u. and t = 50 a.u. The system has reached an equilibrium: the surface morphology does not evolve anymore upon further annealing. (b) Strain field (ε_{xx}) component resulting in a 600 nm -thick film relaxed by an ideal array of 60° dislocations.

the sub-nm scale, allowing us to rule out any significant role played by step bunches initially present at the free surface in the subsequent evolution. The dependence of the CHP on annealing time was analyzed by annealing these three sets of samples for 10 and 60 min at T = 1050°C.

In Fig. 43 we display Atomic Force Microscopy (AFM) images acquired on the various samples. The surface of all the samples presents a clear CHP, with two sets of perpendicular features aligned along two [110]-equivalent directions. This is interesting per se as CHPs were, so far, observed only after the growth. Here we demonstrate that even if one removes the CHP formed during growth, an annealing following the CMP restores the pattern.

5.2.3 Modeling CHP dynamics

In order to try to reproduce the results of Fig. 43, we replaced in the surface evolution model of section 5.2.1 the ideal distribution with the lognormal distribution (Eq (52)) derived from the analysis of a similar system presented in section 5.1.2. We used the same σ value found in that analysis ($\sigma = 0.7$) and we fixed α based on the present dislocation-dislocation distance giving on average full relaxation of the SiGe film ($\alpha = 4.2$). The orientation of the individual Burgers vectors was randomly assigned.

Simulation results corresponding to the three different sample thicknesses analyzed (600 nm, 1500 nm, and 3000 nm) and for different annealing times are reported in Fig. 44. It is evident that by considering a realistic distribution of dislocations both the typical roughness and the average separation between surface undulations become fully consistent with the experimental findings. Notice that the time scale in the simulations is controlled by the M value of Eq. (54), depending on T [110]. As all samples were annealed at the same temperature, a single rescaling factor should be in principle suffi-

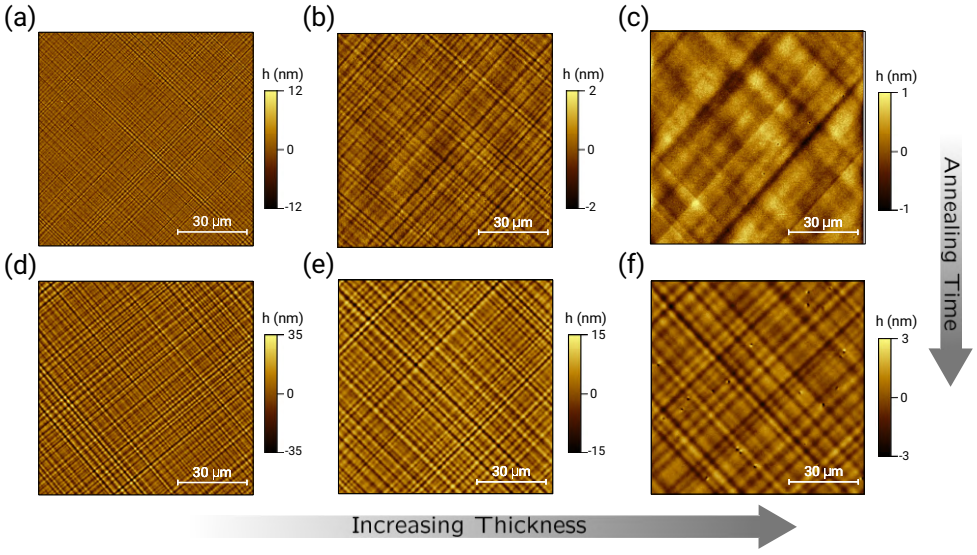

Figure 43: Cross-hatch patterns. AFM images obtained for the three groups of A, B and C. (a)-(c) AFM after 10 min of annealing for the 600, 1500 and 3000 nm-thick samples respectively. (d)-(f) AFM after 60 min of annealing min at 1050°C.

cient to match experimental and simulation times. Indeed, we forced such matching using the two roughness points of the 1500 nm-thick sample, and obtained all other results displayed in Fig.44(a) with no further readjustment. The overall quantitative, time-dependent agreement between experimental data and simulations is excellent.

With the validation of the proposed model, we can now exploit it to directly interpret the interesting physical behavior of the CHP. For instance, the lower ρ value observed for increasing film thickness is readily explained: the dynamics of CHP formation is entirely determined by the magnitude of strain inhomogeneities at the free surface, which is obviously lowered by increasing the film thickness, when the sources of the strain field at the heterointerface get more "buried".

Besides the value of the roughness, the other important feature characterizing the CHP is the typical distance between surface undulations. In Fig. 44(b)-(c) we report the surface profiles by AFM taken along one of the two equivalent [110] CHP directions, for the 3000 nm-thick sample thinned down to 600 nm and the 3000 nm-thick sample after 60 min of annealing. This can be directly compared with the simulated profiles in panels (d) and (e) for the corresponding two film thicknesses. Albeit qualitatively, we can clearly see that our model correctly describe the increase of the typical dis-

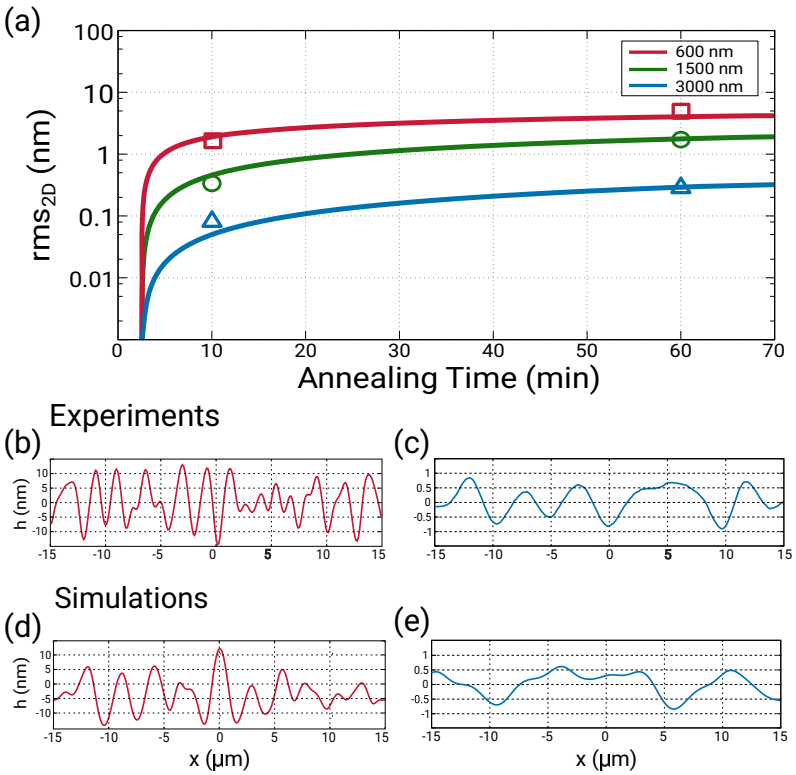

Figure 44: (a) rms_{2D} roughness evolution predicted by the simulations in solid lines and experimental results for the three sample groups A, B, and C (triangle, circle and squares respectively) after 10 and 60 min of annealing. The scan of the experimental surface profiles along on of the two [110] directions for the 600 nm and 3000 nm samples after 60 min of annealing are reported in (b) and (c) and the corresponding simulated profiles are shown in panels (d) and (e).

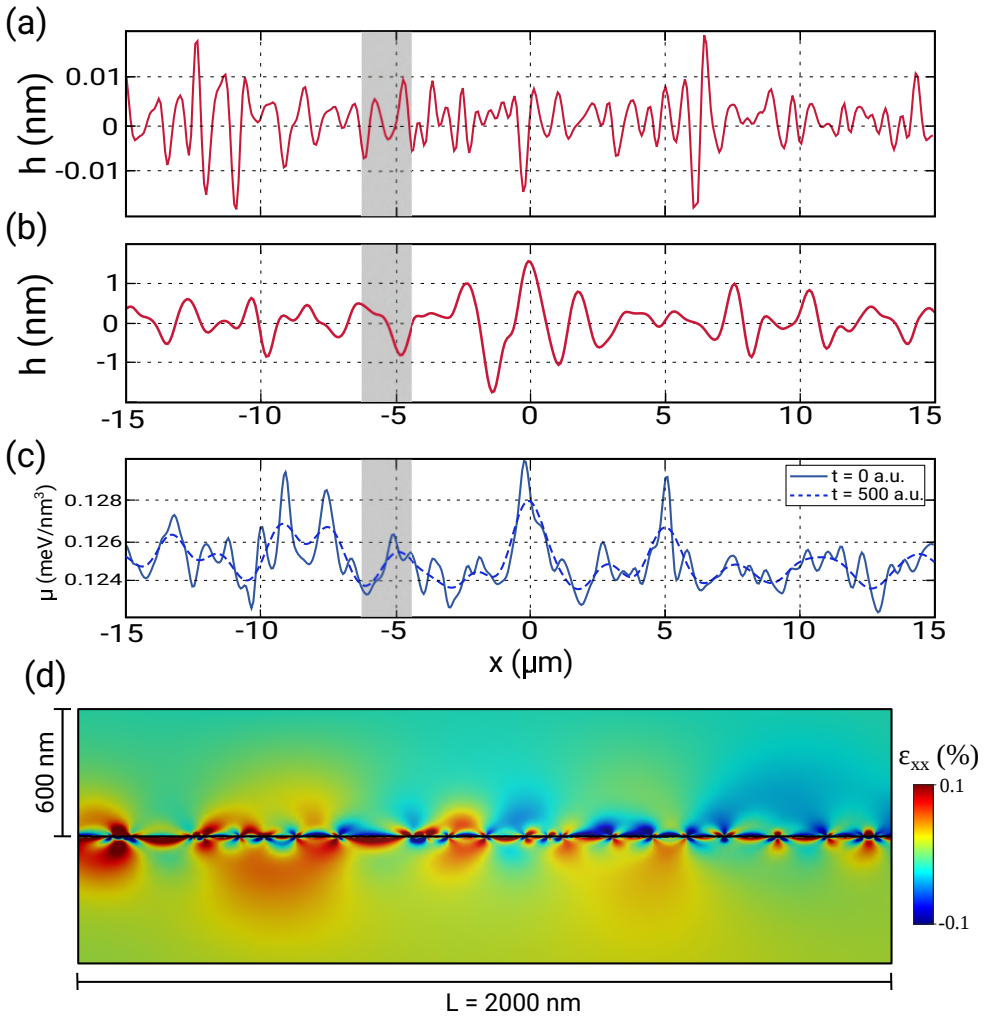

Figure 45: Early stages of the surface roughness evolution for the 600 nm sample. Panels (a) and (b): surface profile obtained after the annealing of the initially flat film for $t = 1$ a.u. and $t = 500$ a.u. Panel (c) plot of the surface chemical potential for after the same two annealing time. Panel (d) strain field (ε_{xx}) calculated in the same 2000 nm region shaded in panels (a)-(c).

tance between CHP peaks, related to the fading-out of the strain field modulation induced by the MD network in thicker epi-layer.

The dynamics of the earlier stages of CHP formation for the 600 nm sample can be better appreciated by looking at Fig. 45. The initial response of the system consists in fast-growing high-frequency undulations (panel (a)) that tend to disappear in later stages of the evolution, when larger λ and larger amplitude oscillations develop, as shown in panel (b). This behavior is consistent with the evolution of the surface chemical potential μ reported in panel (c). Furthermore, we report in panel (d) the strain field produced by the MD network in the same 2 μm area shaded in panels (a)-(c). The difference with respect to the ideal dislocations distribution can be easily appreciated by comparing it with Fig. 42. It is evident that the non-uniform distribution of the dislocation locations give rise to superpositions of the strain field resulting in the more complex dynamical evolution of the surface pro-

file, finding an equilibrium wavelength λ much larger than the dislocation-dislocation distance.

The above reported analysis was based on annealing of initially flat, fully-relaxed epilayers. This procedure yields clear advantages. We notice, indeed, that CHPs in the literature are usually analyzed directly after growth. As a consequence the observed pattern corresponds to some unknown stages (depending on the deposition conditions) of evolution towards equilibrium, making it very hard to rationalize quantitative estimates in a broader context.

6 THREADING DISLOCATIONS IN HETEROEPITAXY

The characterization of the misfit dislocation networks and their effect on the surface morphology, subject of the previous chapter, represent a first building step towards the understanding of the mechanism of strain relaxation in thin heteroepitaxial layers. However the active defects in the relaxation process (misfit dislocations) are unavoidably linked to the presence of threading arms, which do not take part in relieving the misfit strain but are particularly detrimental for technological applications since they run through the layer up to the free surface. Thus, an understanding of the entire relaxation process requires also the description of the behavior of the TD and the physical parameters that can help in controlling their densities. This analysis poses different challenges since the *post mortem* characterization provided in the previous chapter is not able to give information on the dynamical process of plastic relaxation and thus on the mechanisms leading to the observed density of defects. In this chapter we shall exploit the Dislocation Dynamics approach described in chapter 3 in order to follow the plastic relaxation during its evolution and provide an interpretation to the observed distribution of threading arms.

6.1 LOW-MISFIT LIMIT: UNIAXIAL RELAXATION

In this section we shall provide an explanation of experiments performed on very low-misfit SiGe layers. Results show that it is possible to promote the gliding of the dislocation for very long paths (up to tens of centimeters) by starting from a pre-existing distribution of TDs at the rim of the wafer. This finally produces uniaxial distribution of dislocations where the TDs can glide before encountering a deposited MD. By dedicated DD simulations we will enlighten the importance of the blocking mechanism between TDs and MDs and we will show how the experimental results can be interpreted in terms of their interactions.

6.1.1 Experimental characterization

A series of very low-misfit SiGe layers with nominal content of 2% in Ge were grown by SILTRONIC in a CVD reactor on 300 mm Si wafers in an atmospheric pressure high temperature process. A high deposition temperature was used to maximize glide of dislocations. After layer deposition, the samples were annealed for 60 min at 1050°C. Two thickness series (ranging from 250 nm to 10 μm) were grown on different substrates to study the onset of relaxation: In series A the substrate is a polished Si wafer. In Series B a high-defective region at the rim edge of the Si(001) wafer was created before the deposition of the $Si_{0.98}Ge_{0.02}$ epi-layer as schematically depicted in Fig-

ure 46. Details about the rim fabrication and composition did not obtained clearance for publication at the moment of this Thesis submission and they cannot be revealed.

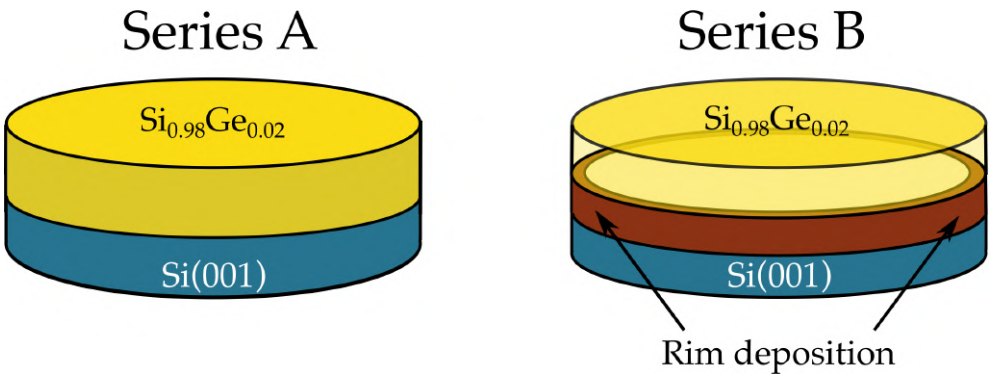

Figure 46: Schematic samples design. Two thickness series of $Si_{0.98}Ge_{0.02}$ layers were grown on top of standard 300 mm Si wafers for Series A, and on substrates with a high defective rim deposited at the wafer edge before epilayer growth (series B).

For revelation of threading dislocations, in situ vapor phase etching was carried out after annealing of the samples. The resulting etch pits were counted in the central region of the wafer. Additionally, modified Secco etching was carried out on some wafers. It has been shown that etching can reveal the misfit segment associated with the TD's. For this, the etch removal was chosen to be higher than the layer thickness, to etch through the SiGe/Si interface and make misfit dislocations visible. Composition and strain analysis of the layers was carried out by High-Resolution X-ray Diffraction (HRXRD). The center positions of the wafers were analyzed to calculate the in-plane and out-of-plane lattice constant of the epitaxial layers. For analysis of misfit dislocation distribution on the global wafer scale, X-ray diffraction topography (XRT) was carried out by scanning the whole wafer. Misfit dislocations weaken the intensity of the diffracted beam as lattice planes around the dislocation are slightly bent and therefore don't contribute to the diffracted intensity. Misfit dislocations or bundles of misfit dislocations appear as dark lines in XRT images.

The relaxation behavior with increasing layer thickness of samples grown on standard substrates (Series A) is presented in Figure 47. HRXRD analysis shows, that samples below 1µm thickness are growing pseudomophically to the Si substrate. However, the 1 µm sample already contains threading dislocations ($\approx 1 \times 10^3$ cm^{-2}), showing that the layer has already started to relax, but the degree of relaxation is below the resolution capability of HRXRD.

With increasing thickness, the degree of relaxation as well as the TDD rises quickly. Full relaxation is only achieved for samples thicker than 5µm, the final TDD level was found to be around $2-3 \times 10^4$ cm^{-2}. During the relaxation process, formation of typical surface roughening (cross-hatch pattern) can be observed [111]. For Series B the relaxation behavior is also displayed in Figure 47(a). Here, relaxation sets in at lower thickness (350 nm). Again, the critical thickness from XRD is only an apparent value, as samples with a

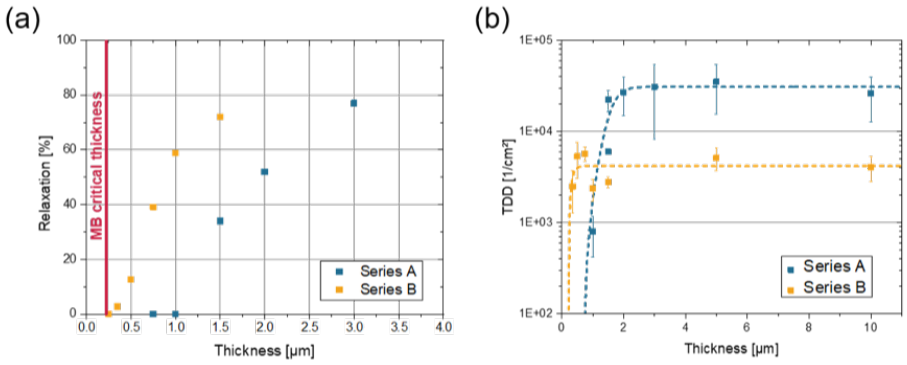

Figure 47: Degree of relaxation measured by HRXRD (a) and TDD from HCl etching (b) with increasing layer thickness on substrates with and without a backside deposition: The relaxation increases with increasing thickness for both substrate types, but is shifted to lower thicknesses in series B. The TDD level for Series B is approximately one order of magnitude lower.

degree of relaxation of 0% already exhibit a TDD. The degree of relaxation increases with increasing layer thickness, similar to series A. The TDD is near its final level ($2-4\times10^3$ cm^{-2}) as soon as relaxation of the layers sets in, saturating at a level about one order of magnitude lower the samples from series A.

Additionally in the very early stages of relaxation (350 nm thickness), long, extended "stair-case"-like pile-ups of threading dislocations run over the whole wafer in the ⟨100⟩ diagonals as can be seen in Fig. 48. The step height of these pile-ups is ranging from a few nm to hundreds of µm.

Secco etching to the SiGe/Si interface reveals the misfit dislocation segments associated to the TD's (figure 49). The pile-up forms the border between two perpendicular arrays of misfit dislocations. The misfit dislocations ending in a threading arm at the location of the staircase pile-up extend across the whole wafer and end at the wafer edge. In addition to

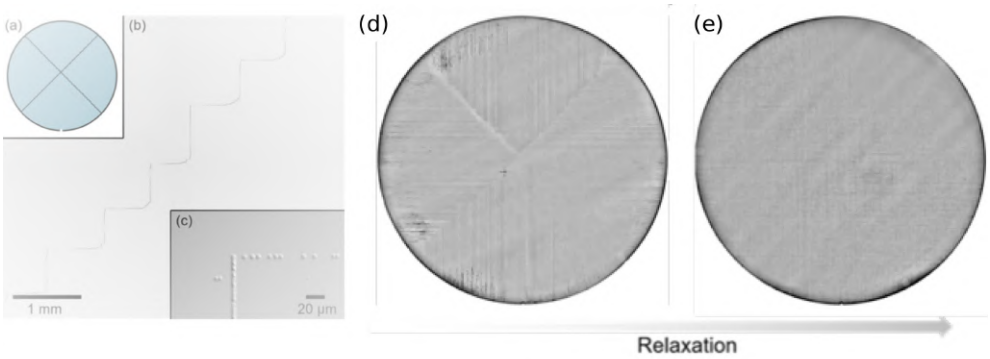

Figure 48: Schematic distribution of staircase pile-ups (a) and micrographs of the etched 350 nm sample of series B (b) and (c): Staircase pile-ups of etch pits run across the whole wafer in the <100> axis of the wafer indicating multiple blocking events in these areas. (c) and (d) X-ray Topographs of samples of series B with thickness of 350 and 500 nm, respectively.

misfit dislocations connected to the edge of the wafer, very short segments can be found within the unidirectional arrays (Figure 49(c)).

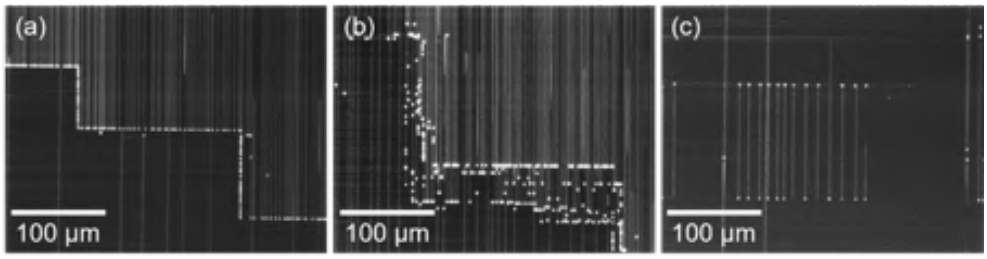

Figure 49: Dark field micrographs from Secco etched samples. The secco etch reveals the corresponding misfit segment of the threading dislocation. In (a) the blocking mechanism for the 350 nm sample is displayed. Each etch pits has its individual line segment, which can be followed across the whole wafer to the edge. At higher thickness (b) the pile-up begins to resolve as the dislocations can overcome the glide barrier. In (c) random nucleation of half loops can be witnessed.

6.1.2 Modeling uniaxial relaxation

The results reported in Fig. 47(a) clearly show how the plastic relaxation process for the samples of series B is shifted to lower thickness with respect to the ones of series A. Indeed, the starting point of relaxation is really close to the Matthews and Blakslee critical thickness (see section 2.5.1). This results can be interpreted as due to the presence of a high-defective region at the edge of the substrate that provides a "reservoir" of threading arms ready to relax as soon as the growing film reach the critical thickness. Furthermore, the uniaxial distribution of MDs developed during these early stages of relaxation (see Fig. 48(b)), demonstrate that nucleation of new loops has not yet started. The final effects of providing this reservoir of preexisting TDs is to significantly reduce the TDD by eliminating the random nucleation of loops for the first stages of the relaxation (as happens in the "standard" biaxial relaxation). Arrays of parallel dislocations without a perpendicular counterpart are formed in the different quarters of the wafer, enforced by geometric constrains of the circular wafer. The interaction and blocking between dislocations can be confined to the $\langle 100 \rangle$ diagonals, where perpendicular dislocation arrays meet, forming extended staircase-like groupings of etch pits as in figure 48, which resolve as soon as the thickness increases.

The witnessed blocking and resolving process between single dislocations has been simulated by means of the DD model presented in Chapter 3. The simulations mimick the early-stages of the process experimentally observed by assuming that pre-existing TDs move in a nearly-unrelaxed $Si_{0.98}Ge_{0.02}$ film until they encounter an already deposited MD in the direction orthogonal to its motion. Two examples of simulation results are reported in Fig. 50 for the 350 nm (a) and 500 nm (b) cases. In the thinner layer, the TD (red line in the figure) glide towards the already deposited MD (blue line in the figure), but as soon as the TD start feeling the interaction with the MD it slow down its motion until it eventually stops, thus leading exactly to the

blocking behavior observed in Fig. 49(a) where a single MD is sufficient to block an array of running threadings. The lateral sizes of the (periodic) cell are chosen to be of 5μm in dimension in order to closely reproduce the initial stages of an unrelaxed epi-layer (resulting in a degree of relaxation ≈ 2%).

Fig. 50(b) shows the results of a simulation with the same parameters but a thickness for the SiGe layer of 500 nm. Here it is possible to see how the running TD, after encountering the deposited MD does not stop but is able to overcame the barrier and thus proceed in its motion through the layer. This corresponds to the experimental observation that the "staircase" groupings of TDs and the uniaxial behavior tend to resolve with increasing thickness of the deposited film, as seen in Fig. 48(e).

However, this transition is not abrupt and indeed, the presence of closely-spaced deposited misfit segments can again provide a blocking barrier for the running TDs. This behavior is exemplified in Fig. 51. This figure reports the blocking conditions, as extracted by DD simulation in terms of Ge concentration (and thus total strain in the epi-layer) and film thickness. Below the line marked as "MB" no relaxation can happen since this corresponds to a system below the Matthews-Blakslee critical thickness. Here even the presence of pre-existing TDs at the rim of the wafer cannot provide relaxation because there the total resolved shear stress is not sufficient to start bending them. This happens when the thickness overcome the MB critical value and specifically the uniaxial behavior observed is expected in the region delimited by the line marked as "1 MD". This correspond to the strain/thickness conditions where a single deposited MD is sufficient to block the running TDs. This blocking conditions tend to resolve moving to higher thicknesses, where more than one, closely-spaced MDs (here simulated as overlapped exactly at the same position) are necessary to provide a barrier for the TDs. Thus, the uniaxial behavior turns to be statistically less significant and eventually reducing to the "standard" biaxial relaxation of thin heteroepitaxial films, condition represented in the upper right corner of Fig. 51.

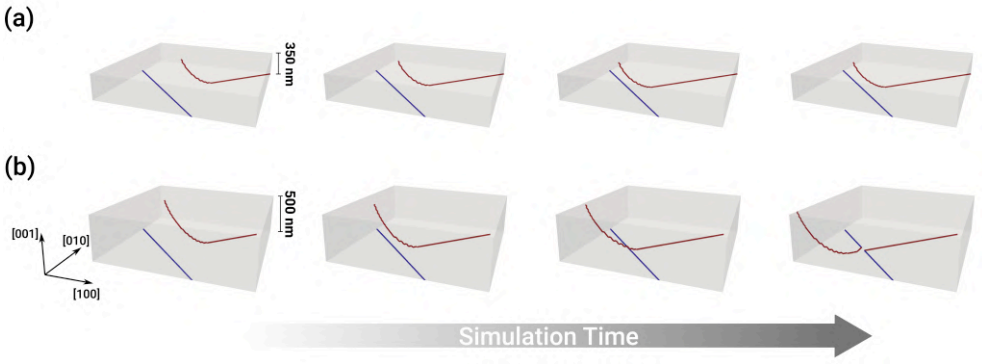

Figure 50: Dislocation Dynamics simulations of the interaction between a deposited misfit segment and a running threading dislocation. (a) Result for a 350 nm $Si_0.98Ge_0.02$ layer, the threading dislocation (in red) runs towards the deposited misfit segment (in blue) and get stopped by the resulting interaction. (b) Same initial configuration of defects simulated in 500 nm thick $Si_0.98Ge_0.02$ layer. Under this conditions the running threading dislocation can overcame the barrier produced by the MD and continue to run through the layer.

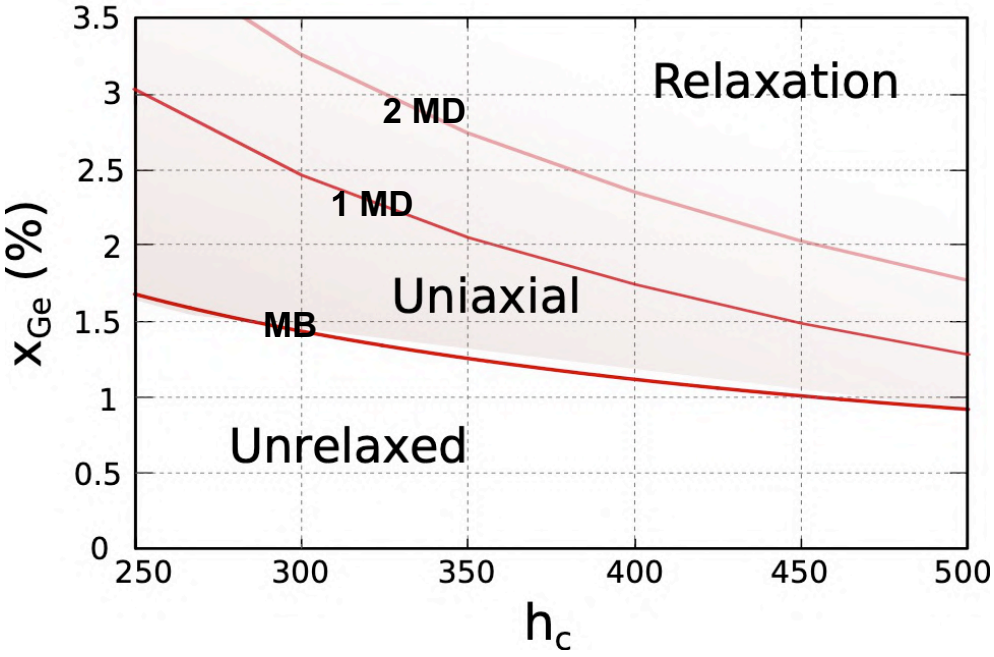

Figure 51: Diagram showing the condition for the uniaxial relaxation condition as obtained by DD simulations. The limiting thickness for the blocking of a TD encountering a MD was evaluated as function of the Ge content in the epilayer. The lines represents the results for MBs critical thickness (marked MB), for a single deposited misfit segment (marked 1 MD), and for two deposited misfit segments (marked 2 MD).

In summary, the combined effect of the low Ge content and the presence of pre-existing TD at the edge of the wafer provides the system a viable path for starting the plastic relaxation of the epi-layer with ordered arrays of defects running in the same direction. This has the effect of elongating the mean path traveled by dislocations before encountering a blocking event, up to centimeters for initial TDs moving from the edge towards the center. The concept of a rim reservoir may be applied to higher Ge-content layers to improve the TDDs and quality of buffer layers for industrial applications. Although the TDD can be lowered by this technique, random heterogeneous nucleation of dislocation loops still occurs, limiting the reduction of the TDD. Controlling this process is challenging, but could lead to an even lower TDD.

6.2 SIGE PILLARS

So far we have only considered growth on planar substrates, which is highly desirable for applications. However, recent attention has been dedicated to more complex morphologies, offering further control over relaxation and TDD and showing promising results for applications where only selected area are required to be defect-free. Between these, 3D heteroepitaxy [16, 112, 113] has been recently shown as a promising technique. This consists in the growth of Ge (or SiGe) onto an ordered array of micrometric, square Si pillars. The combined effect of largely strong out-of-equilibrium growth condi-

tions (high deposition rate of ≈ 5 nm/s, low growth temperatures $\leqslant 750°C$) and mutual shadowing among neighbouring pillars, leads to the formation of vertical heterostructures (VHEs), whose upper region is fully dislocation-free as defects are laterally expelled. By combining the 3D heteroepitaxy approach with the compositional grading (see section 2.5.2), 100% dislocation-free, micron-sized SiGe crystals were recently demonstrated [114]. Here, grading allows to release completely the lattice-mismatch strain by exploiting lateral elastic relaxation [71]). As a result neither misfit dislocations nor TDs, are introduced.

Vertical compositionally graded heterostructures, however, still need further optimization before being easily exploited in applications. Indeed, for a fixed final Ge content target (x_f), 100% dislocation-free crystals can be obtained only by a proper choice of the crystal width and/or Ge compositional grading rate R [71]. In this section we will show how by changing the Si pillar shape via a suitable under-etching procedure [115], it can be experimentally shown that the dislocation density can be further lowered (bringing it back down to zero, in some cases) even for large crystal widths. These results will be directly compared with DD simulations, proving again the good agreement between experiments and the proposed modeling.

6.2.1 Experimental characterization

The SiGe epitaxial growth was performed by Low-Energy Plasma-Enhanced Chemical Vapour Deposition (LEPECVD) (see Ref. [116]) on 4-inch patterned Si(001) wafers. The Si(001) wafers were patterned in two different ways (Figure 52(a) and Figure 52(b), respectively). Both types of patterns are based on optical lithography and reactive ion etching. The first one (see Figure 52 (a)) consists of fabrication by the Bosch process of regular arrays of square, vertical Si pillars with a height h of 8 μm. Further details about substrate patterning and preparation are reported in Ref. [16]. The resulting pillar width w ranges from 2 to 50 μm, and the sides are aligned with the $\langle 110 \rangle$ crystal directions. The second type (see Figure 52 (b)) involves two different dry etching steps. Initially, $0.6 - 1$ μm thick square mesas are produced by vertical etching, after which 3 μm of isotropic etching is performed. This approach results in Si pillars consisting of a thin square mesa and an under-etched neck. The width of the pillar neck is determined by the width of the mesa (ranging from $w = 7$ to 50 μm), assuming that the isotropic etching always removes 3 μm. For further details see Ref. [115].

The epitaxial growth consists of three different steps. First, a 50 nm thin $Si_{1-x}Ge_x$ layer with $x_l = 0.5\%$ is deposited at 750°C and 5.9 nm/s. Second, the compositionally graded alloy is grown at the Ge grading rate of 1.5% μm^{-1} up to the final Ge content $x_f = 0.4$. The Ge content is increased stepwise by $\Delta x = 0.5\%$. The growth temperature is kept constant at 750°C for $x \leqslant 0.1$, while for larger Ge content, it linearly decreases to the final value of 590°C reached at $x_f = 0.4$. Third, a 1 μm thick capping layer at $x_f = 0.4$ is deposited at 590°C and 6.2 nm/s. As illustrated in Figure 52 (c)

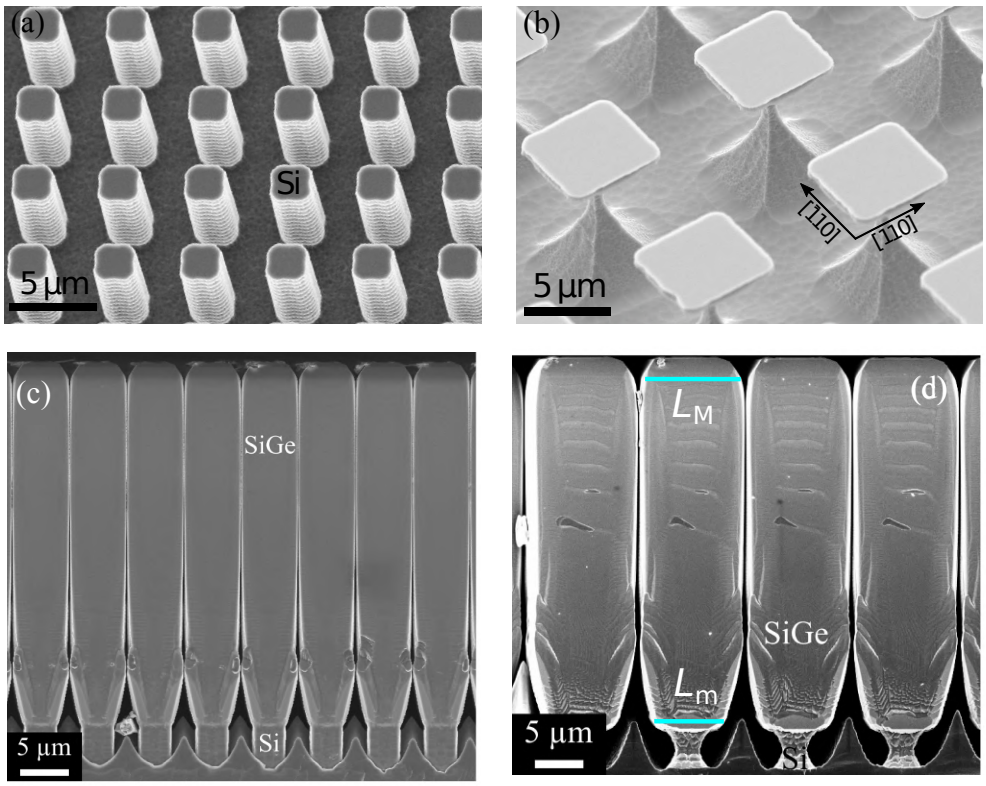

Figure 52: Perspective SEM view of a Si pillars array with vertical {110} sidewalls. (b) Perspective SEM image of an array of under-etched Si pillars width $w = 7$ µm and patterned height $h = 7$ µm. (c), (d) Perspective view SEM images of SiGe crystals grown on vertical (c) and under-etched (d) Si pillars, respectively.

and (d), the epitaxial depositions results in several micrometers tall, isolated SiGe crystals. The SiGe crystals are constituted by {110} sidewalls and on top a central (001) surface bounded by {113} facets [117].

The dislocation analysis is performed by etching the samples and by extensive SEM imaging to count etch pits related to dislocations (see Ref. [118]). The dislocation density is calculated by taking into account a total {110} sidewall surface equivalent to the area of at least 20 pillars to ensure a reliable statistics. Dislocations are present both in the SiGe crystal and in the Si pillar. We denote the corresponding two distinct dislocation densities in the SiGe crystal and the Si pillar as DD_{SiGe} and DD_{Si}, respectively.

The experimentally determined distribution of dislocations within the SiGe and Si regions of the crystal is elucidated in Figure 53. Panel (a) shows the average DD_{SiGe} as a function of the width of the Si pillars and their geometry (vertical or under-etched). As already reported in Ref. [114, 118], narrow and vertical Si pillars allow for a strong elastic relaxation of the epitaxial strain, preventing the nucleation of dislocations. Indeed, the DD_{SiGe} (black spheres) is 0 for 2 µm wide Si pillars, while it reaches a value of $\approx 4 \cdot 10^7 \text{cm}^{-2}$ for $w = 50$ µm. In under-etched Si pillars a much lower DD_{SiGe} is measured in a wide range of Si pillar widths w (red triangles) [115]. The additional compliance effect provided by under-etching becomes less and less effective with increasing w, and practically vanishes for $w = 50$ µm. This is due to the

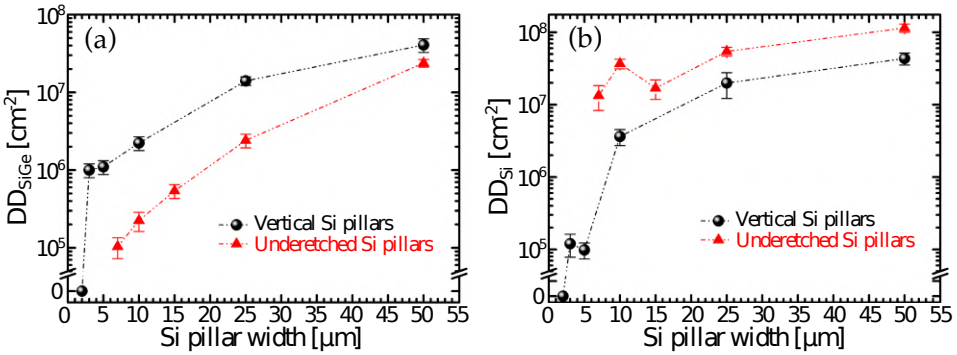

Figure 53: (a) Average dislocation density in SiGe crystals (DD_{SiGe}) deposited on vertical (black spheres) and under-etched (red triangles) Si pillars with different widths. (b) Average dislocation density inside the Si substrate (DD_{Si}) for vertical (black spheres) and under-etched (red triangles) Si pillars.

fact that the under-etching is constantly 3 μm for every pillar width, while the Si neck becomes wider proportionally to w.

On the contrary, Figures 53 (b) indicate that the density of dislocations located in silicon (DD_{Si}) is larger in the case of underetched pillars as compared to the case of vertical Si pillars. Panel (b) shows that the DD_{Si} in vertical Si pillars increases with their width, being 0 for $w = 2$ μm, since in this case all the strain is elastically released ($DD_{SiGe} = 0$ as well), and reaching a value of $\approx 3 \cdot 10^7 cm^{-2}$ for $w = 50$ μm. Surprisingly, the DD_{Si} of under-etched Si pillars (red triangles) is higher for every Si pillar width, increasing from $\approx 1 \cdot 10^7 cm^{-2}$ to $1 \cdot 10^8 cm^{-2}$ between $w = 7$ and 50 μm. A quantitative modeling of this phenomenon is given in Section 6.2.3, however, from the experimental results reported in Figure 53, it is already clear that for small Si pillar widths, where elastic strain relaxation plays a fundamental role, the dislocation dynamics is strongly influenced by the Si pillar geometry. Indeed, for narrow Si pillars ($w \leqslant 10$ μm) the DD_{SiGe} is much lower for deposition on under-etched Si pillars, while the DD_{Si} behave in the opposite way. This is not the case for wide Si pillars (i.e. $w = 50$ μm) where DD_{SiGe} and DD_{Si} are not geometry dependent.

In order to understand the different dislocation behavior, we take a closer look at the spatial distribution of dislocations within the narrow SiGe crystals. Figure 54 (a) and (b) shows cross-sectional SEM images of SiGe/Si crystals deposited on narrow vertical and under-etched Si pillars, respectively. The dashed light blue line indicates the SiGe/Si heterointerface. In (a) the thickness of the layer with $x_l = 0.5\%$ is 8 μm. This ensures vertical growth of the compositionally graded material by reducing the gap between adjacent crystals, without altering the mechanical properties of the system. It is evident that the etch pits related to emerging dislocations are distributed very differently in the two panels. Importantly, dislocations are predominantly located in the SiGe crystal for vertical Si pillars (white arrow in panel (a)), while they are predominantly located in the Si region in the case of underetched pillars and piled-up along the same {111} glide plane (indicated by the red dashed ellipses in panel (b)). Indeed the measured angle in Figure 54 (b) between the [110] direction and the dislocation pile-up indicated by the

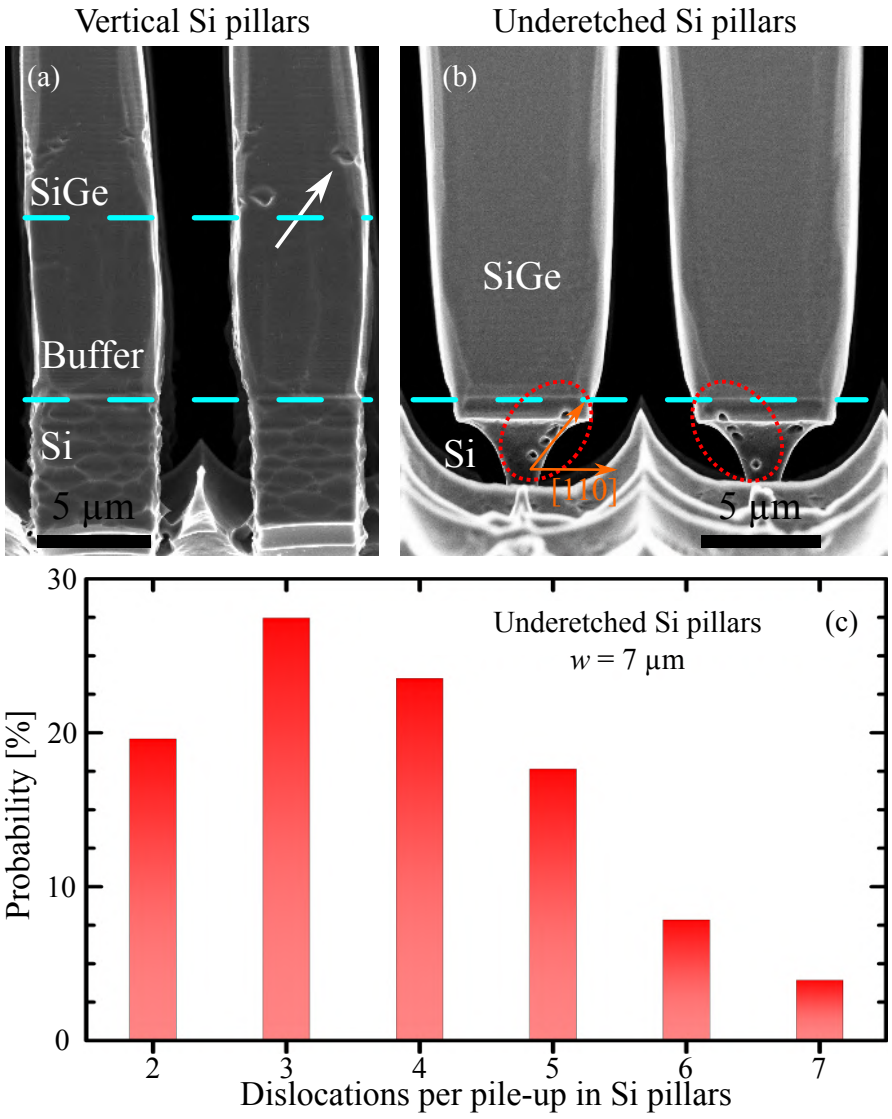

Figure 54: (a) and (b) Cross-sectional SEM images of SiGe crystals deposited on vertical and under-etched Si pillars, respectively, after selective defect etching (width $w = 5$ and 7 µm). The dashed light blue line shows the SiGe/Si heterointerface. The white arrow indicates a dislocation in the SiGe crystal. The the red dashed ellipses in (b) highlight dislocations piled up along a {111} plane. (c) Probability distribution of having a certain number of dislocations per pile-up along {111} planes in under-etched Si pillars ($w = 7$ µm).

orange arrows is about 54°, as expected from the intersection between the {111} glide planes of the dislocations and the [110] direction. By looking at dozens of different under-etched Si pillars, as those of Figure 54 (b), it is possible to measure the probability of having a certain number of dislocations per pile-up. Figure 54 (c) shows the probability distribution of dislocations per pile-up in under-etched Si pillars indicating that 3 dislocations per pile-up is the most likely.

6.2.2 Modeling Underetched SiGe Pillars

Let us now provide a theoretical explanation for the observed decrease (increase) of the number of dislocations in SiGe crystals (underlying Si pillar) as caused by under-etching. The approach exploited in this section to model the plastic relaxation is a 2D implementation of the DD approach coupled to a FEM solver presented in section 3.1. In order to understand the distribution of dislocations revealed in the experiments and how this is affected by under-etching the Si pillar we started by investigating the plasticity onset, i.e. the introduction of the very first dislocation in the system during growth. This was done by evaluating the total elastic energy and by taking the energy difference between the system with and without the dislocation as a function of the pillar height H. The onset of plasticity is found when introducing a dislocation brings the total energy to a net reduction, corresponding to negative values of ΔE.

In these calculations dislocations are placed at the SiGe/Si interface, probing different lateral positions, for each different H, in order to find the minimum-energy position. The difference between the energy with the dislocation placed at that position and the defect-free system is called ΔE_{min}. The evaluations are done by considering the geometry of a pillar grown on an under-etched Si pattern of base 7 μm. As clearly visible in Figure 52 (c), the experimentally-grown pillars show a degree of taper in the vertical directions resulting from a certain degree of lateral growth. In our model we considered a simplified geometry with constant pillar width (Fig. 55) for both vertical and under-etched Si pillars. In order to take care of the dependence of the onset of plasticity with the pillar width we repeated the calculation for the two limiting values of width measured at the SiGe/Si interface ($L_m = 6.6$ μm) and at the pillar top ($L_M = 11$ μm), see also Fig. 52 (c), maintaining a constant neck for the under-etched region of 2 μm.

We started by considering the two possible 60° dislocation Burgers vectors, i.e. $b = [101]a_{Si}/2$ or $b = [\bar{1}01]a_{Si}/2$, (where a_{Si} is the lattice parameter of Si) which features a compressive lobe mainly positioned in the silicon substrate and a tensile lobe in the SiGe epilayer. Such dislocations are typically encountered in SiGe/Si heteroepitaxy of standard 2D films and also in vertical pillars grown with the same parameters of the samples considered in this paper (see Refs. [112, 114]) and are introduced to relax the compressive strain in the SiGe epilayer. However, contrary to what happens in standard vertical pillars, the introduction of a dislocation with one of these two Burgers vec-

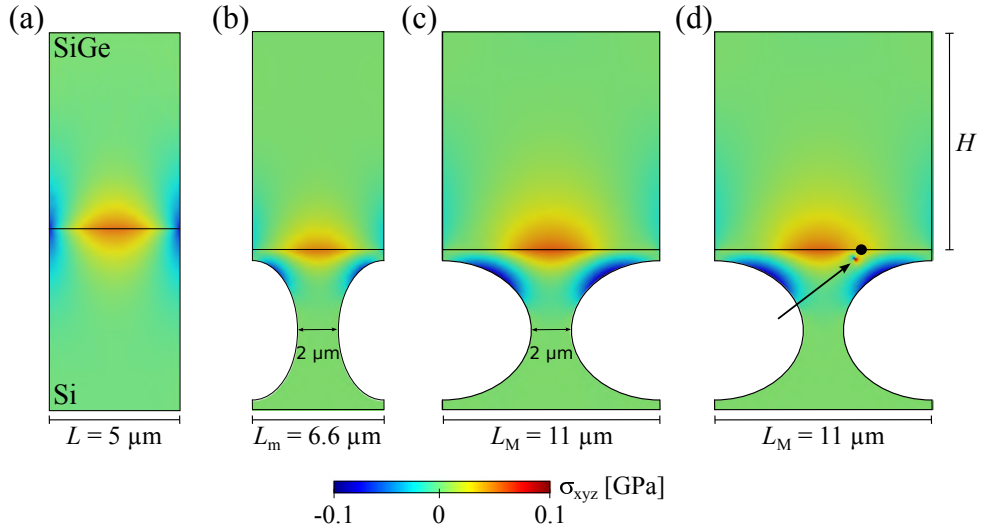

Figure 55: Hydrostatic stress maps (σ_{xyz}) and considered geometry for the vertical (a) and under-etched (b)-(c) Si pillars. The SiGe/Si interface is marked with a black line. The two considered pillar bases L_m (b) and L_M (c) for the under-etched pillar are taken to mimick the extreme values of bases measured on the tapered geometry of the grown pillar as reported in Fig. 2 (c). In panel (d) is reported the stress map for an under-etched pillar with the first dislocation introduced. The filled black circle report its optimal position along the interface while the black arrow represents the result of the energy minimization by means of a dislocation dynamics simulation.

tors inside an under-etched pillar is never energetically favored, as shown in the red region of Fig. 56. Surprisingly, the introduction of dislocations with the opposite sign of the Burgers vector (and opposite orientation for the compressive/tensile lobes) becomes energetically favorable after a certain critical thickness for both the considered values of pillar base (purple region in Fig. 56). In order to understand this evidence it is convenient to look at the stress field reported in Fig. 55 (b)-(c). As it is evident by comparing with Fig. 55 (a), in the presence of under-etching a strongly compressed region is created in the underneath Si pillar close to the free surfaces of the neck. In order to release such stress it is required to introduce a dislocation which adds space in silicon, i.e. the opposite of what happens in the vertical geometry or in standard SiGe/Si heteroepitaxial films.

As we already emphasized, the values displayed in Fig. 56 were obtained, for simplicity, by placing the dislocation at the SiGe/Si interface, in the horizontal position minimizing the energy. Such a position is indicated, for $L_M = H = 11$ μm, by a black filled circle in Fig. 55 (d). By running dislocation dynamics simulations starting from such a position we found out that a slightly lower-energy position located under the interface exists (tip of the black arrow in Fig. 55 (d)). However the energy difference between the two produces negligible changes in terms of the estimate of the critical thickness.

The above described approach, purely based on an energy minimization criterium and used to estimate the onset of plasticity, cannot be reliably extended to treat more advanced stages of relaxation (e.g. by looking at the minimum energy position for a larger number of dislocations) as nucle-

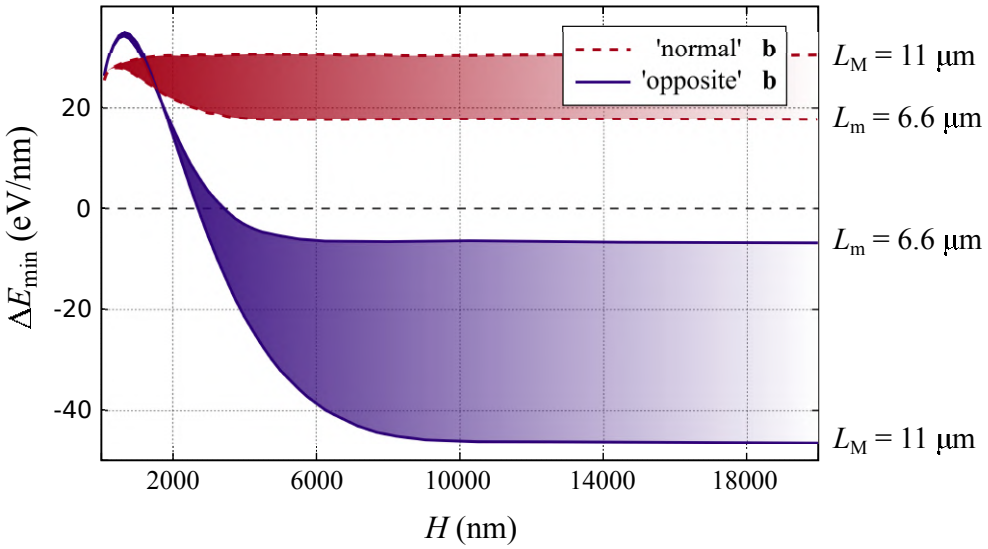

Figure 56: Energy gain for the introduction of the first dislocations in an under-etched pillar with base L with respect to the pillar height H. The formation energy is negative only for dislocations with the opposite Burgers vector b.

ation processes are known to dominate in low-misfit graded layers [61, 91]. The experimental images of Fig. 33 (a) (vertical) and (b) (under-etched) are therefore exploited to proceed with further modeling. They show that dislocations tend to pile-up on the same glide plane, a clear sign of multiple nucleation from the same source. Under this hypothesis we tried to model the observed distribution of dislocations exploiting the dislocation dynamics approach described in section 3.1. Results are discussed and compared with experiments in the next Section.

6.2.3 Comparison between theory and simulations

In order to predict the dislocation distribution, under the hypothesis of dislocation nucleation from the same source, we have placed a first dislocation at the SiGe/Si interface, with both the Burgers vector and the lateral positioning derived in the previous section for both vertical and under-etched Si pillars. Then an iterative procedure is performed by adding a singular dislocation to the same glide plane and finding the resulting stable configuration by means of dislocation dynamics simulations. In the simulations, the first dislocation is kept fixed to the initial position as it is treated as the origin of the source (possibly originated in the 3D system by crossing between dislocations running in perpendicular direction and leading to multiplication [119]). Iterations are repeated until the total energy of the system is lowered by the addition of a further dislocation. Results are shown in Fig. 57 where the energy gain is plotted against the number of dislocations per pileup. As we can see the minimum of this curve corresponds to a number of four dislocations, fully compatible with the experimental results of Fig. 33 (c).

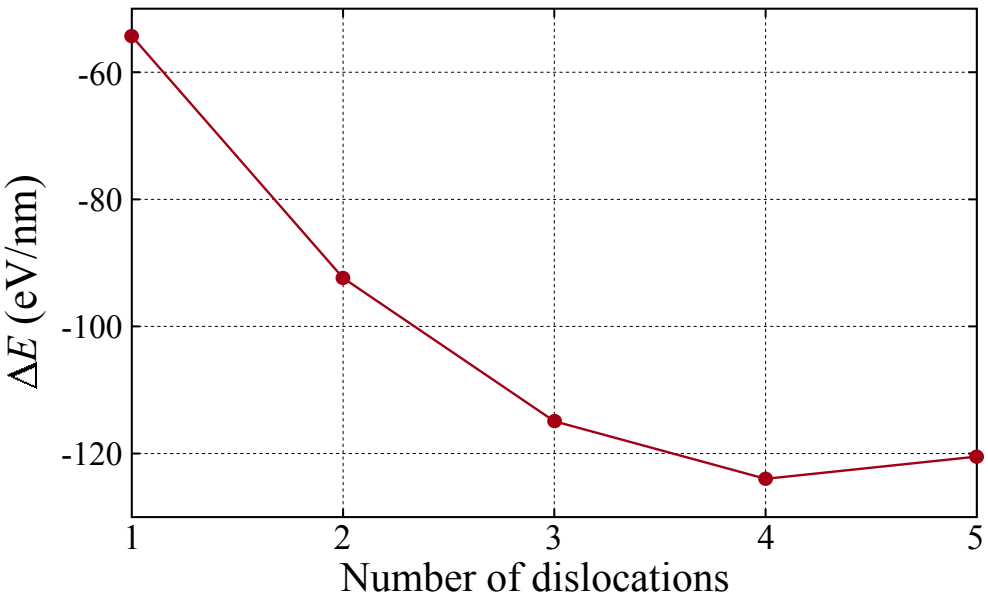

Figure 57: Plot of the energy gain versus the number of dislocations per pileup in an under-etched pillar. The optimal number of dislocations can be deduced to be four by the minimum in this curve because the introduction of a further one will increase the total elastic energy.

At the end of these simulations we are able to predict the optimal position of a pileup inside a pillar along with the total number and the positions of the individual dislocations inside the pileup. The final results of these computations are shown in Fig. 58. In (a) we can see how in under-etched pillars dislocations are pushed inside the silicon region underneath and this is well comparable to the simulation results. In the (b) the simulation is reproducing the behavior observe in standard vertical pillar where, instead, the pile-ups tend to float in the SiGe region, again showing a behavior well-comparable with the experimental results of Fig. 54. Some differences in the theoretical vs experimental distributions can be spotted. This is not surprising taking into account some simplifications considered in the model where the system is described only in 2D and the first dislocation is kept fixed at the exact minimum energy position. As we can see the simulations can well reproduce the behavior shown in experiments with dislocations in vertical pillars floating in the SiGe region, while those in the under-etched ones are pushed into the silicon pillar underneath.

Finally, we wish to comment about another difference in the defects of vertical vs under-etched pillars, revealed by the SEM images of Fig. 54. We recall that misfit and threading dislocations can be distinguished by the etch pits symmetry [118]. Indeed, misfit dislocations with line along the ⟨110⟩ directions generate four-fold symmetric etch pits, while the inclined threading dislocation line results in elongated and asymmetric etch pits. It is clearly visible in Fig. 54 (a) and (b), that the etch pits in the vertical pillars are the result of a threading arm extending toward the lateral surface of the crystal, while in the under-etched ones they result from misfit segments running all across the pillar. We ascribe this difference to the different positioning of the dislocations. In the under-etched case multiplication takes place closer

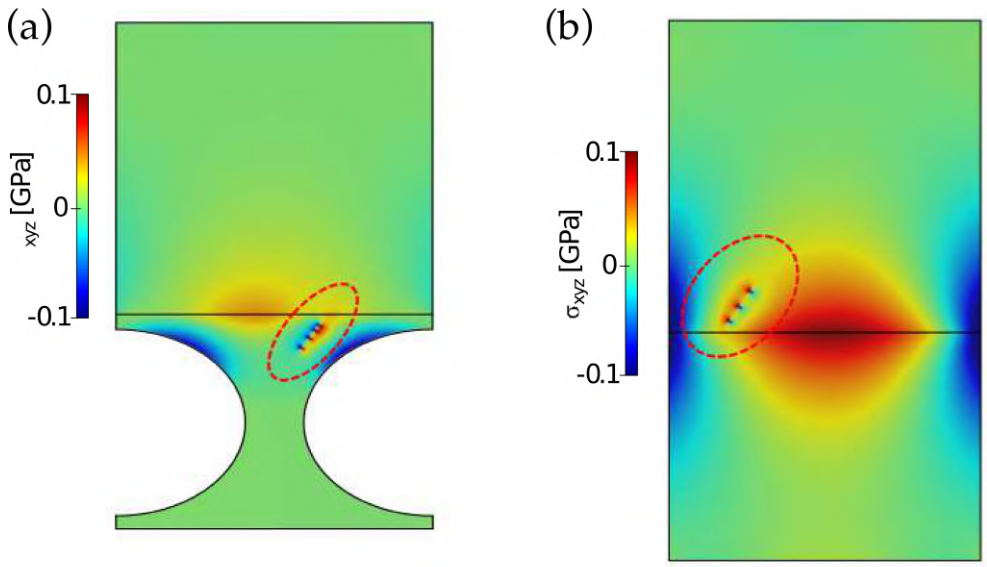

Figure 58: Comparison between experimental SEM images and hydrostatic stress maps from the final stages of the dislocations dynamics simulations for an under-etched pillar, panel (a) - (b), and a vertical one (c) - (d). Experimental images of figure Fig. 55

to the free surfaces. Therefore, dislocation (semi-)loops can more easily fully open, threading arms being expelled in the process.

7 CONCLUSIONS

In this Thesis the process of strain relaxation during the heteroepitaxial growth was modeled by continuum approaches in order to provide a deep understanding of the underlying physical mechanisms and suitable modeling tools for their description. The study was focused on the technology relevant SiGe/Si system. Both the elastic and plastic relaxation processes have been discussed, together with examples of their competing effects. This modeling required the development and applications of different numerical codes able to describe the specific phenomena of interest. The description of plastic relaxation and evolution of dislocation distribution was performed by exploiting a Dislocation Dynamics (DD) [66] approach coupled with the Discrete Continous Model (DCM) [15]. On the other hand, the description of the elastic relaxation required the development of a code able to describe the surface diffusion of material by means of a diffusion equation. This was done by means of a numerical exploiting the Finite Element Method (FEM) to numerically solve the partial differential equation of surface diffusion. Within this approach it was also implemented the possibility of including dislocations on the fly during the simulations.

In chapter 4 we have shown the competing effects of plastic and elastic relaxation by simulations of the growth process of a SiGe layer on Si. The introduction of dislocations during the process of relaxation of heteroepitaxial islands permitted the reproduction of the phenomenon known as *cyclic growth* [120], already well documented in literature by experimental observation [62]. The very same approach was also exploited to reproduce the growth of plastically-relaxed flat films, with the identification of the physical parameters describing the transition between these two growth regimes [120].

In chapter 5 we performed a detailed analysis of the distribution of misfit dislocations in low misfit SiGe/Si layers. Here, by combining advanced experimental characterization by means of a suitable theoretical model we were able to interpret the tilting angle maps obtained from X-ray analysis in terms of contributions coming from single defects [106]. Furthermore, in this chapter we demonstrated also how the understanding of the distribution of misfit dislocations permitted to reproduce the well-known phenomena of crosshatch patterns formation by implementing. This was done by implementing this realistic distribution of dislocations inside the surface diffusion model discussed above [111].

Finally in chapter 6 we have shown the application of the DD approach to study the plastic relaxation of low misfit thin films and heterostructures. Particular attention was focused here to study the mechanisms leading to a reduction in the density of threading dislocations. For the case of low-misfit planar films simulations have shown how an unexpected observed phenomenon of uniaxial relaxation can be interpreted in terms of interaction

between misfit and threading dislocations. Furthermore, in the study of the relaxation of vertical heterostructures (VHEs) we have shown the interaction of dislocations with local elastic fields. This latter was due to the shape of the substrate for the growth of the heterostructures on top of deeply patterned substrates. The presence of this local elastic fields produced a drastic change in the dislocation distribution, changing the kind of defects nucleated and pushing them away from the top active area of the heterostructures [121, 122].

The aforementioned results opens interesting perspective for future studies. Indeed, the optimization of the growth process oriented at lowering the number of threading dislocations is one of the key research topic in the field of heteroepitaxial growth. This optimization procedure cannot be done by a trials and errors procedure and thus the exploitation of the codes developed in this Thesis can provide convenient support to the experiments. Examples could be the shape optimization of substrates to be used for the growth of VHEs or the optimization of the process providing the observed uniaxial relaxation in low-misfit flat films.

From the modeling point of view the codes here proposed can be further developed. The inclusion of additional contributions to the surface energy in the diffusion model can move the description towards more realistic systems. For example, accounting for surface orientation can be used to model the formation of crystallographic facets. Finally, despite we provided a first application of a 2D code able to tackle simultaneously elastic and plastic relaxation, the methodology can be extended further by considering 3D systems. The development of the DCM in the same Finite Element environment for solving PDEs (FEniCs) represents a first step in this direction.

A ANALYTICAL SOLUTIONS FOR DISLOCATION ARRAYS

This appendix reports some analytical expressions for the displacement and stress fields of dislocation arrays near a free surface. These expression were exploited in all the models presented in this Thesis whenever periodic boundary conditions (PBCs) were required when treating systems with the presence of dislocation near a free surface.

A.1 DISPLACEMENTS

The expressions for the displacements of dislocations near a free surface are reported here from Ref. [100]:

$$
\begin{aligned}
u_x =& -\frac{b_x}{4\pi(1-\nu)}\left[\frac{x(y-h)}{((y-h)^2+x^2)}-\frac{x(y+h)}{((y+h)^2+x^2)}+\arctan\left(\frac{y-h}{x}\right)\right.\\
&\left.+\arctan\left(\frac{y+h}{x}\right)\right]\\
&-\frac{b_y}{2\pi}\left[\frac{(y-h)^2-x^2}{4(1-\nu)\left((y-h)^2+x^2\right)}+\frac{(1-2\nu)\log\left((y-h)^2+x^2\right)}{4(1-\nu)}\right]\\
&+\frac{b_y}{2\pi}\left[\frac{(h+y)^2-x^2}{4(1-\nu)\left((h+y)^2+x^2\right)}+\frac{(1-2\nu)\log\left((h+y)^2+x^2\right)}{4(1-\nu)}\right]\\
&+\frac{b_x h}{\pi}\left[\frac{(1-2\nu)x}{2(1-\nu)\left((h+y)^2+x^2\right)}-\frac{xy(h+y)}{(1-\nu)\left((h+y)^2+x^2\right)^2}\right]\\
&-\frac{b_x h}{2\pi}\left[\frac{h\left((h+y)^2+x^2\right)+2x^2y}{2(1-\nu)\left((h+y)^2+x^2\right)^2}+\frac{(1-2\nu)(h+y)}{2(1-\nu)\left((h+y)^2+x^2\right)}\right]\\
u_y =& \frac{b_x}{2\pi}\left[\frac{x^2-(y-h)^2}{4(1-\nu)\left((y-h)^2+x^2\right)}+\frac{(1-2\nu)\log\left((y-h)^2+x^2\right)}{4(1-\nu)}\right]\\
&-\frac{b_x}{2\pi}\left[\frac{x^2-(h+y)^2}{4(1-\nu)\left((h+y)^2+x^2\right)}+\frac{(1-2\nu)\log\left((h+y)^2+x^2\right)}{4(1-\nu)}\right]\\
&+\frac{b_y}{2\pi}\left[\frac{x(y-h)}{2(1-\nu)\left((y-h)^2+x^2\right)}+\arctan\left(\frac{x}{y-h}\right)\right]\\
&-\frac{b_y}{2\pi}\left[\frac{x(y+h)}{2(1-\nu)\left((h+y)^2+x^2\right)}+\arctan\left(\frac{x}{h+y}\right)\right]\\
&-\frac{b_x h}{\pi}\left[\frac{y\left((y+h)^2-x^2\right)}{2(1-\nu)\left((h+y)^2+x^2\right)^2}+\frac{y+h}{(y+h)^2+x^2}\right]\\
&-\frac{b_y h}{\pi}\left[\frac{xy(y+h)}{(1-\nu)\left((h+y)^2+x^2\right)^2}+\frac{(1-2\nu)x}{4(1-\nu)\left((y+h)^2+x^2\right)}\right]\\
u_z =& \frac{b_z}{2\pi}\left[\arctan\left(\frac{x}{y-h}\right)-\arctan\left(\frac{x}{y+h}\right)\right]
\end{aligned}
$$

A.2 ANLAYTIC SOLUTION FOR DISLOCATIONS ARRAY NEAR A FREE SURFACE

In this section a complete derivation of the σ_{xx} component of the stress field generated by a periodic array of dislocations is reported. The considered system is illustrated in Fig. 59 where two ordered arrays of parallel straight dislocations of Burgers vector $\mathbf{b} = (b_x, b_y, b_z)$ are present, laying in a plane displaced by a value h from to the top free surface. As the expression for the total stress field can be achieved by a superposition between the stress generated by the dislocations running along the x and z directions we can focus our attention only on the latter.

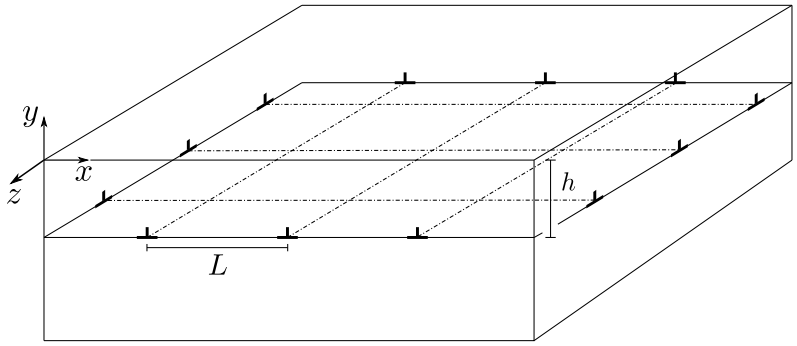

Figure 59: Schematic representation of the system. Two set of periodic parallel dislocations (one set being perpendicular to the other) run along the xz plane at a distance h from the free surface. The distance between adjacent dislocations is set equal to L in both directions.

The stress field for a single dislocation running along z direction, including the corrections evaluated by Head in Ref. [55] to account for the presence of the free surface, is an expression dependent on b_x and b_y:

$$\begin{aligned}\sigma_{xx} = &-\frac{\mu b_x}{2\pi(1-\nu)}\Bigg\{\underbrace{\frac{(y+h)[3x^2+(y+h)^2]}{\left[x^2+(y+h)^2\right]^2}-\frac{(y-h)[3x^2+(y-h)^2]}{\left[x^2+(y-h)^2\right]^2}}_{A}\\ &\underbrace{+2h\frac{(y+h)(y-h)^3-6y(y-h)x^2+x^4}{[x^2+(y-h)^2]^3}}_{B}\Bigg\}\\ &+\frac{\mu b_y}{2\pi(1-\nu)}\Bigg\{\underbrace{\frac{x\left[x^2-(y+h)^2\right]}{\left[x^2+(y+h)^2\right]^2}-\frac{x\left[x^2-(y-h)^2\right]}{\left[x^2+(y-h)^2\right]^2}}_{C}\\ &\underbrace{-\frac{4hx\left[x^2(2h-3y)+(y-h)^2(2h+y)\right]}{\left[x^2+(y-h)^2\right]^3}}_{D}\Bigg\}\end{aligned} \tag{55}$$

where $\mu = E/2(1+\nu)$, with E and ν respectively the Young's modulus and the Poisson's ratio of the medium. The stress field σ_{xx}^{xPBC} generated by the array can be obtained summing the stress fields of infinite individual dislocations displaced from each others by L. In order to perform the calculations let us consider separately the contributions from the b_x component of the Burgers vector, i.e. terms A-B and those from the b_y component, i.e. terms

C-D. Note that for dislocations running along z direction b_z represents the screw component of the Burgers vector which does not contribute to σ_{xx}.

A.2.1 Contributions from b_x

Let us focus firstly on the terms depending on b_x. The two terms in A represent the dipole construction, σ^{D}_{xx}, with the bulk and image contributions, and in order to find their periodic expression we have to evaluate a sum like:

$$\sigma^{D\text{-}xPBC}_{xx}(x,y;L) = \sum_{n=-\infty}^{+\infty} \sigma^{D}_{xx}(x-nL,y) \tag{56}$$

The sum in Eq. (56) can be evaluated following the derivation reported in [54], and results in:

$$\begin{aligned}\sigma^{D\text{-}xPBC}_{xx} = \frac{\mu b_x}{(1-\nu)L}\Bigg[&\frac{\pi Y_+(C_{Y_+}c_X-1)-S_{Y_+}\left(C_{Y_+}-c_X\right)}{\left(c_X-C_{Y_+}\right)^2}+\\ &-\frac{\pi Y_-(C_{Y_-}c_X-1)-S_{Y_-}\left(C_{Y_-}-c_X\right)}{\left(c_X-C_{Y_-}\right)^2}\Bigg]\end{aligned} \tag{57}$$

where we used the following notation:

$$\begin{aligned}&X = x/L, && Y = y/L,\\ &Y_+ = \frac{y+h}{L}, && Y_- = \frac{y-h}{L},\\ &C_{Y_\pm} = \cosh(2\pi Y_\pm), && S_{Y_\pm} = \sinh(2\pi Y_\pm),\\ &C_{2Y_\pm} = \cosh(4\pi Y_\pm), && S_{2Y_\pm} = \sinh(4\pi Y_\pm),\\ &c_X = \cos(2\pi X), && s_X = \sin(2\pi X)\end{aligned} \tag{58}$$

The term B in equation (55) is the Head correction for the presence of the free surface, σ^{H}_{xx}, and we have to find its sum:

$$\sigma^{H\text{-}xPBC}_{xx}(x,y;L) = \sum_{n=-\infty}^{+\infty} \sigma^{H}_{xx}(x-nL,y) \tag{59}$$

The sum (59) can be exactly evaluated:

$$\begin{aligned}\sigma^{H\text{-}xPBC}_{xx} &= \sum_{n=-\infty}^{+\infty} 2h\frac{(y+h)(y-h)^3-6y(y-h)(x-nL)^2+(x-nL)^4}{[(x-nL)^2+(y-h)^2]^3} =\\ &= \sum_{n=-\infty}^{+\infty} 2h\frac{(y+h)(y-h)^3}{[(x-nL)^2+(y-h)^2]^3} - 12hy(y-h)\frac{(x-nL)^2}{[(x-nL)^2+(y-h)^2]^3}\\ &\quad +2h\frac{(x-nL)^4}{[(x-nL)^2+(y-h)^2]^3}\end{aligned} \tag{60}$$

The evaluation of the three addenda in Eq. (60), exploits the known mathematical results (see e.g. [54]):

$$\sum_{n=-\infty}^{+\infty} \frac{n+p}{(n+p)^2+q^2} = \frac{\pi \sin(2\pi p)}{\cosh(2\pi q)-\cos(2\pi p)} \tag{61}$$

$$\sum_{n=-\infty}^{+\infty} \frac{1}{(n+p)^2+q^2} = \frac{\pi}{q}\frac{\sinh(2\pi q)}{\cosh(2\pi q)-\cos(2\pi p)} \tag{62}$$

and:

$$\sum_{n=-\infty}^{+\infty} \frac{n+p}{[(n+p)^2+q^2]^2} = \frac{\pi^2}{q}\frac{\sinh(2\pi q)\sin(2\pi p)}{[\cosh(2\pi q)-\cos(2\pi p)]^2} \tag{63}$$

Indeed, the first term in Eq. (60) reads:

$$\begin{aligned}\sum_{n=-\infty}^{+\infty} 2h\frac{(y+h)(y-h)^3}{[(x-nL)^2+(y-h)^2]^3} &= 2h\frac{(y+h)(y-h)^3}{L^6}\sum_{n=-\infty}^{+\infty}\frac{1}{[(n-\frac{x}{L})^2+(\frac{y-h}{L})^2]^3} \\ &= 2h\frac{(y+h)(y-h)^3}{L^6}\sum_{n=-\infty}^{+\infty}\frac{1}{[(n+p)^2+q^2]^3}\end{aligned}$$

with the substitution $p = -\frac{x}{L}$, and $q = \frac{y-h}{L}$. This sum can be evaluated starting from Eq. (62) and considering the following identity:

$$\begin{aligned}\sum_{n=-\infty}^{+\infty}\frac{1}{[(n+p)^2+q^2]^3} &= -\frac{1}{4q}\frac{\partial}{\partial q}\left\{-\frac{1}{2q}\frac{\partial}{\partial q}\left\{\sum_{n=-\infty}^{+\infty}\frac{1}{[(n+p)^2+q^2]}\right\}\right\} \\ &= -\frac{1}{4q}\frac{\partial}{\partial q}\left\{-\frac{1}{2q}\frac{\partial}{\partial q}\left\{\frac{\pi}{q}\frac{\sinh(2\pi q)}{\cosh(2\pi q)-\cos(2\pi p)}\right\}\right\}\end{aligned} \tag{64}$$

Substituting back the values for $p = -\frac{x}{L}$ and $q = \frac{y-h}{L}$ in this expression we obtain the result for this series.

The second addendum in Eq. (60) is:

$$\begin{aligned}&\sum_{n=-\infty}^{+\infty} -12hy\frac{(y-h)(x-nL)^2}{[(x-nL)^2+(y-h)^2]^3} = \\ &\quad = -\frac{12hy(y-h)}{L^4}\sum_{n=-\infty}^{+\infty}\frac{(n+p)^2}{[(n+p)^2+q^2]^3}\end{aligned} \tag{65}$$

The sum in equation (65) can be evaluated starting again from Eq. (62) and exploiting the identity:

$$\begin{aligned}\sum_{n=-\infty}^{+\infty}\frac{(n+p)^2}{[(n+p)^2+q^2]^3} = \sum_{n=-\infty}^{+\infty} -\frac{1}{4}\left\{\frac{\partial}{\partial p}\left\{-\frac{1}{2}\frac{\partial}{\partial p}\left[\frac{1}{(n+p)^2+q^2}\right]\right\}+\right. \\ \left.+\frac{1}{2q}\frac{\partial}{\partial q}\left[\frac{1}{(n+p)^2+q^2}\right]\right\}\end{aligned} \tag{66}$$

Exploiting the known series reported in Eq. (62), Eq. (66) yields:

$$\begin{aligned}\sum_{n=-\infty}^{+\infty} &-\frac{1}{4}\left\{\frac{\partial}{\partial p}\left\{-\frac{1}{2}\frac{\partial}{\partial p}\left[\frac{1}{(n+p)^2+q^2}\right]\right\}+\frac{1}{2q}\frac{\partial}{\partial q}\left[\frac{1}{(n+p)^2+q^2}\right]\right\}= \\ &=-\frac{1}{4}\left\{\frac{\partial}{\partial p}\left\{-\frac{1}{2}\frac{\partial}{\partial p}\left[\frac{\pi}{q}\frac{\sinh(2\pi q)}{\cosh(2\pi q)-\cos(2\pi p)}\right]\right\}+\right. \\ &\left.+\frac{1}{2q}\frac{\partial}{\partial q}\left[\frac{\pi}{q}\frac{\sinh(2\pi q)}{\cosh(2\pi q)-\cos(2\pi p)}\right]\right\}\end{aligned} \tag{67}$$

Finally, the third term in the expression of σ_{xx}^{H} is:

$$\sum_{n=-\infty}^{+\infty}+2h\frac{(x-nL)^4}{[(x-nL)^2+(y-h)^2]^3}=\frac{2h}{L^2}\sum_{n=-\infty}^{+\infty}\frac{(n+p)^4}{[(n+p)^2+q^2]^3}$$

which can be evaluated exploiting the identity:

$$\begin{aligned}\sum_{n=-\infty}^{+\infty}\frac{(n+p)^4}{[(n+p)^2+q^2]^3}=\sum_{n=-\infty}^{+\infty}\frac{3}{2}&\left\{\frac{\partial}{\partial p}\left\{\frac{1}{6}\left\{q^2\frac{n+p}{[(n+p)^2+q^2]^2}-\frac{n+p}{(n+p)^2+q^2}\right\}\right\}+\right. \\ &\left.-\frac{1}{4}\left\{\frac{\partial}{\partial p}\left[\frac{n+p}{(n+p)^2+q^2}\right]-\frac{1}{(n+p)^2+q^2}\right\}\right\}\end{aligned}$$

This term can be summed using again the results from the series in Eq. (61), (62) and (63).

A.2.2 Contributions from b_y

Now we can come back to equation (55) and consider the terms dependent on the b_y component of the Burgers vector. The two addenda in C again correspond to the dipole construction and the sum of this two terms is known and reported in [54], yielding (using the notation reported in Eq. (58)):

$$\sigma_{xx}^{D\text{-}xPBC}(x,y;L)=\frac{\mu b_y s_X}{2(1-\nu)L}\left[\frac{C_{Y_+}-c_X-2\pi Y_+ S_{Y_+}}{(c_X-C_{Y_+})^2}-\frac{C_{Y_-}-c_X-2\pi Y_- S_{Y_-}}{(c_X-C_{Y_-})^2}\right]$$

Finally, the term D is the contribution to the Head correction for the σ_{xx} stress field arising from the b_y component of the Burgers vector. To evaluate its expression we have to compute a sum like that in Eq. (59):

$$\begin{aligned}\sigma_{xx}^{H\text{-}xPBC}&=\sum_{n=-\infty}^{+\infty}-\frac{4h(x-nL)\left[(x-nL)^2(2h-3y)+(y-h)^2(2h+y)\right]}{\left[(x-nL)^2+(y-h)^2\right]^3} \\ &=-4h(2h-3y)\sum_{n=-\infty}^{+\infty}\frac{(x-nL)^3}{\left[(x-nL)^2+(y-h)^2\right]^3}+ \\ &\quad-4h(y-h)^2(2h+y)\sum_{n=-\infty}^{+\infty}\frac{(x-nL)}{\left[(x-nL)^2+(y-h)^2\right]^3}\end{aligned} \tag{68}$$

the first series in Eq. (68) can be rewritten using again the substitution $p = -\frac{x}{L}$ and $q = \frac{y-h}{L}$, and summed exploiting the identity:

$$\begin{aligned}\sum_{n=-\infty}^{+\infty} \frac{(n+p)^3}{\left[(n+p)^2+q^2\right]^3} &= -\frac{1}{4}\left\{\frac{\partial}{\partial p}\left\{-\frac{1}{2}\left\{\frac{\partial}{\partial p}\left[\frac{(n+p)}{(n+p)^2+q^2}\right] - \frac{1}{(n+p)^2+q^2}\right\}\right\}+\right. \\ &\left. -2\frac{n+p}{[(n+p)^2+q^2]^2}\right\} \\ &= -\frac{1}{4}\left\{\frac{\partial}{\partial p}\left\{-\frac{1}{2}\left\{\frac{\partial}{\partial p}\left[\frac{\pi \sin(2\pi p)}{\cosh(2\pi q)-\cos(2\pi p)}\right] + \right.\right.\right. \\ &\left.\left.\left. -\frac{\pi}{q}\frac{\sinh(2\pi q)}{\cosh(2\pi q)-\cos(2\pi p)}\right\}\right\} - 2\frac{\pi^2 \sinh(2\pi q)\sin(2\pi p)}{q(\cosh(2\pi q)-\cos(2\pi p))^2}\right\}\end{aligned}$$

where we have exploited the results from the series (61), (62) and (63).

The second sum in Eq. (68) can be evaluated, using the same notation, exploiting the identity:

$$\begin{aligned}\sum_{n=-\infty}^{+\infty} \frac{(n+p)}{\left[(n+p)^2+q^2\right]^3} &= \sum_{n=-\infty}^{+\infty} \frac{1}{4}\frac{\partial}{\partial p}\left\{\frac{1}{2q}\frac{\partial}{\partial q}\left[\frac{1}{(n+p)^2+q^2}\right]\right\} \\ &= \frac{1}{4}\frac{\partial}{\partial p}\left\{\frac{1}{2q}\frac{\partial}{\partial q}\left[\frac{\pi}{q}\frac{\sinh(2\pi q)}{\cosh(2\pi q)-\cos(2\pi p)}\right]\right\}\end{aligned}$$

This result can be obtained by series (62). Again, substituting back the values for p and q we can obtain the final result for the sum in equation (68).

A.3 STRESS FIELD CONVERGENCE

In order to check the expressions obtained, we can compare the analytical expressions with numerical calculations of the series as reported in Eq. 59. At the same time, we also check that the summed expressions do verify the condition of zero normal stress at the free surface $\sigma \cdot \mathbf{n} = 0$. In figure 60 the convergence of stress fields at the free surface for the only two non-zero stress components, that, as expected, are σ_{xx} and σ_{xz} is reported.

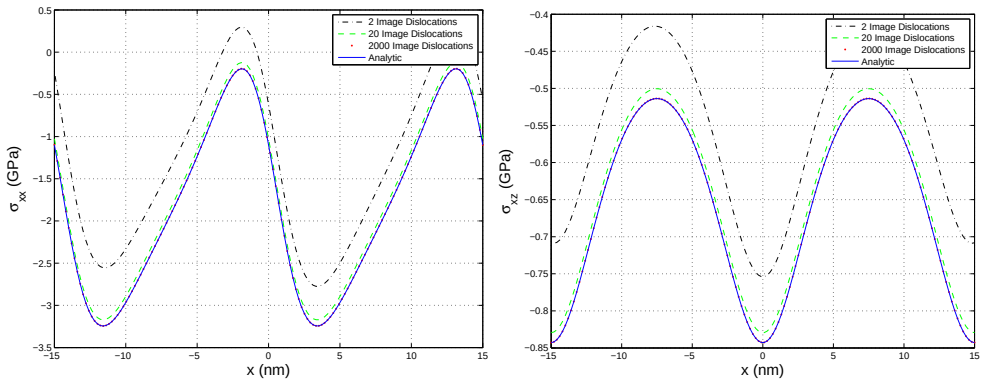

Figure 60: Plot of the only two non-zero components of the stress functions at the free surface. The solid blue lines represent the analytic solution found as sum of an infinite number of dislocations, the other lines show the convergence with an increasing number of image dislocations.

A.4 NON-SINGULAR STRESS FUNCTIONS

Once the problem of finding the periodic stress field is solved, it is necessary to remove the numerical divergence at dislocations cores, e.g. to numerically intea-grate the elastic energy in a heteroepitaxial system. Notice that the only divergent contribution in the integration domain is the bulk one, so this is the only one that requires the correction of its divergence.

The solution for a periodic array of bulk dislocations is known and for example the yz stress component is:

$$\sigma_{yz}^{x\text{-PBC}} = \frac{\mu b_z}{2\pi} \frac{\sin\left(2\pi\frac{x}{L}\right)}{\cosh\left(2\pi\frac{y}{L}\right) - \cos\left(2\pi\frac{x}{L}\right)} \tag{69}$$

This can be regularized starting by the procedure proposed by Wei Cai et al. in [69] for a single dislocation, i.e. by considering the non-divergent expression:

$$\sigma_{yz} = \frac{\mu b_z}{2\pi} \frac{x(x^2+y^2+2t^2)}{(x^2+y^2+t^2)^2}$$

with $t > 0$ representing a typical core dimension ($1-2$ Å).

Starting from this expression we want to find the sum:

$$\sum_{n=-\infty}^{\infty} \frac{\mu b_z}{2\pi} \frac{(x-nL)[(x-nL)^2+y^2+2t^2]}{[(x-nL)^2+y^2+t^2]^2}$$

$$\sum_{n=-\infty}^{\infty} \frac{\mu b_z}{2\pi} \Bigg[\underbrace{\frac{(x-nL)\cancel{[(x-nL)^2+y^2+t^2]}}{\cancel{[(x-nL)^2+y^2+t^2]^2}}}_{\text{I}} + \underbrace{t^2 \frac{(x-nL)}{[(x-nL)^2+y^2+t^2]^2}}_{\text{II}} \Bigg]$$

I yields:

$$\sum_{n=-\infty}^{\infty} -\frac{1}{L} \frac{(n-\frac{x}{L})}{\left[(n-\frac{x}{L})^2+\frac{y^2+t^2}{L^2}\right]^2} = \sum_{n=-\infty}^{\infty} -\frac{1}{L} \frac{n+p}{\left[(n+p)^2+q^2\right]^2}$$

This series again can be summed exactly, yielding:

$$-\frac{1}{L} \frac{\pi \sin(2\pi p)}{\cosh(2\pi q)\cos(2\pi p)} = \frac{1}{L} \frac{\pi \sin\left(2\pi\frac{x}{L}\right)}{\cosh\left(2\pi\sqrt{\frac{y^2+t^2}{L^2}}\right) - \cos\left(2\pi\frac{x}{L}\right)}$$

The second term (II) is:

$$\sum_{n=-\infty}^{\infty} t^2 \frac{(x-nL)}{[(x-nL)^2+y^2+t^2]^2} = \sum_{n=-\infty}^{\infty} -\frac{t^2}{L^3} \frac{(n+p)}{\left[(n+p)^2+q^2\right]^2}$$

And from [54] eq. 19-74 the result of this sum is:

$$-\frac{t^2}{L^3} \frac{\pi^2 \sinh(2\pi q)\sin(2\pi p)}{q(\cosh(2\pi q)-\cos(2\pi p))^2} = \frac{t^2}{L^3} \frac{\pi^2 \sinh\left(2\pi\sqrt{\frac{y^2+t^2}{L^2}}\right)\sin\left(2\pi\frac{x}{L}\right)}{\sqrt{\frac{y^2+t^2}{L^2}}\left[\cosh\left(2\pi\sqrt{\frac{y^2+t^2}{L^2}}\right) - \cos\left(2\pi\frac{x}{L}\right)\right]^2}$$

So, putting all terms together we find:

$$\sigma_{yz} = \frac{\mu b_z}{2L} \sin\left(2\pi\frac{x}{L}\right) \Bigg[\frac{1}{\cosh\left(2\pi\sqrt{\frac{y^2+t^2}{L^2}}\right) - \cos\left(2\pi\frac{x}{L}\right)} + \frac{t^2}{L} \frac{\pi \sinh\left(2\pi\sqrt{\frac{y^2+t^2}{L^2}}\right)\sin\left(2\pi\frac{x}{L}\right)}{\sqrt{y^2+t^2}\left[\cosh\left(2\pi\sqrt{\frac{y^2+t^2}{L^2}}\right) - \cos\left(2\pi\frac{x}{L}\right)\right]^2} \Bigg]$$

All other stress functions can be regularized in a similar way. Using the notation $Y_t = \sqrt{\frac{y^2+t^2}{L^2}}$ and $X = \frac{x}{L}$:

$$\begin{aligned}
\sigma_{xx} =& -\frac{\mu b_x}{2L}\left[\frac{3y\pi}{LY_t}\frac{\sinh(2\pi Y_t)}{\left[\cosh(2\pi Y_t)-\cos(2\pi X)\right]}\right.\\
&\left.-\frac{2y^3}{4L^3Y_t^3}\frac{-4\pi Y_t+2\cos(2\pi X)\left[2\pi Y_t\cosh(2\pi Y_t)-\sinh(2\pi Y_t)\right]+\sinh(4\pi Y_t)}{\left[\cosh(2\pi Y_t)-\cos(2\pi X)\right]^2}\right]\\
&+\frac{\mu b_y}{2(1-\nu)L}\sin(2\pi X)\left[\frac{\cosh(2\pi Y_t)-\cos(2\pi X)+\frac{2\pi y^2}{L^2Y_t}\sinh(2\pi Y_t)}{\left[\cosh(2\pi Y_t)-\cos(2\pi X)\right]^2}\right]\\
\sigma_{yy} =& -\frac{\mu b_x \pi y}{(1-\nu)L^2}\frac{\cosh(2\pi Y_t)\cos(2\pi X)-1}{\left[\cosh(2\pi Y_t)-\cos(2\pi X)\right]^2}\\
&+\frac{\mu b_y}{2(1-\nu)L}\sin(2\pi X)\left[\frac{\cosh(2\pi Y_t)-\cos(2\pi X)+2\pi Y_t\sinh(2\pi Y_t)}{\left[\cosh(2\pi Y_t)-\cos(2\pi X)\right]^2}\right]\\
\sigma_{xy} =& \frac{b_x\mu}{2L^3(1-\nu)}\sin(2\pi X)\left[\frac{2\pi t^2\sinh(2\pi Y_t)}{Y_t\left[\cosh(2\pi Y_t)-\cos(2\pi X)\right]^2}\right.\\
&\left.+\frac{L^2\left(\cosh(2\pi Y_t)-\cos(2\pi X)-2\pi Y_t\sinh(2\pi Y_t)\right)}{\left[\cosh(2\pi Y_t)-\cos(2\pi X)\right]^2}\right]\\
&-\frac{\mu b_y \pi y}{2(1-\nu)L^2}\frac{\cosh(2\pi Y_t)\cos(2\pi X)-1}{\left[\cosh(2\pi Y_t)-\cos(2\pi X)\right]^2}\\
\sigma_{xz} =& -\frac{\mu b_z}{2L}\left[\frac{y}{LY_t}\frac{\sinh(2\pi Y_t)}{\left[\cosh(2\pi Y_t)-\cos(2\pi X)\right]}\right.\\
&\left.+\frac{yt^2}{4L^3Y_t^3}\frac{-4\pi Y_t+2\cos(2\pi X)\left(2\pi Y_t\cosh(2\pi Y_t)-\sinh(2\pi Y_t)\right)+\sinh(4\pi Y_t)}{\left[\cosh(2\pi Y_t)-\cos(2\pi X)\right]^2}\right]\\
\sigma_{yz} =& \frac{\mu b_z}{2L}\sin(2\pi X)\left[\frac{\cosh(2\pi Y_t)-\cos(2\pi X)+\frac{\pi t^2}{L^2Y_t}\sinh(2\pi Y_t)}{\left[\cosh(2\pi Y_t)-\cos(2\pi X)\right]^2}\right]
\end{aligned}$$

LIST OF PUBBLICATIONS

- **F. Rovaris**, R. Bergamaschini and F. Montalenti, "Modeling the Competition between elastic and plastic relaxation in semiconductor heteroepitaxy: from cyclic growth to flat films", *Phys. Rev. B* **94**, 205304 (2016)
- **F. Rovaris**, F. Isa, R. Gatti, A. Jung, G. Isella, F. Montalenti and H. Von Känel, "Three-dimensional SiGe/Si Heterostructures: Switching the dislocation sign by substrate under-etching", *Phys. Rev. Mat.* **1**, 073602 (2017)
- F. Montalenti, **F. Rovaris**, R. Bergamaschini, L. Miglio, M. Salvalaglio, G. Isella, F. Isa, H. Von Kaenel, "Dislocation-Free SiGe/Si Heterostructures", *Crystals* **8**, 257 (2018)
- **F. Rovaris**, M. Zoellner, P. Zamsueil, M. Schubert, A. Marzegalli, L. De Gaspare, M. De Seta, T. Schroeder, P. Storck, G. Schwalb, C. Richter, T. Schülli, G. Capellini and F. Montalenti, "Misfit-Dislocation Distributions in Heteroepitaxy: From mesoscale measurements to individual defects and back", *Phys. Rev. Appl.* **10**, 054067 (2019)
- **F. Rovaris**, M. Zoellner, P. Zamsueil, A. Marzegalli, L. De Gaspare, M. De Seta, T. Schroeder, P. Storck, G. Schwalb, G. Capellini and F. Montalenti, "Dynamics of crosshatch patterns in heteroepitaxy", *Phys. Rev. B.* **100**, 085307 (2019)
- L. Becker, **F. Rovaris**, *et. al*, "Approaching Matthews and Blakeslee conditions in heteroepitaxy: Relaxation of low-misfit GexSi1-x/Si(001) layers" *in preparation* (2019)
- F. Boccardo, **F. Rovaris**, F. Montalenti and O. Pierre-Luis, *In preparation* (2019)

CONTRIBUTED TALKS

- F. Rovaris, R. Bergamaschini and F. Montalenti, "Modeling the competition between elastic and plastic relaxation: From cyclic growth to flat films", in GDRi Mecano General Meeting, Toulouse (France), 10-12 May 2017.
- F. Rovaris, M. Zoellner, G. Chahine, P. Zamsueil, P. Storck, M. Haeberlen, A. Marzegalli, T. Schroeder, G. Capellini and F. Montalenti, "Misfit relaxation in heteroepitaxy: A theoretical model for inferring individual dislocation positions from tilting angle maps", in EMRS Fall 2017, Warsaw (Poland), 2017.

- F. Rovaris, M. Zoellner, P. Zamsueil, A. Marzegalli, L. De Gaspare, M. De Seta, T. Schroeder, P. Storck, G. Schwalb, G. Capellini and F. Montalenti, "Dynamics of cross-hatch evolution in heteroepitaxy", in EMRS Fall 2018, Warsaw (Poland), 2018.
- F. Rovaris and R. Gatti, "Multi-Scale Modeling of Plasticity: a coupling between Dislocation Dynamics and FEniCS", in FEniCS'18, Oxford (United Kingdom), 21-23 march 2018.
- F. Rovaris, F. Isa, R. Gatti, A. Jung, G. Isella, F. Montalenti and H. Von Kaenel, "SiGe/Si Vertical Heterostructures: Switching the Dislocation Sign by Substrate Under-Etching" in 1st Joint ISTDM/ICSI 2018 Meeting, Potsdam (Germany).
- F. Rovaris, M. Zoellner, P. Zamsueil, A. Marzegalli, L. De Gaspare, M. De Seta, T. Schroeder, P. Storck, G. Schwalb, G. Capellini and F. Montalenti, "Dynamics of crosshatch patterns in heteroepitaxy" in 2nd Joint ISTDM/ICSI 2019 Meeting, Madison (Wisconsin), (2019)

AWARDS

- Best Paper Award for the paper entitled "SiGe/Si Vertical Heterostructures: Switching the Dislocation Sign by Substrate Under-Etching" in 1st Joint ISTDM/ICSI 2018 Meeting, Potsdam (Germany), 2018.

BIBLIOGRAPHY

[1] I. Ferain, C. A. Colinge, and J. P. Colinge, "Multigate transistors as the future of classical metal-oxide-semiconductor field-effect transistors," *Nature*, vol. 479, no. 7373, pp. 310–316, 2011.

[2] C. Y. Chi, C. C. Chang, S. Hu, T. W. Yeh, S. B. Cronin, and P. D. Dapkus, "Twin-free GaAs nanosheets by selective area growth: Implications for defect-free nanostructures," *Nano Letters*, vol. 13, no. 6, pp. 2506–2515, 2013.

[3] T. Vasen, P. Ramvall, A. Afzalian, G. Doornbos, M. Holland, C. Thelander, K. A. Dick, L. E. Wernersson, and M. Passlack, "Vertical Gate-All-Around Nanowire GaSb-InAs Core-Shell n-Type Tunnel FETs," *Scientific Reports*, vol. 9, no. 1, pp. 1–9, 2019.

[4] S. Takagi, S.-H. Kim, M. Yokoyama, R. Zhang, N. Taoka, Y. Urabe, T. Yasuda, H. Yamada, O. Ichikawa, N. Fukuhara, M. Hata, and M. Takenaka, "High mobility CMOS technologies using III–V/Ge channels on Si platform," *Solid-State Electronics*, vol. 88, pp. 2–8, 2013.

[5] T. E. Kazior, "Beyond Cmos: Heterogeneous integration of III-V devices, RF MEMS and other dissimilar materials/devices with Si CMOS to create intelligent microsystems," *Philosophical Transactions of the Royal Society A: Mathematical, Physical and Engineering Sciences*, vol. 372, no. 2012, pp. 20130105–20130105, 2014.

[6] E. Fitzgerald, "Dislocations in strained-layer epitaxy: theory, experiment, and applications," *Materials Science Reports*, vol. 7, no. 3, pp. 87–142, 1991.

[7] "International Technology Roadmap for Semiconductors." http://www.itrs.net/.

[8] D. J. Paul, "Silicon-germanium strained layer materials in microelectronics," *Advanced Materials*, vol. 11, no. 3, pp. 191–204, 1999.

[9] E. C. Garnett, M. L. Brongersma, Y. Cui, and M. D. McGehee, "Nanowire solar cells," *Annual Review of Materials Research*, vol. 41, no. 1, pp. 269–295, 2011.

[10] I. Prieto, B. Galiana, P. A. Postigo, C. Algora, L. J. Martínez, and I. Rey-Stolle, "Enhanced quantum efficiency of ge solar cells by a two-dimensional photonic crystal nanostructured surface," *Applied Physics Letters*, vol. 94, no. 19, p. 191102, 2009.

[11] J. Michel, J. Liu, and L. C. Kimerling, "High-performance ge-on-si photodetectors," *Nature Photonics*, vol. 4, no. 8, pp. 527–534, 2010.

[12] M. S. Alnæs, J. Blechta, J. Hake, A. Johansson, B. Kehlet, A. Logg, C. Richardson, J. Ring, M. E. Rognes, and G. N. Wells, "The fenics project version 1.5," *Archive of Numerical Software*, vol. 3, no. 100, 2015.

[13] A. Logg, K.-A. Mardal, G. N. Wells, *et al.*, *Automated Solution of Differential Equations by the Finite Element Method*. Springer, 2012.

[14] A. K. Tripathi and O. Pierre-Louis, "Triple-line kinetics for solid films," *Phys. Rev. E*, vol. 97, p. 022801, Feb 2018.

[15] O. Jamond, R. Gatti, A. Roos, and B. Devincre, "Consistent formulation for the discrete-continuous model: Improving complex dislocation dynamics simulations," *International Journal of Plasticity*, vol. 80, pp. 19 – 37, 2016.

[16] C. V. Falub, H. von Kaenel, F. Isa, R. Bergamaschini, A. Marzegalli, D. Chrastina, G. Isella, E. Muller, P. Niedermann, and L. Miglio, "Scaling Hetero-Epitaxy from Layers to Three-Dimensional Crystals," *Science*, vol. 335, p. 1330Ð1334, 2012.

[17] J. P. Douglas, "Si/sige heterostructures: from material and physics to devices and circuits," *Semiconductor Science and Technology*, vol. 19, no. 10, p. R75, 2004.

[18] J. Stangl, V. Holý, and G. Bauer, "Structural properties of self-organized semiconductor nanostructures," *Reviews of Modern Physics*, vol. 76, pp. 725–783, Sep 2004.

[19] P. K. Bhattacharya, U. Das, F. Juang, Y. Nashimoto, and S. Dhar, "Material properties and optical guiding in ingaas-gaas strained layer superlattices—a brief review," *Solid-State Electronics*, vol. 29, no. 2, pp. 261 – 267, 1986.

[20] S. Naritsuka, T. Nishinaga, M. Tachikawa, and H. Mori, "InP layer grown on (001) silicon substrate by epitaxial lateral overgrowth," *Japanese Journal of Applied Physics*, vol. 34, no. Part 2, No. 11A, pp. L1432–L1435, 1995.

[21] G. Medeiros-Ribeiro, A. M. Bratkovski, T. I. Kamins, D. A. A. Ohlberg, and R. S. Williams, "Shape transition of germanium nanocrystals on a silicon (001) surface from pyramids to domes," *Science*, vol. 279, no. 5349, pp. 353–355, 1998.

[22] F. Montalenti, P. Raiteri, D. Migas, H. von Känel, A. Rastelli, C. Manzano, G. Costantini, U. Denker, O. Schmidt, K. Kern, and L. Miglio, "Atomic-scale pathway of the pyramid-to-dome transition during ge growth on si(001)," *Physical Review Letters*, vol. 93, p. 216102, 2004.

[23] M. Hammar, F. LeGoues, J. Tersoff, M. Reuter, and R. Tromp, "In situ ultrahigh vacuum transmission electron microscopy studies of hetero-epitaxial growth i. si(001)ge," *Surface Science*, vol. 349, no. 2, pp. 129–144, 1996.

[24] F. Ross, J. Tersoff, M. Reuter, F. Legoues, and R. Tromp, "In situ transmission electron microscopy observations of the formation of self-assembled ge islands on si," *Microscopy Research and Technique*, vol. 42, no. 4, pp. 281–294, 1998.

[25] J. Tersoff and R. M. Tromp, "Shape transition in growth of strained islands: Spontaneous formation of quantum wires," *Physical Review Letters*, vol. 70, pp. 2782–2785, 1993.

[26] R. B. Hetnarsky and J. Ignaczak, *The Mathematical Theory of Elasticity*. CRC Press, 2011.

[27] L. D. Landau and E. M. Lifshitz, *Theory of Elasticity*, vol. 7 of *Course of Theoretical Physics*. Elsevier, 3 ed., 1986.

[28] T. Mura, *Micromechanics of Defects in Solids*. Mechanics of Elastic and Inelastic Solids, Springer Netherlands, 1987.

[29] B. P. Uberuaga, M. Leskovar, A. P. Smith, H. Jónsson, and M. Olmstead, "Diffusion of ge below the si(100) surface: Theory and experiment," *Phys. Rev. Lett.*, vol. 84, pp. 2441–2444, 2000.

[30] R. Asaro and W. Tiller, "Interface morphology development during stress corrosion cracking: Part i. via surface diffusion," *Metallurgical Transactions*, vol. 3, no. 7, pp. 1789–1796, 1972.

[31] M. Grinfeld, "The stress driven instability in elastic crystals: Mathematical models and physical manifestations," *Journal of Nonlinear Science*, vol. 3, no. 1, pp. 35–83, 1993.

[32] D. Srolovitz, "On the stability of surfaces of stressed solids," *Acta Metallurgica*, vol. 37, no. 2, pp. 621–625, 1989.

[33] A. A. Stekolnikov, J. Furthmüller, and F. Bechstedt, "Absolute surface energies of group-iv semiconductors: Dependence on orientation and reconstruction," *Physical Review B*, vol. 65, p. 115318, Feb 2002.

[34] M. J. Beck, A. van de Walle, and M. Asta, "Surface energetics and structure of the ge wetting layer on si(100)," *Physical Review B*, vol. 70, p. 205337, Nov 2004.

[35] P. Müller and J. Métois, "Anisotropy of the surface thermodynamic properties of silicon," *Thin Solid Films*, vol. 517, no. 1, pp. 65–68, 2008. Fifth International Conference on Silicon Epitaxy and Heterostructures (ICSI-5).

[36] L. Onsager, "Reciprocal relations in irreversible processes. i.," *Physical Review*, vol. 37, pp. 405–426, Feb 1931.

[37] L. Onsager, "Reciprocal relations in irreversible processes. ii.," *Physical Review*, vol. 38, pp. 2265–2279, Dec 1931.

[38] M. Grinfeld, "Instability of the separation boundary between a non-hydrostatically stressed elastic body and a melt," *Soviet Physics Doklady*, vol. 31, pp. 831–834, 1986.

[39] K. Kassner and C. Misbah, "Non-Linear Evolution of a Uniaxially Stressed Solid: A Route to Fracture?," *Europhysics Letters*, vol. 28, no. 4, pp. 245–250, 1994.

[40] Y.-W. Zhang and A. F. Bower, "Three dimensional simulations of island formation in a coherent strained epitaxial film," *Thin Solid Films*, vol. 357, pp. 8–12, 1999.

[41] W. H. Yang and D. Srolovitz, "Cracklike Surface Instabilities in Stressed Solids," *Physical Review Letters*, vol. 71, no. 10, pp. 1593–1596, 1993.

[42] W. H. Yang and D. J. Srolovitz, "Surface morphology evolution in stressed solids: surface diffusion controlled crack initiation," *Journal of Mechanics and Physics of Solids*, vol. 42, no. 10, p. 1551, 1994.

[43] L. Freund and F. Jonsdottir, "Instability of a biaxially stressed thin film on a substrate due to material diffusion over its free surface," *Journal of the Mechanics and Physics of Solids*, vol. 41, no. 7, pp. 1245–1264, 1993.

[44] H. Gao and W. D. Nix, "Surface Roughening of Heteroepitaxial Thin Films," *Annual Review of Materials Science*, vol. 29, no. 1, pp. 173–209, 1999.

[45] Y. Pang and R. Huang, "Nonlinear effect of stress and wetting on surface evolution of epitaxial thin films," *Physical Review B*, vol. 74, p. 075413, Aug 2006.

[46] J.-N. Aqua, T. Frisch, and A. Verga, "Nonlinear evolution of a morphological instability in a strained epitaxial film," *Physical Review B*, vol. 76, p. 165319, Oct 2007.

[47] C.-H. Chiu and H. Gao, "A Numerical Study of Stress Controlled Surface Diffusion During Epitaxial Film Growth," *Mater. Res. Soc. Symp. Proc.*, vol. 356, p. 33, 1995.

[48] G.-H. Lu and F. Liu, "Towards quantitative understanding of formation and stability of Ge hut islands on Si(001)," *Physical Review Letter*, vol. 94, p. 176103, 2005.

[49] J. Ye and C. V. Thompson, "Mechanisms of complex morphological evolution during solid-state dewetting of single-crystal nickel thin films," *Applied Physics Letters*, vol. 97, no. 7, p. 071904, 2010.

[50] A. Herz, A. Franz, F. Theska, M. Hentschel, T. Kups, D. Wang, and P. Schaaf, "Solid-state dewetting of single- and bilayer au-w thin films: Unraveling the role of individual layer thickness, stacking sequence and oxidation on morphology evolution," *AIP Advances*, vol. 6, no. 3, p. 035109, 2016.

[51] E. Jiran and C. Thompson, "Capillary instabilities in thin films," *Journal of Electronic Materials*, vol. 19, no. 11, pp. 1153–1160, 1990.

[52] M. De Seta, G. Capellini, F. Evangelisti, and C. Spinella, "Intermixing-promoted scaling of ge/si(100) island sizes," *Journal Of Applied Physics*, vol. 92, no. 1, pp. 614–619, 2002.

[53] M. Stoffel, A. Rastelli, J. Tersoff, T. Merdzhanova, and O. G. Schmidt, "Local equilibrium and global relaxation of strained SiGe/Si(001) layers," *Physical Review B*, vol. 74, pp. 155326–155330, 2006.

[54] J. P. Hirth and J. Lothe, *Theory of Dislocations*. Krieger Publishing Company, 2 ed., 1982.

[55] A. K. Head, "Edge dislocations in inhomogeneous media," in *Proceedings of the Physical Society, Section B*, vol. 66, 1953.

[56] A. Sakai, N. Taoka, O. Nakatsuka, S. Zaima, and Y. Yasuda, "Pure-edge dislocation network for strain-relaxed SiGe/Si(001) systems," *Appl. Phys. Lett.*, vol. 86, no. 22, p. 221916, 2005.

[57] J. Friedel, *Dislocations*. Pergamon Press, 1967.

[58] J. Godet, S. Brochard, L. Pizzagalli, P. Beauchamp, and J. M. Soler, "Dislocation formation from a surface step in semiconductors: An ab–initio study," *Phys. Rev. B*, vol. 73, p. 092105, 2006.

[59] J. Matthews and A. Blakeslee, "Defects in epitaxial multilayers: I. Misfit dislocations," *Journal of Crystal Growth*, vol. 27, pp. 118–125, 1974.

[60] J. Matthews and A. Blakeslee, "Defects in epitaxial multilayers: II. Dislocation pile-ups, threading dislocations, slip lines and cracks," *Journal of Crystal Growth*, vol. 29, no. 3, pp. 273–280, 1975.

[61] F. K. LeGoues, J. A. Ott, K. Eberl, and S. S. Iyer, "In situ study of relaxation of sige thin films by the modified frank–read mechanism," *Applied Physics Letter*, vol. 61, no. 2, pp. 174–176, 1992.

[62] F. K. LeGoues, B. S. Meyerson, and J. F. Morar, "Anomalous strain relaxation in Sige/Si thin films and heterostructures," *Physical Review Letters*, vol. 66, no. 22, pp. 2903–2906, 1991.

[63] K. W. Schwarz, "Simulation of dislocations on the mesoscopic scale. I. Methods and examples," *Journal of Applied Physics*, vol. 85, no. 1, pp. 108–119, 1999.

[64] S. Ryu, K. Kang, and W. Cai, "Entropic effect on the rate of dislocation nucleation.," *Proceedings of the National Academy of Sciences of the United States of America*, vol. 108, no. 13, pp. 5174–8, 2011.

[65] J. Tersoff, "Dislocations and strain relief in compositionally graded layers," *Applied Physics Letters*, vol. 62, no. 7, pp. 693–695, 1993.

[66] D. Gómez-García, B. Devincre, and L. P. Kubin, "Dislocation patterns and the similitude principle: 2.5D mesoscale simulations," *Physical Review Letters*, vol. 96, pp. 8–11, 2006.

[67] L. P. Kubin, *Dislocations, Mesoscale Simulations and Plastic Flow*. Oxford University Press, 2013.

[68] *The Determination of the Elastic Field of an Ellipsoidal Inclusion, and Related Problems*, vol. 241, 1957.

[69] W. Cai, A. Arsenlis, C. R. Weinberg, and V. V. Bulatov, "A non-singular continuum theory of dislocations," *Journal of The Mechanics and Physics of Solids*, vol. 54, pp. 561–587, 2006.

[70] R. Gatti, A. Marzegalli, V. Zinovyev, F. Montalenti, and L. Miglio, "Modeling the plastic relaxation onset in realistic SiGe islands on Si(001)," *Phys. Rev. B*, vol. 78, no. 18, pp. 184104–184115, 2008.

[71] M. Salvalaglio and F. Montalenti, "Fine control of plastic and elastic relaxation in Ge/Si vertical heterostructures," *Journal of Applied Physics*, vol. 116, pp. 104306–104314, 2014.

[72] B. J. Spencer, P. W. Voorhees, and S. H. Davis, "Morphological instability in epitaxially strained dislocation-free solid films," *Phys. Rev. Lett.*, vol. 67, no. 26, pp. 3696–3699, 1991.

[73] D. J. Godbey, J. V. Lill, J. Deppe, and K. D. Hobart, "Ge surface segregation at low temperature during SiGe growth by molecular beam epitaxy," *Appl. Phys. Lett.*, vol. 65, no. 6, p. 711, 1994.

[74] A. Rastelli, *Structural Evolution of Nanoscopic Islands of Ge and SiGe on Si(001)*. PhD thesis, Università degli studi di Pavia, 2002.

[75] Y. Xiang and W. E, "Nonlinear evolution equation for the stress-driven morphological instability," *Journal of Applied Physics*, vol. 91, no. 11, p. 9414, 2002.

[76] I. Berbezier, J.-N. Aqua, M. Aouassa, L. Favre, S. Escoubas, A. Gouyé, and A. Ronda, "Accommodation of sige strain on a universally compliant porous silicon substrate," *Phys. Rev. B*, vol. 90, p. 035315, Jul 2014.

[77] D. E. Jesson, S. J. Pennycook, J.-M. Baribeau, and D. C. Houghton, "Direct imaging of surface cusp evolution during strained-layer epitaxy and implications for strain relaxation," *Phys. Rev. Lett.*, vol. 71, pp. 1744–1747, Sep 1993.

[78] H. Hu, H. J. Gao, and F. Liu, "Theory of directed nucleation of strained islands on patterned substrates," *Phys. Rev. Lett.*, vol. 101, p. 216102, Nov 2008.

[79] J.-N. Aqua and X. Xu, "Directed self-organization of quantum dots," *Physical Review E*, vol. 90, no. 3, pp. 030402–030406(R), 2014.

[80] Y.-W. Zhang, "Formation of epitaxially strained islands by controlled annealing," *Applied Physics Letters*, vol. 75, no. 2, pp. 205–207, 1999.

[81] H. R. Eisenberg and D. Kandel, "Formation, ripening, and stability of epitaxially strained island arrays," *Physical Review B*, vol. 71, pp. 115423–115421, 2005.

[82] M. Levine, A. Golovin, S. Davis, and P. W. Voorhees, "Self-assembly of quantum dots in a thin epitaxial film wetting an elastic substrate," *Physical Review B*, vol. 75, pp. 205312–205322, 2007.

[83] M. Albani, R. Bergamaschini, and F. Montalenti, "Dynamics of pit filling in heteroepitaxy via phase-field simulations," *Phys. Rev. B*, vol. 94, p. 075303, 2016.

[84] F. Boccardo, "Dewetting-induced pinching of strained solid films at the nanoscale." Master Thesis. Università degli studi di Milano-Bicocca, 2018.

[85] G. Reiter, "Dewetting of thin polymer films," *Phys. Rev. Lett.*, vol. 68, pp. 75–78, Jan 1992.

[86] C. V. Thompson, "Solid-state dewetting of thin films," *Annual Review of Materials Research*, vol. 42, no. 1, pp. 399–434, 2012.

[87] H. Wong, P. Voorhees, M. Miksis, and S. Davis, "Periodic mass shedding of a retracting solid film step," *Acta Materialia*, vol. 48, no. 8, pp. 1719–1728, 2000.

[88] F. K. LeGoues, M. C. Reuter, J. Tersoff, M. Hammar, and R. M. Tromp, "Cyclic Growth of Strain-Relaxed Islands," *Phys. Rev. Lett.*, vol. 73, no. 2, p. 300, 1994.

[89] F. Boioli, V. A. Zinovyev, R. Gatti, A. Marzegalli, F. Montalenti, M. Stoffel, T. Merdzhanova, L. Wang, F. Pezzoli, A. Rastelli, O. G. Schmidt, and L. Miglio, "Self-Ordering of Misfit Dislocation Segments in Epitaxial SiGe Islands on Si(001)," *Journal of Applied Physics*, vol. 110, no. 4, p. 044310, 2011.

[90] A. Marzegalli, V. A. Zinovyev, F. Montalenti, A. Rastelli, M. Stoffel, T. Merdzhanova, O. G. Schmidt, and L. Miglio, "Critical shape and size for dislocation nucleation in $Si_{1-x}Ge_x$ islands on Si(001)," *Physical Review Letters*, vol. 99, pp. 235505–235509, Dec 2007.

[91] R. Hull, "Equilibrium theory of misfit dislocations networks," in *Properties of Silicon Germanium and SiGe: Carbon* (E. Kasper and K. Lyutovich, eds.), Exeter (UK): Inspec, 2000.

[92] L. Colace, G. Masini, F. Galluzzi, G. Assanto, G. Capellini, L. D. Gaspare, E. Palange, and F. Evangelisti, "Metal-semiconductor-metal near-infrared light detector based on epitaxial Ge/Si," *Appl. Phys. Lett.*, vol. 72, pp. 3175–3177, 1998.

[93] A. Marzegalli, M. Brunetto, M. Salvalaglio, F. Montalenti, G. Nicotra, M. Scuderi, C. Spinella, M. De Seta, and G. Capellini, "Onset of plastic relaxation in the growth of ge on si(001) at low temperatures: Atomic-scale microscopy and dislocation modeling," *Physical Review B*, vol. 88, p. 165418, Oct 2013.

[94] Y. B. Bolkhovityanov, A. S. Deryabin, A. K. Gutakovskii, and L. V. Sokolov, "Mechanism of induced nucleation of misfit dislocations in the Ge-on-Si(001) system and its role in the formation of the core structure of edge misfit dislocations," *Acta Mater.*, vol. 61, no. 2, p. 617, 2013.

[95] E. A. Fitzgerald, Y. H. Xie, D. Monroe, P. J. Silverman, J. M. Kuo, A. R. Kortan, and F. A. Thiel, "Relaxed Ge_xSi_{1-x} structures for III–V integration with Si and high mobility two-dimensional elctron gases in Si," *Journal of Vacuum Science and Technology B*, vol. 10, no. 4, pp. 1807–1819, 1992.

[96] A. M. Andrews, R. LeSar, M. A. Kerner, J. S. Speck, A. E. Romanov, A. L. Kolesnikova, M. Bobeth, and W. Pompe, "Modeling crosshatch surface morphology in growing mismatched layers. Part II: Periodic boundary conditions and dislocation groups," *J. Appl. Phys.*, vol. 95, no. 11, p. 6032, 2004.

[97] K. H. Chang, R. Gilbala, D. J. Srolovitz, P. K. Bhattacharya, and J. F. Mansfield, "Crosshatched surface morphology in strained III-V semiconductor films," *Journal of Applied Physics*, vol. 67, no. 9, pp. 4093–4098, 1990.

[98] S. Kishino, M. Ogirima, and K. Kurata, "A Cross-Hatch Pattern in $GaAs_{1-x}P_x$ Epitaxially Grown on GaAs Substrate," *J. Electrochem. Soc.*, vol. 119, no. 5, pp. 617–622, 1972.

[99] T. Nishioka, Y. Itoh, A. Yamamoto, and M. Yamaguchi, "Crosshatch patterns in GaAs films on Si substrates due to thermal strain in annealing processes," *Applied Physics Letters*, vol. 51, no. 23, pp. 1928–1930, 1987.

[100] V. Kaganer, R. Köhler, M. Schmidbauer, R. Opitz, and B. Jenichen, "X-ray diffraction peaks due to misfit dislocations in heteroepitaxial structures," *Physical Review B*, vol. 55, pp. 1793–1810, 1997.

[101] M. H. Zoellner, M.-I. Richard, G. A. Chahine, P. Zaumseil, C. Reich, G. Capellini, F. Montalenti, A. Marzegalli, Y. H. Xie, T. U. Schülli, M. Häberlen, P. Storck, and T. Schroeder, "Imaging structure and composition homogeneity of 300 mm SiGe virtual substrates for advanced CMOS applications by scanning X-ray diffraction microscopy," *ACS Applied Materials and Interfaces*, vol. 7, no. 17, pp. 9031–9037, 2015.

[102] A. J. Wilkinson, "Assessment of lattice strain, rotation and dislocation content using electron back-scatter diffraction," *Journal of Physics: Conference Series*, vol. 326, p. 012004, 2011.

[103] P. M. Mooney, F. K. Legoues, J. O. Chu, and S. F. Nelson, "Strain relaxation and mosaic structure in relaxed SiGe layers," *Applied Physics Letters*, vol. 62, no. 26, pp. 3464–3466, 1993.

[104] V. M. Kaganer, T. Ulyanenkova, A. Benediktovitch, M. Myronov, and A. Ulyanenkov, "Bunches of misfit dislocations on the onset of relaxation of Si 0.4 Ge 0.6 /Si(001) epitaxial films revealed by high-

resolution x-ray diffraction," *Journal of Applied Physics*, vol. 122, no. 10, p. 105302, 2017.

[105] S. Mochizuki, A. Sakai, N. Taoka, O. Nakatsuka, S. Takeda, S. Kimura, M. Ogawa, and S. Zaima, "Local strain in SiGe/Si heterostructures analyzed by X-ray microdiffraction," *Thin Solid Films*, vol. 508, no. 1-2, pp. 128–131, 2006.

[106] F. Rovaris, M. H. Zoellner, P. Zaumseil, M. A. Schubert, A. Marzegalli, L. D. Gaspare, M. D. Seta, T. Schroeder, P. Storck, G. Schwalb, T. U. Schülli, G. Capellini, and F. Montalenti, "Misfit-Dislocation Distributions in Heteroepitaxy : From Mesoscale Measurements to Individual Defects and Back," *Physical Review Applied*, vol. 10, no. 5, p. 054067, 2018.

[107] A. M. Andrews, J. S. Speck, A. E. Romanov, M. Bobeth, and W. Pompe, "Modeling cross-hatch surface morphology in growing mismatched layers," *Journal of Applied Physics*, vol. 91, p. 1933, feb 2002.

[108] M. Albrecht, S. Christiansen, J. Michler, W. Dorsch, H. P. Strunk, P. O. Hansson, and E. Bauser, "Surface ripples, crosshatch pattern, and dislocation formation: Cooperating mechanisms in lattice mismatch relaxation," *Applied Physics Letters*, vol. 67, no. 9, pp. 1232–1234, 1995.

[109] F. Jonsdottir and L. Freund, "Equilibrium surface roughness of a strained epitaxial film due to surface diffusion induced by interface misfit dislocations," *Mechanics of Materials*, vol. 20, pp. 337–349, jun 1995.

[110] R. Bergamaschini, M. Salvalaglio, R. Backofen, A. Voigt, and F. Montalenti, "Continuum modelling of semiconductor heteroepitaxy: an applied perspective," *Advances in Physics: X*, vol. 1, no. 3, pp. 331–367, 2016.

[111] F. Rovaris, M. H. Zoellner, P. Zaumseil, A. Marzegalli, L. Di Gaspare, M. De Seta, T. Schroeder, P. Storck, G. Schwalb, G. Capellini, and F. Montalenti, "Dynamics of crosshatch patterns in heteroepitaxy," *Phys. Rev. B*, vol. 100, p. 085307, Aug 2019.

[112] A. Marzegalli, F. Isa, H. Groiss, E. Müller, C. V. Falub, A. Taboada, P. Niedermann, G. Isella, F. Schöffler, F. Montalenti, H. von Känel, and L. Miglio, "Unexpected Dominance of Vertical Dislocations in High-Misfit Ge/Si(001) Films and Their Elimination by Deep Substrate Patterning," *Adv. Mater.*, vol. 25, pp. 4408–4412, 2013.

[113] F. Isa, A. Marzegalli, A. Taboada, C. V. Falub, G. Isella, F. Montalenti, H. von Kaenel, and L. Miglio, "Onset of vertical threading dislocations in $Si_{1-x}Ge_x$/Si (001) at a critical Ge concentration," *APL Mater*, vol. 1, p. 52109, 2013.

[114] F. Isa, M. Salvalaglio, Y. Dasilva, M. Medura, M. Barget, A. Jung, T. Kreiliger, G. Isella, R. Erni, F. Pezzoli, E. Bonera, P. Niedermann, P. Groening, F. Montalenti, and H. von Kaenel, "Highly

Mismatched, Dislocation-Free SiGe/Si Heterostructures," *Adv. Mater.*, vol. 28, pp. 884–888, 2016.

[115] F. Isa, M. Salvalaglio, Y. A. R. Dasilva, A. Jung, G. Isella, R. Erni, B. Timotijevic, P. Niedermann, P. Groening, F. Montalenti, and H. von Kaenel, "Enhancing elastic stress relaxation in SiGe/Si heterostructures by Si pillar necking," *Appl. Phys. Lett.*, vol. 109, p. 182112, 2016.

[116] C. Rosenblad, H. R. Deller, A. Dommann, T. Meyer, P. Schroeter, and H. von Kaenel, "Silicon epitaxy by low-energy plasma enhanced chemical vapor deposition," *Journal of Vacuum Science & Technology A: Vacuum, Surfaces, and Films*, vol. 16, no. 5, pp. 2785–2790, 1998.

[117] R. Bergamaschini, F. Isa, C. Falub, P. Niedermann, E. Müller, G. Isella, H. von Känel, and L. Miglio, "Self-aligned ge and sige three-dimensional epitaxy on dense si pillar arrays," *Surface Science Reports*, vol. 68, no. 3, pp. 390 – 417, 2013.

[118] F. Isa, M. Salvalaglio, Y. A. R. Dasilva, A. Jung, G. Isella, R. Erni, P. Niedermann, P. Gröning, F. Montalenti, and H. von Känel, "From plastic to elastic stress relaxation in highly mismatched sige/si heterostructures," *Acta Materialia*, vol. 114, pp. 97 – 105, 2016.

[119] K. W. Schwarz, "Simulation of dislocations on the mesoscopic scale. II. Methods and examples," *Journal of Applied Physics*, vol. 85, no. 1, pp. 120–129, 1999.

[120] F. Rovaris, R. Bergamaschini, and F. Montalenti, "Modeling the competition between elastic and plastic relaxation in semiconductor heteroepitaxy: From cyclic growth to flat films," *Phys. Rev. B*, vol. 94, 2016.

[121] F. Rovaris, F. Isa, R. Gatti, A. Jung, G. Isella, F. Montalenti, and H. von Känel, "Three-dimensional Sige/Si heterostructures: Switching the dislocation sign by substrate under-etching," *Phys. Rev. Materials*, vol. 1, p. 073602, 2017.

[122] F. Montalenti, F. Rovaris, R. Bergamaschini, L. Miglio, M. Salvalaglio, G. Isella, F. Isa, and H. Von Känel, "Dislocation-free SiGe/Si heterostructures," *Crystals*, vol. 8, no. 6, 2018.